Thermal Stability of Alumina-based

Hard Coatings

by

Dipl.-Ing. Viktoria Edlmayr

being a thesis in partial fulfillment of the requirements for the degree of a

Doctor of Montanistic Sciences (Dr. mont.)

at the Montanuniversität Leoben.

Munich, Germany, October 2014

Preface

The work presented in this thesis concerns the growth, characterization and thermal stability of alumina-based hard coatings and was done at the Department Physical Metallurgy and Materials Testing of the Montanuniversität Leoben in Austria within the Research Studio Austria energy-drive, with financial support from the Österreichische Forschungsförderungsgesellschaft and the Bundesministerium für Wirtschaft, Familie und Jugend.

Affidavit

I declare in lieu of oath, that I wrote this thesis and performed the associated research myself, using only literature cited in this volume.

Munich, Germany, October 2014

Acknowledgements

I am grateful to a number of people who have supported me in many different ways and contributed to the work present in this thesis.

I would especially like to thank...

...my supervisor **Prof. Dr. Christian Mitterer**, leader of the Thin Film Group in Leoben, for giving me the opportunity to perform this work in his group, for his steady strategic guidance, support and trust during the projects, and for providing the freedom for action necessary for successful scientific working. Finally, he enabled to finish this thesis after a long break - which I appreciate as a huge gift.
It was the best choice to join your group!

...**Prof. Dr. Helmut Clemens**, head of Department Physical Metallurgy and Materials testing, for his great support and the opportunity to carry out this thesis on his department and the **staff of the department** for their administrative cooperation as well as being a helping hand on the various challenges that occurred during this thesis.

...my **past and present colleagues and friends** within the **Thin Film Group** for vital discussions, support and especially their friendship. Thank you to all who had the patience to show me how to use equipment or have endured my questioning.
I enjoy remembering the combination of scientific atmosphere and the fun we had during our work and non-work related discussions at the coffee table, lunch breaks, enjoyable traveling to conferences together, and after-work activities such as intercultural cooking and sports.
Dear friends, thank you for the wonderful time! Without you, work would not have been as much fun as it was!

Table of content

1. Introduction

The oldest known technical application of surface engineering by mankind is devoted to gold layers, which came into favor from about the 3rd millennium B.C. in the Middle East [Oddy1981]. They provided the appearance of solid gold allowing a greater use of the limited gold available. However, the first thin film applications can be traced back all the way to the ancient Egypt, where hammering and other refining techniques were developed to reduce the thickness of the so-called gold leaf to a thin gold film having a film thickness of 0.3 µm. These thin films of gold were applied to decorative objects and fashion items for optical reasons in Egypt in about 1500 B.C. [Nicholson1979, Hunt1973]. Already in 1200 B.C., the Egyptians mastered the art of beating gold to extend its use from only decorative purposes to more functional purposes via alloying gold with other metals. Subsequently, more variations for colors for decorative coatings could be achieved and mechanical properties of the coatings such as hardness could be improved [Gold2014].

In the present time, the two main reasons motivating the use of coatings remain unchanged and the global market demands decorative coatings as well as functional tailor made materials perfectly fulfilling all special requirements of their respective fields of application. For example, in the domain of cutting applications, the tools are subjected to high temperatures, wear, oxidation and surface fatigue. Thus, the requirements on cutting tools for a high durability include high hardness and toughness, chemical inertness against the environment and working material at elevated temperatures. To comply with these requirements, a combination of coating properties with bulk properties of another material is needed. More specifically, a thin coating is deposited onto another material (bulk or substrate) in order to achieve properties that cannot be attained by the coating or the bulk alone. Therefore, cutting

tools are made of high speed steel or cemented carbide (bulk), which are coated with protective and wear-resistant coatings. Since aluminum oxide, or alumina for short, has excellent properties like chemical inertness, corrosion resistance and high hardness, alumina is a state-of-the-art protective coating material for cemented carbide cutting tools. Thus, Al_2O_3 coatings improve the productivity of machining operations by increasing life time and cutting speed due to their excellent wear protection, high hot hardness and stability at elevated temperatures [Kathrein2003].

Crystalline Al_2O_3 and $(Al_xCr_{1-x})_2O_3$ coatings are well-researched, but due to the complexities arising from the existence of various different crystalline alumina phases, many questions still remain to be answered concerning the relationships between synthesis, composition, microstructure and the thermal stability of these alumina-based coatings. The primary objective of this work is to deposit crystalline alumina coatings by reactive magnetron sputtering in industrial scale deposition systems and contribute to the understanding of the mechanisms behind the formation of different phases in these coatings. Furthermore, their thermal stability, microstructural changes during thermal load and transformation sequences from the metastable to the desired thermodynamically stable $\alpha-Al_2O_3$ phase having the above mentioned properties required for a protective coating for cutting tools have to be investigated. The secondary objective is to find an alumina-based coating material exhibiting similar properties in terms of thermal stability, wear resistance and hardness compared to the $\alpha-Al_2O_3$ phase, which is suitable as protecting coating material, but can be deposited at reduced temperatures. Low deposition temperatures provide the opportunity to use a wider range of substrate materials. More specifically, this has been done by exploring metastable $(Al_xCr_{1-x})_2O_3$ solid solution coatings grown by reactive cathodic arc evaporation. Finally, the effects of thermal annealing on the microstructure of these $(Al_xCr_{1-x})_2O_3$ solid solution coatings have been studied in detail.

The following chapters of this thesis give a comprehensive overview on the theoretical background of the most important aspects of this work concerning the

used deposition techniques, the growth of thin films in general and the investigated alumina-based coating materials. Subsequently, an introduction to the employed characterization techniques is given, followed by a short summary of the most important findings. The major experimental research is summarized in three subsequent scientific publications presented at the end of this work.

2. Coating synthesis by physical vapor deposition

In general, physical vapor deposition (PVD) processes are techniques to deposit thin films by evaporation or sputtering under vacuum conditions. Nowadays, numerous PVD modifications have been developed and are in industrial use [Bunshah1982, Häfer1987, Kienel1995, Moll1992, Rother1992]. The main steps to deposit a coating are evaporation of a solid phase (the so-called target), the transport of the vapor to a substrate followed by condensation on the substrate. To ensure that the vaporized coating material is transported directly to the substrate and to avoid collisions and other involuntary reactions, PVD techniques operate under vacuum conditions. However, for deposition of compounds an additional gas can be added into the chamber so that a reaction between the target components and the reactive gas can take place. These processes are called reactive processes [Bunshah1982, Bunshah2001, Hocking1989].

Hence, a major advantage of PVD can be found in the huge variety of selectable coating materials ranging from pure metals (e.g. Cr) and alloys (e.g. AlCr) to compounds like oxides (e.g. Al_2O_3, $(Al,Cr)_2O_3$), nitrides and carbides [Mitterer2014]. Another advantage as compared to other deposition techniques, e.g. chemical vapor deposition (CVD), is the opportunity to deposit at very low deposition temperatures if needed, so that even polymers can be used as substrate material. However, consequently PVD results in synthesis of coatings usually far from their thermodynamic equilibrium [Bunshah1982, Häfer1987, Moll1992].

The PVD techniques used in this work are unbalanced magnetron sputtering (Publication I, Publication II) and arc evaporation (Publication III), both in reactive mode. The following chapter summarizes the most important aspects of these two

techniques (see also Chapters 9 to 11: Publications I, II and III); further information is given in scientific articles [Bunshah2001, Kienel1995, Konuma1992, Rother1992, Smith1995, Steffens1996].

2.1 Reactive magnetron sputtering

Sputtering is based on the ejection of deposition material from a solid target via bombardment by energetic particles of an inert gas. Figure 1 shows schematically the arrangement of a direct current unbalanced magnetron sputtering system modified after [Mitterer2014, Sproul1991], which consists mainly of two facing electrodes, a target (cathode) and an assembly of substrates on a substrate holder (anode), both arranged in an evacuated deposition chamber. The target is connected to the negative potential of a direct current (DC) supply to sustain a glow discharge [Kienel1995, Rother1992]. Substrates are placed at some distance to the target, so they intercept the flux of the ejected atoms [Mattox2010]. They may be grounded or also be negatively or positively charged via a bias voltage. During deposition, ions of an inert gas (the so-called working gas) are accelerated to the negatively charged target, ejecting deposition material. These evaporated atoms leave the target having a certain energy level and undergo gas scattering while traversing the plasma. Due to collision and scattering, the kinetic energy of the atoms is reduced and some atoms absorb on the chamber walls. Hence, low deposition rates are observed. In order to overcome that drawback, the cathode can be equipped with permanent magnets located behind the target. These magnets apply magnetic fields parallel to the target and perpendicular to the electric field. Hence, electrons are localized near the target via the occurring Lorentz force and the ionization of the working gas is increased. This arrangement is known as DC magnetron sputtering. Dependent on whether all field lines between the magnetic poles are closed or the field lines are partially open towards the substrate, the magnetrons are designed as conventional balanced or

unbalanced magnetrons. Typically, high voltages (several hundreds to a few thousands Volts) in combination with low currents (in the range of milli- to several ten Amperes) are applied. The usage of unbalanced magnetrons allows the plasma to interact with the growing coating, thereby affecting the ad-atom mobility as well as the nucleation and growth kinetics [Chapman1980, Ohring2002, Petrov1992].
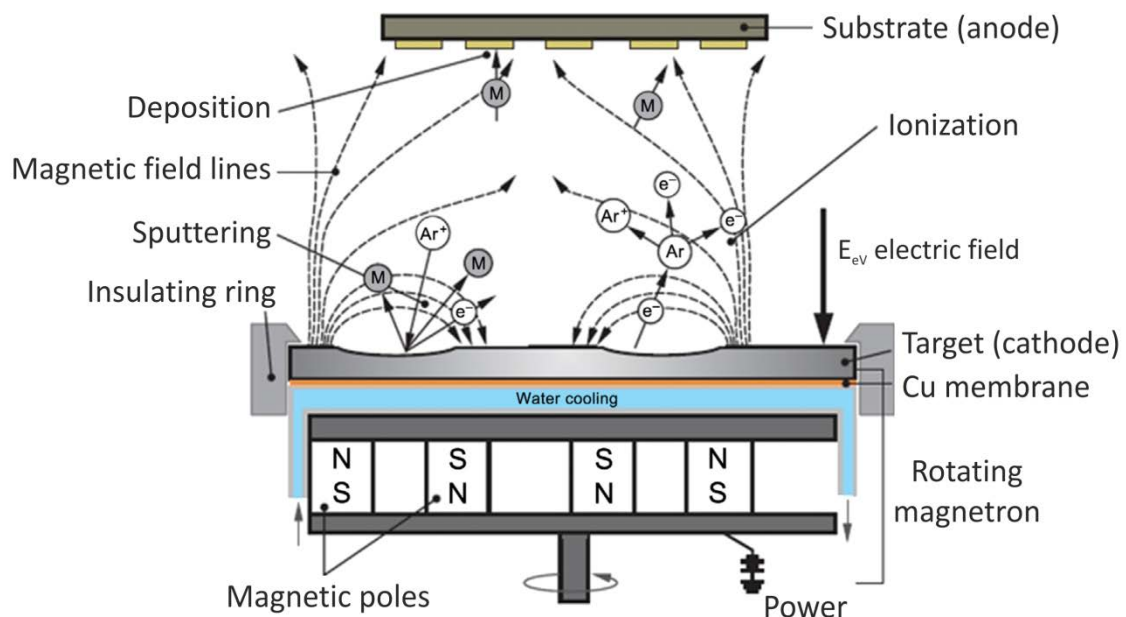
Figure 1: Schematic of a DC unbalanced magnetron sputtering system [Mitterer2014]; Ar...argon atom, Ar$^+$...argon ion, e$^-$...electron, M...metal atom.

In general, sputtering allows various target materials, conductive, semi-conductive as well as insulating materials. However, when a DC voltage is applied at the target only electrical conductors can be used as target material. Other arrangements of the sputter process, like the so-called pulsed DC sputtering or radio frequency sputtering, enable sputtering of conductive, semi-conductive and insulating materials. Applying a pulsed DC voltage to multi-magnetron systems enables a process where alternatively one target acts as cathode and the other one acts as anode. This mode is called bipolar pulsed and leads to a reduced thermal exposure, due to the downtime of the respective target acting currently as anode [Schulze2000].

The transfer of the target species to the vapor state and to the heated and/or biased substrate surface, where adsorption, nucleation and growth can take place, is different for several deposition techniques. In the case of non-reactive magnetron sputtering, the deposition chamber is backfilled with a noble gas such as Ar and the deposited coating contains elements from the target material only. If a component of the deposited coating is additionally introduced into the deposition chamber in form of a non-inert gas (e.g. O_2, N_2, CH_4), the technique is called reactive as described above. The compound of the target atoms and the reactive gas can be formed on the target surface, in the plasma or on the substrate surface, where the latter is the most important one for deposition of the coating [Frey1995, Mattox2010]. Unfortunately, a reactive process also comes along with forming a coating on the target causing an effect called target poisoning, where the sputtering conditions change depending on the coverage of the target with an in the worst case non-conductive coating (e.g. Al_2O_3 for sputtering of Al in O_2). This effect can be controlled by the sputter power and the partial pressure of the reactive gas [Mitterer2014, Sproul2005].

The alumina coatings studied in this thesis were grown in an industrial scale CemeCon CC800/9MLT system equipped with four bipolar pulsed unbalanced DC magnetrons by reactive magnetron sputtering. The respective deposition parameters for the Al_2O_3 coatings studied are given in Publications I and II.

2.2 Cathodic arc evaporation

Cathodic arc evaporation has a lot similarities with the above described sputter process. The deposition chamber is evacuated and, if necessary, inert and/or reactive gases are simultaneously used for deposition. The source of deposition material is again a target (cathode) and the substrates can be heated and/or biased. In contrast to sputtering, cathodic arc evaporation uses a high current (30 A to several kiloamperes)

in combination with low voltage (20 to 100 V) for an electrical gas discharge between two electrodes. Arc erosion is generated by a short circuit of two metal electrodes which are separated immediately and a small luminous spot is formed at the cathodic target, which then passes the high current density region and ignites an arc. The point of contact between the arc and the target is called arc spot, which is very small (10^{-8} to 10^{-4} m in diameter) and moves randomly along the target surface. Thereby, it creates a high flux of ionized target material and electrons, which enables a self-sustained plasma with extremely high ionization rates (> 95 %) of the coating forming species [Anders2008]. The arc spot is an intense source of plasma with a current density of in the order of 10^{12} A/m [Anders2008, Mitterer2014]. To achieve a uniform evaporation of the target, the arc is steered magnetically (so-called steered arc [Ohring1991]).

Cathodic arc evaporation enables synthesis of coatings exhibiting a high density, thus efficient growth of compound coatings is possible. However, there is a major drawback, i.e. the emission of macro droplets from the arc spot. These droplets leave the target in a molten state and have a typical size between 0.01 to 10 µm (see for an example in Figure 2). Upon impact on a substrate, the droplets flatten and solidify. Hence, they are incorporated as defects in the growing coating and some properties of the coating are negatively affected. Holes or porous areas in the vicinity of these growth defects can act as diffusion paths, which may deteriorate the corrosion and oxidation resistance of the coating [Hörling2002, Petrov1997]. Droplets extending the whole coating thickness or being located on the surface of the coating cause additional surface roughness, which necessitates further surface treatments.
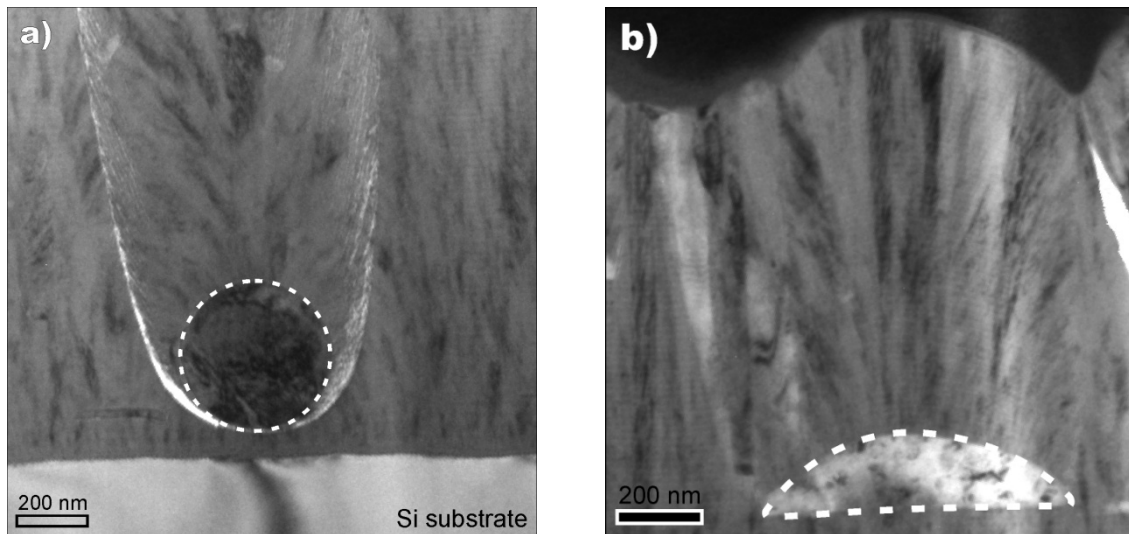
Figure 2: Bright-field TEM images of (a) ball-shaped droplet and (b) hemispherical-shaped droplet in an $(Al_xCr_{1-x})_2O_3$ coating deposited on Si substrate [own work, for more details see Publication III].

However, the emission and size of such droplets can be influenced in various ways, for example via filtering by magnetic fields as well as the coating material itself [Anders2008].

In this work, an Oerlikon Balzers INNOVA industrial arc evaporation system was used for Publication III, equipped with four Al/Cr compound targets. Depositions were performed in argon/oxygen atmosphere and the substrates were mounted on a two-fold planetary rotating substrate carousel. Further deposition parameters are given in Publication III.

3. Thin film growth

In general, thin film growth is a result of the condensation of mobile ad-atoms on the substrate surface. Since the microstructure of coatings is formed by atomic-scale processes occurring during deposition, in particular by nucleation and growth, the coating properties mainly depend on deposition parameters [Choy2000]. But also factors like substrate surface condition, deposition system geometry, film growth details including surface mobility of the ad-atoms, and post-deposition processing and reactions such as those with the ambient have to be well controlled in order to get a coating having desired structure and properties [Mattox2010].

3.1 Nucleation and growth

Growth processes of typical hard coatings, which control the evolution of microstructure, include nucleation, island growth, coalescence of islands, formation of polycrystalline islands, development of a continuous structure and film growth [Barna1998, Petrov2003]. In particular, impinging species like atoms or ions arrive at a surface and can either be adsorbed or directly reflected, depending on the appearance of the substrate surface, as schematically illustrated in Figure 3. Since an adequate affinity of the chemical nature of substrate and film is necessary for condensation, the species can not immediately condense at the substrate surface and deposit a film; initially only surface adsorption can take place. However, most particles remain on the surface for a certain time and form metastable or stable clusters, which can grow by binding or diffusion or by direct capture of atoms from the vapor phase. Larger clusters may also grow at the expense of neighboring smaller clusters by so-called Oswald

ripening. Subsequently, a network of connected clusters is formed through continued coalescence, the remaining holes can be filled and finally a continuous film is obtained. This cluster formation can be defined as nucleation and the combination of clusters is termed growth [Greene1993, Greene2009].
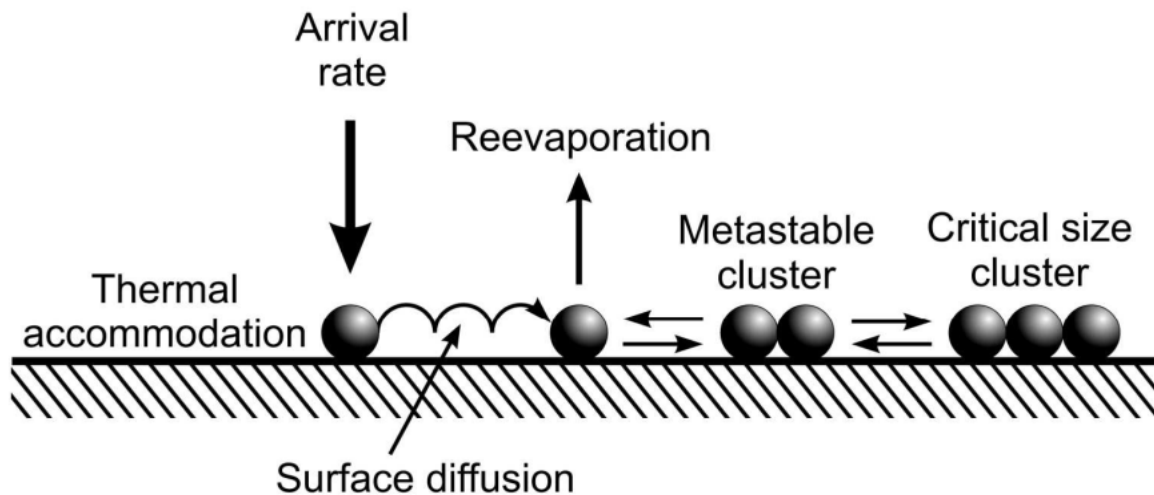
Figure 3: Schematic illustration of the nucleation process and film growth on a substrate modified after Greene [Greene1993].

According to Greene and Jehn *et al.* [Greene1993, Jehn1992], thin film growth can be divided into three different types, which are represented in Figure 4. Island or Volmer-Weber growth, which is characterized by three-dimensional (3D) nucleation and growth (see Figure 4a); layer-by-layer or Frank-Van der Merwe-growth leading to a monolayer-by-monolayer growth (see Figure 4b); and layer plus island or Stranski-Krastanov growth, where 3D islands grow on a layer on the substrate (see Figure 4c).
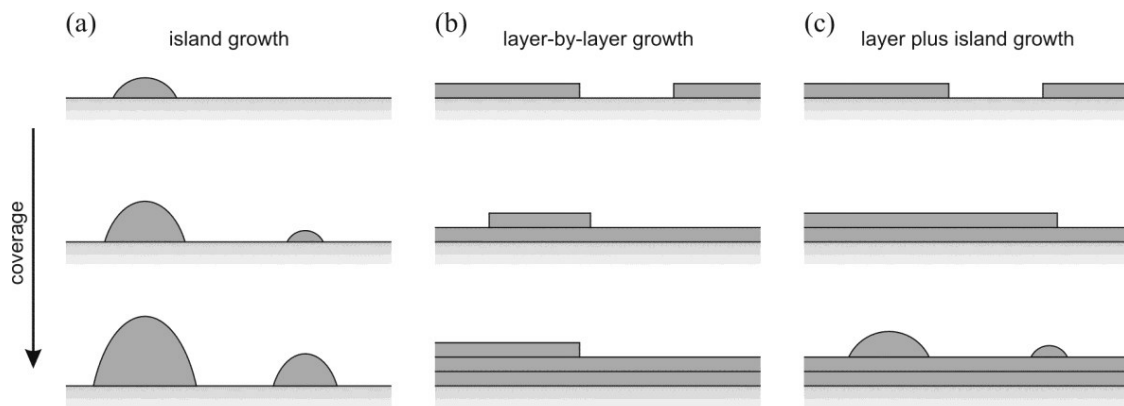
Figure 4: Basic modes of film growth, (a) Island growth (Volmer-Weber), (b) Layer-by-layer growth (Frank-Van der Merwe), (c) Layer plus island growth (Stranski-Krastanov) [Greene1994].

Which growth mechanism preferentially occurs during deposition depends mainly on the film-species and substrate affinity, the activation energy of diffusion and the binding energies between the film atoms and between the film and the substrate [Ensinger1997, Greene1993, Jehn1992, Mayrhofer2001].

3.2 Structure zone models

As discussed earlier, growth of the coating depends on both the nucleation and growth kinetics, where selected processes take place and determine the structure of the coating. Therefore, so-called structure zone models (SZMs) have been developed in order to correlate the microstructure of coatings with deposition parameters. These SZMs show the morphology and structural aspects of coatings in dependence on ad-atom mobility.

Movchan and Demchishin introduced the first SZM for evaporated coatings in 1969, which distinguishes between three structural zones classified by homologous temperatures, i.e. the ratio between substrate temperature and melting point of the deposited species. Since the ad-atom mobility is related to the melting point of the deposited species, a correlation between the homologous temperature and the observed structure is valid. While zone 1 shows a porous columnar structure due to insufficient surface mobility, zone 2 is dominated by surface diffusion processes resulting in a columnar dense coating, where shadowing effects can be overcome. In zone 3, bulk diffusion is enabled resulting in a recrystallized structure [Movchan1969]. In order to extend the model of Movchan and Demchishin on sputtered coatings, Thornton developed a similar model, where an inert gas pressure, i.e. argon, was taken into account by adding a second axis to the model. With increasing argon pressure, the above described structural zones are shifted to higher temperatures due to inert gas scattering. Thornton observed an additional zone, called the transition zone T located between zone 1 and zone 2, which is formed at higher temperatures and is characterized by a dense fibrous structure [Thornton1974, Thornton1977]. The model of Thornton was modified by Messier *et al.*, where the gas pressure was substituted by the substrate bias voltage and on account of this, the effect of ion bombardment was included. With increasing ion bombardment (bias voltage), the zone T having a dense-packed fibrous structure gets broader, primarily at the expense of zone 1 [Messier1984]. Furthermore, Barna and Adamik investigated the influence of impurities on the structure evolution and zone formation and suggested a SZM for real polycrystalline coatings. It was disclosed that for high concentrations of impurities, crystal growth is blocked due to periodical development of coverage of the whole crystal surface. Consequently, no grain growth can take place and randomly oriented crystallites are observed [Barna1998]. A detailed description and comparison of the above mentioned SZMs can be found in literature [Barna1998, Bunshah1982, Gissler1992, Messier1984, Movchan1969, Thornton1974].

In the following, a SZM recently published by Anders [Anders2010] will be presented (see Figure 5). Since the diffusion process and structure formation phenomena are not only controlled by the substrate temperature, but by the total energy flux to the growing surface, the use of homologous temperature values only is avoided in this model. Therefore, the linear axis T^* shows a generalized temperature T^*, which includes the homologous temperature plus a temperature shift caused by the potential energy of arriving particles on the surface. The logarithmic normalized energy E^* axis describes displacement and heating effects caused by the kinetic energy of impinging particles and replaces the linear argon pressure axis of already existing SZMs. The until then unlabeled axis is replaced by the net film thickness t^*, which quantitatively indicates a coating densification, sputtering or even "negative film thickness", which can be obtained by ion etching. The different zones describing the expected microstructure of the deposited coating are in accordance with the respective zones 1, 2, 3 and T of the earlier presented SZMs. Additionally, a non-accessible region is illustrated, see Figure 5, because the growth process is limited on one hand when E^*, the kinetic energy of the bombarding ions, is too low for the species to reach the surface, and on the other hand, when the value of E^* is too high. In this case, T^* describing the thermal activation can not be arbitrarily low [Anders2010].
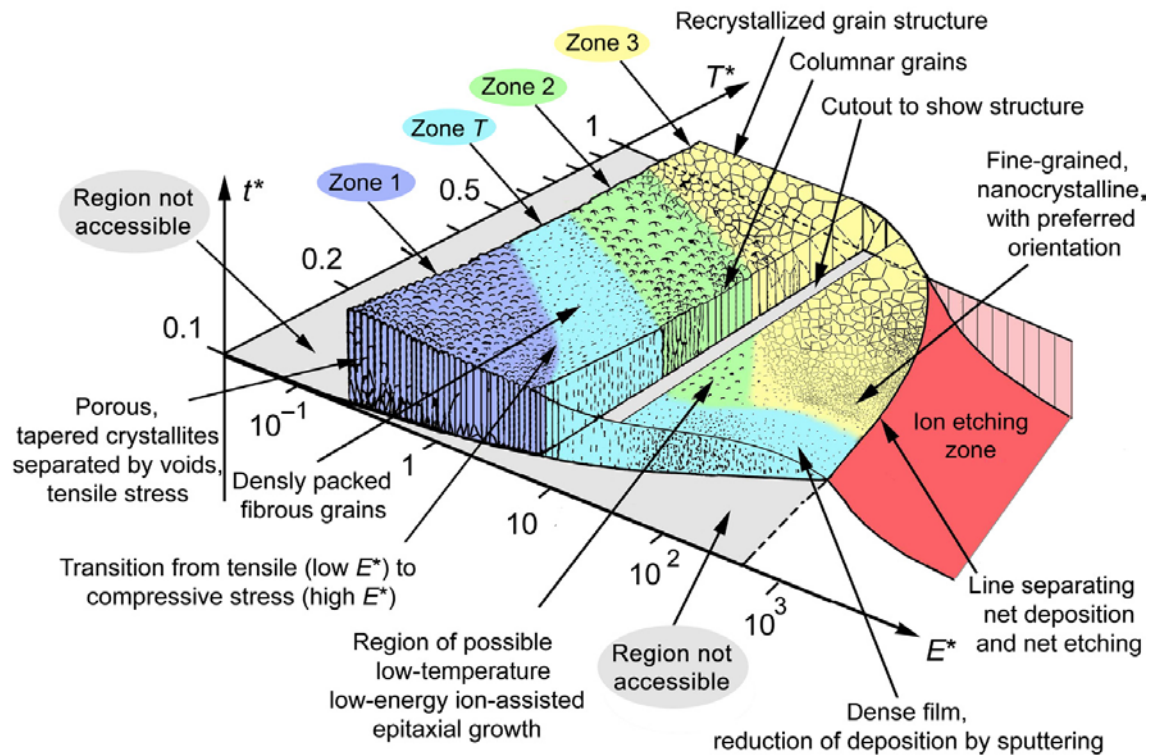
Figure 5: Structure zone model for thin film growth after Anders [Anders 2010]; T^*...generalized temperature, E^*...normalized energy, t^*...net film thickness.

3.3 Ion bombardment

Ion bombardment has a significant impact on the growth conditions of a coating and is therefore a useful tool to increase the density and to modify the morphology of coatings [Mattox1989, Petrov2003]. As shown in the SZM of Thornton, the energy of impinging particles on a surface influences the transition from the above mentioned zone 1 to zone T, which is a region with denser structure and fine fibrous grains stemming from limited surface diffusion [Thornton1977]. For a better understanding, Figures 6a and 6b show schematically the effects of energetic ions

impinging on a surface. While at low ion bombardment conditions, growth is still determined by ad-atom diffusion, an intensified ion bombardment enables incoming ions (P) to knock out atoms from their lattice positions in the substrate due to their high kinetic energy. These knock-out atoms create secondary collisions resulting in cascades of colliding atoms. The atomic motion leads to lattice rearrangements and point defects, i.e. residual interstitials, vacancies and point defects, see Figure 6b [Ensinger1997, Mayrhofer2006].
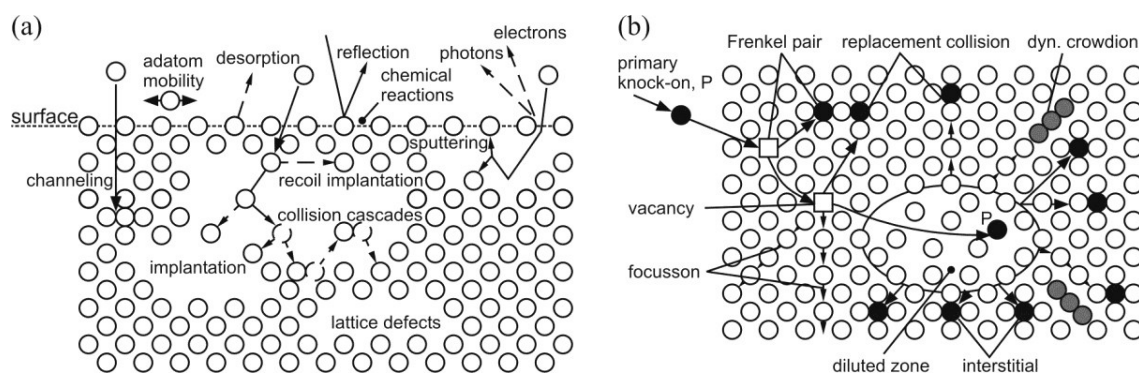
Figure 6: (a) Effects of ion bombardment on a growing film [Ensinger1997, Mattox1989] and (b) Schematic view of possible lattice defects created by an impinging energetic atom, primary knock-on atom (P) [Haasen1978, Mayrhofer2001].

In addition to defect generation, ion bombardment during growth affects the crystallographic orientation as well [Ensinger1997, Greene1993]. In magnetron sputtering, the arriving high energetic particles stem from the sputtering gas itself; i.e. back-scattered or ionized inert or reactive gas atoms, which may be incorporated into the growing film [Mattox1989]. For arc evaporation, the arriving particles contain of a high amount of ionized metal species [Anders2010].

4. Alumina-based coating materials

4.1 Alumina phases

Alumina (Al_2O_3) coatings have been studied intensively in the recent years due to their outstanding properties such as chemical inertness, wear resistance, corrosion resistance, and hardness as well as high thermal stability, which make them interesting as a protective coating material for high temperature applications as well as for cutting tools [Kathrein2003]. Alumina exists in a number of crystalline phases, three of the most important for PVD coatings being α, γ and θ.

The thermodynamically stable phase of alumina at atmospheric pressure is the α−alumina, remaining stable up to the melting point of about 2045 °C [Sitte1985]. This α−alumina phase is also denoted as corundum or sapphire and was first investigated by Bragg and Bragg in 1915 and by Pauling and Hendricks in 1925 [Bragg1916, Pauling1925]. While Bragg *et al.* determined the crystallographic structure of corundum in an approximately way, the first exact attribution to the "corundum structure" was made by Pauling *et al.* This corundum structure can be described as rhombohedral structure (space group R̄3c) with two formula units (10 atoms) in the primitive unit cell [Wyckoff1964]. However, the structure of α−alumina alternatively can be described by an approximately hexagonal close packed (hcp) structure of large oxygen anions stacked in the sequence A–B–A–B, where the aluminum cations are placed on octahedral interstitial positions of this basic array of oxygen ions and form another type of close packed planes, which are inserted between the oxygen layers [Lee1985, Rooksby1961]. In order to maintain charge neutrality, only two thirds of the octahedral interstices available are occupied with aluminum cations, i.e., the

aluminum atoms have six oxygen nearest neighbors [Chiang1996 pp. 10]. Figure 7a shows schematically the location of octahedral sites between two layers of the close packed oxygen super-lattice. Already by aluminum cations taken octahedral sites are marked by small black filled circles. The remaining one third vacant sites are marked with "x" and are located in a way that ensures a maximum separation of the aluminum cations. Depending on the position of the vacant cation site within the layer, three different types of cation layers are defined, each having the same ion configuration but shifted by one atomic spacing, either in the direction of the green vector marked as "1" or "2". They are referred to as layers a, b, and c, which are stacked in the sequence a–b–c–a–b–c. Subsequently, the complete stacking sequence of the anion and cation layers can be written as A–a–B–b–A–c–B–a–A–b–B–c–A and so on. This is schematically illustrated in Figure 7b, which is a vertical slice of Figure 7a along the dashed line. Consequently, after six oxygen layers the unit cell is defined [Chiang1996, Dörre1984].
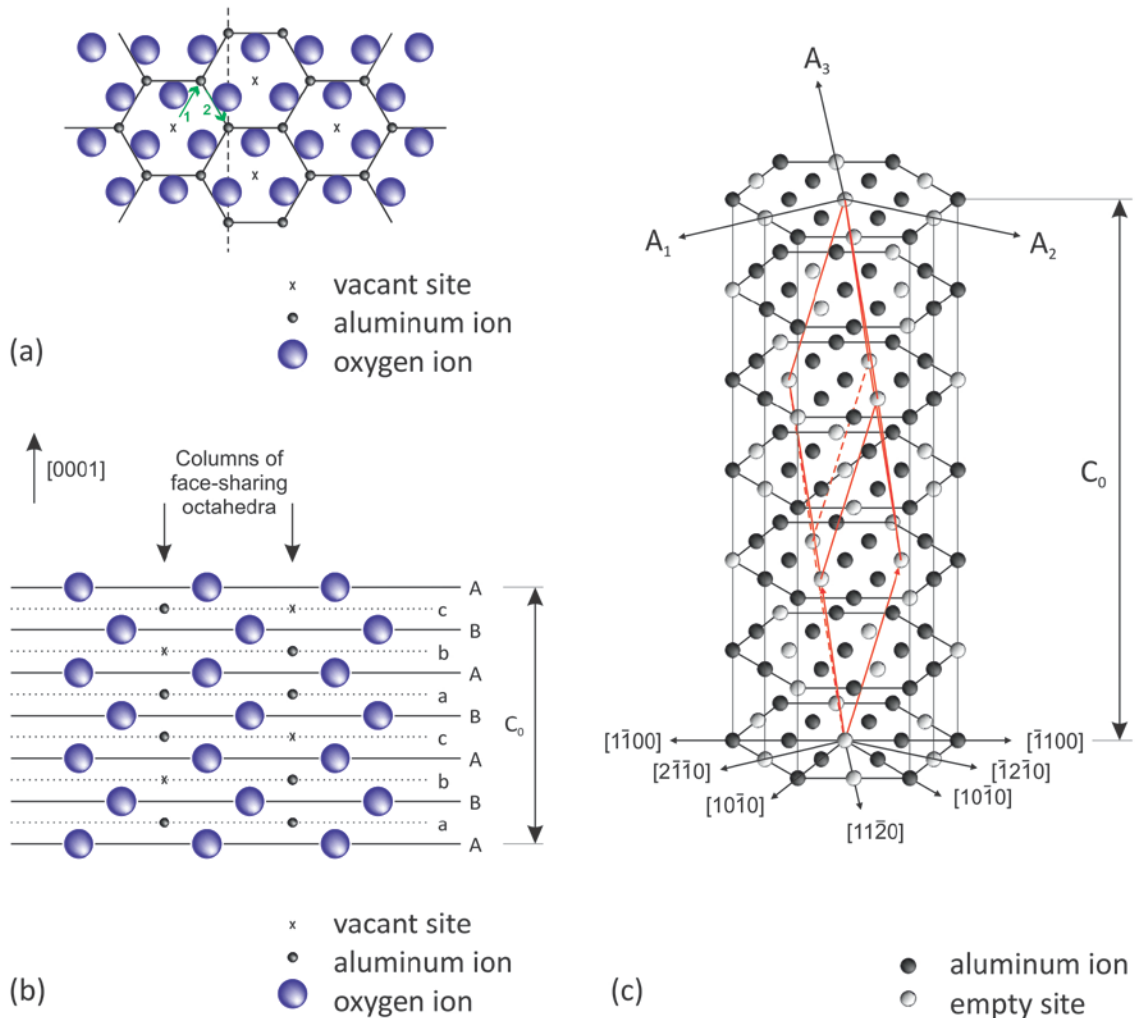
Figure 7: (a) Only one close packed anion plane is shown having a filling of 2/3 of octahedral sites in one base plain of corundum, (b) Plane shown by dashed line in Figure 7(a). Two thirds occupancy of the columns of octahedral sites are shown, and (c) Structural unit cell of corundum, showing only the cation sub-lattice. A1´s are the hexagonal basis vectors [modified after Chiang1996].

Figure 7c represents a schematic structural cell unit of the corundum phase and shows the cation sub-lattice alone, which repeats after three layers. According to Chiang *et al.*, the coulomb repulsion between aluminum ions causes each to move slightly toward adjacent unoccupied octahedral sites. As a result, the oxygen ions shift slightly from the idealized positions, thereby forming distorted unit cells rather than the ideal structures shown in Figure 7 [Chiang1996, Dörre1984].

Alumina exists, beside the thermodynamically stable corundum structured α–alumina phase, in a variety of metastable allotropic structures which are stable at room temperature like γ, δ, θ, η, χ and κ [Buerger1951, Vuorinen1992]. The metastable phases of interest in coatings produced via PVD techniques include mainly γ–, δ– and θ–alumina. It can be summarized that all of them show a less dense structure than α–alumina but as well a closed packed oxygen sub-lattice with different stacking sequences and different cation locations [Levin1998, Wriedt1985].

In general, γ–alumina is described as spinel structure (space group F$\bar{d}$3m) with oxygen anions in a face-centered cubic lattice, in which the aluminum cations possess not only octahedral but also tetrahedral coordination [Lippens1964, Zhou1964]. But γ–alumina has also been represented as a tetragonal structure (Hausmannite) [Paglia2005]. However, the main advantage of γ–alumina phase is that it can be formed by sputter deposition at relatively low substrate temperatures (350 to 550 °C) compared to the high temperatures (~700 °C) required for the stable α–alumina phase [Astrand2004, Chou1991, Cremer1999, Kohara2004, Zywitzki1997]. Furthermore, the γ–alumina exhibits a high thermal stability without any phase transformation up to 1000 °C [Levin1998]. Hence, a phase transformation to the α–phase can be avoided. This transition is associated with a cell volume decrease of approximately 8 % and would lead to cracking and failure of the coating [Vuorinen1992]. The results of the work published in Publication I show, that coatings containing an amorphous phase and a γ–alumina phase in as-deposited state do not transform to the α–alumina phase at a temperature lower than 1100 °C. Of course, this given temperature range concerning the formation of α–alumina may differ dependent on deposition technology, deposition temperatures, parameters of the thermal load and the present transition sequence. A commonly accepted transition sequence for sputtered alumina phases is [Levin1998, MacKenzie2000]

$$\text{amorphous } Al_2O_3 \;\rightarrow\; \gamma\text{–}Al_2O_3 \;\rightarrow\; \delta\text{–}Al_2O_3 \,/\, \theta\text{–}Al_2O_3 \;\rightarrow\; \alpha\text{–}Al_2O_3,$$
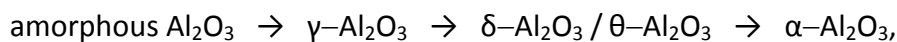
wherein the $\gamma-Al_2O_3$ transforms to $\delta-Al_2O_3$ and $\theta-Al_2O_3$ at temperatures of $700-800\,°C$, $\delta-Al_2O_3$ transforms to $\theta-Al_2O_3$ at temperatures of $900-1000\,°C$, and $\theta-Al_2O_3$ transforms at about $1000-1100\,°C$ into the stable $\alpha-Al_2O_3$ structure. These metastable so-called transition phases $\delta-$ and $\theta-$alumina are often observed during the transition from $\gamma-$alumina to $\alpha-$alumina. The term "transition", as opposed to "metastable", applies as the phase transition between them is irreversible and occurs with increasing temperature. $\delta-$alumina is reported to show a superstructure of $\gamma-$alumina and is of tetragonal or orthorhombic symmetry, while $\theta-$alumina exhibits a monoclinic symmetry belonging to the C2/m space group [Levin1998a, Levin1998b, MacKenzie2000]. However, many other variants of the sequence of phases are possible, since factors like particle size, heating rate, amount and kind of impurities and atmosphere can influence the kinetics of transformation. Within this thesis, it has been shown that there is a possibility to transform $\gamma-Al_2O_3$ formed at higher temperatures directly into $\alpha-Al_2O_3$ depending on the substrate material [Publication I]. This is in good agreement with results of Eklund *et al.*, where the initial fraction of $\gamma-Al_2O_3$ in the as-deposited coating has a major impact on the transition sequence [Eklund2009].

4.1 Alumina-chromia phase

Other compounds of corundum crystal structure include hematite (Fe_2O_3) and chromia (Cr_2O_3). In general, the structure of chromia is also called eskolaite and is isostructural with corundum, showing a relatively small lattice mismatch [Ramm2007a]. Based on the 2 : 3 cation : anion stoichiometry of these compounds, the metal cations that take on octahedral coordination must fill two-thirds of the available octahedral interstitial sites, as described above [Chiang1996]. Since the ionic radii of aluminum and chromium (0.057 nm for Al^{3+} and 0.064 nm for Cr^{3+}) are nearly similar, the ions of chromium can substitute for aluminum in the corundum structure and

aluminum substitutes for these ions in their oxides [Risic1993]. Hence, no gross disturbance of local charge distribution in the lattice is present. Therefore, it is not surprising that the system alumina-chromia shows an extensive area for solid solutions under thermodynamic equilibrium conditions. According to Sitte, this $(Al_xCr_{1-x})_2O_3$ solid solution is formed above 1200 °C over the whole composition range, see Figure 8 [Besmann2006, Bunting1931, Levin1964, Sitte1985]. The lattice parameter of such an $(Al_xCr_{1-x})_2O_3$ solid solution changes nearly linearly with composition according to Vegard´s behavior, owing to substitution of Cr^{3+} for Al^{3+} cations in the corundum structure [Bondioli2000, Ramm2007a, Rossi1970, Roy1972]. As it can be seen in Figure 8, a phase separation on the alumina-rich side of this solid solution to $\alpha-Al_2O_3$ and Cr_2O_3 is present at lower temperatures for equilibrium conditions [Sitte1985]. However, due to low ion diffusivity below 1000 °C this decomposition might be slow and difficult to observe. Moreover, this miscibility gap was not observed for coatings grown by physical vapor deposition techniques so far [Witthaut2000].
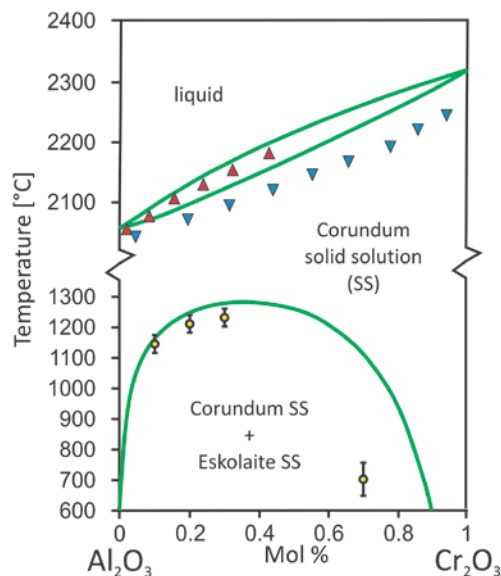

Figure 8: Quasibinary equilibrium phase diagram of $Al_2O_3-Cr_2O_3$: calculated by Besmann *et al.* [Besmann2006] with experimental solidus (▼) and liquidus (▲) data of Bunting [Bunting1931] and the miscibility gap (●) determined by Sitte [Sitte1985].

In this work, arc evaporated $(Al_xCr_{1-x})_2O_3$ coatings have been investigated and a remarkable thermal stability of this metastable $(Al_xCr_{1-x})_2O_3$ solid solution has been found, see Publication III. This is in good agreement with Witthaut *et al.*, presenting single-phase $(Al_xCr_{1-x})_2O_3$ solid solutions of various Al:Cr ratios having improved high temperature behavior as well [Witthaut2000]. Consequently, much work has recently been devoted to identifying ways of depositing crystalline corundum-type $(Al_xCr_{1-x})_2O_3$ coatings at low deposition temperatures and extending the Al:Cr ratio possible [Ashenford1999, Diechle2010, Khatibi2011, Khatibi2012, Najafi2013, Ramm2007b]. Very recently, Pohler *et al.* investigated corundum type $(Al_xCr_{1-x})_2O_3$ coatings with x = 0.25, 0.5, 0.7, and 0.85. These coatings were synthesized by arc evaporation at a comparatively low deposition temperature of ~500 °C and it was found that an isostructural corundum-type $(Al,Cr)_2O_3$ seed layer is able to stimulate the development of the desired corundum crystal structure [Pohler2014]. Hence, these stable coatings are interesting candidates for high-temperature applications.

5. Characterization techniques

In this work, the following main characterization techniques have been used to investigate Al_2O_3 and $(Al_xCr_{1-x})_2O_3$ coatings in the as-deposited state and during (in-situ) or after (ex-situ) exposure to thermal loads;

- X-ray diffraction to study the crystal structure of the coatings,
- scanning and transmission electron microscopy techniques to investigate their microstructure and crystallinity,
- elastic recoil detection analysis, Raman as well as energy-dispersive X-ray spectroscopy to study the elemental composition of the samples, and
- differential scanning calorimetry to gain information about the thermal stability and the change of morphology during thermal load of the coatings.

These methods are described in the following sections.

5.1 X-ray diffraction

X-ray diffraction (XRD) is a powerful, non-destructive characterization technique and applied for the structural identification of crystalline materials. It is very common, because it can be applied for almost any solid material without special preparation techniques. XRD, however, can also be used to obtain structural properties such as grain size, epitaxial relations, texture, or residual stress in coatings [Birkholz2006].

The information provided is based on the principle of an X-ray beam incident on a sample and subsequently diffracted beams coming out, which are detected. In

general, a monochromatic X-ray beam (e.g. Kα radiation of copper with a single wavelength of 1.54056 nm) is applied and scattered depending on lattice parameters of crystalline unit cells. These unit cells can be characterized in terms of size, shape, symmetry and the arrangement of atoms. Each atom in a periodic structure acts as a point of scattering for waves. However, either constructive or destructive interference wave patterns are generated, which are referred to as diffraction patterns. The requirements for constructive interference were mathematically formulated and described by W.H. Bragg and W.L. Bragg in their famous Bragg´s law as given below [Bragg1913] with a simplified model presented in Figure 9. Bragg's law with the geometrical correlation $n \cdot \lambda = 2 \cdot d \cdot \sin \theta$ is derived when the difference in path length of beams reflected from different atomic planes equals an integer number (n) of wavelengths λ. In this case constructive interference is observed. According to Bragg´s law illustrated in Figure 9, θ is attributed to the angle of the incoming X-rays and d (or d_{hkl}) to the lattice plane spacing which can be derived for the different Miller indices (hkl) and the dimensions of an unit cell. Equations for cubic and hexagonal crystals are also given in Figure 9. The information obtainable is primarily concerned with periodicity in a structure and can be categorized as position, intensity and shape of the diffraction peaks, whereby e.g. texture or grain size can be determined. Detailed descriptions and explanations of these influences as well as the diffraction analysis by X-rays itself can be found in literature [Birkholz2006, Cullity1978].
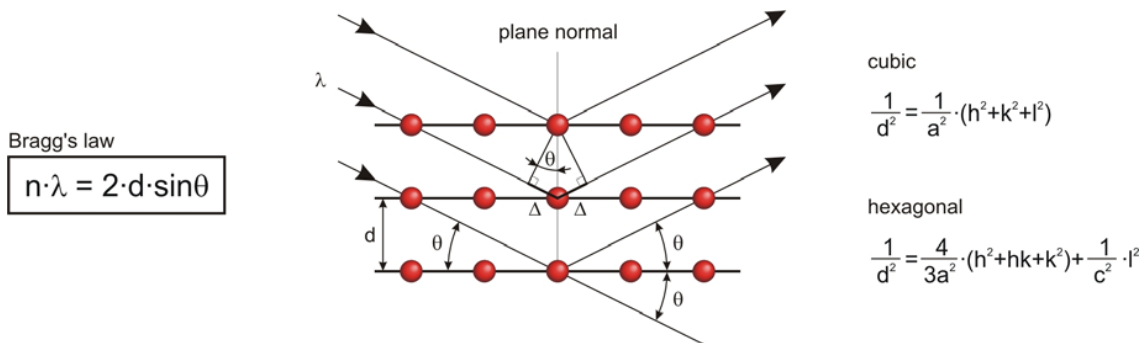
Figure 9: Bragg's law of X-ray diffraction with a schematic model and mathematical correlation between lattice plane spacing of given Miller indices and the unit cell dimensions for cubic and hexagonal crystals [Willmann2007]. n...integer, λ...wavelength (for X-rays from a CuKα source 1.54056 nm), d...interplanar spacing of the diffracting atomic planes, θ...diffraction angle.

In this thesis, XRD techniques were mainly used for phase identification of the coatings. These were conducted on either film/substrate compounds or powder samples of the coating. The measurements carried out where mostly done in the symmetrical Bragg-Brentano mode, where the sample rotates at an angle θ while the detector rotates at 2θ. In this case only the diffraction from crystallographic planes with the plane normal being parallel to the diffraction vector are investigated [Gissler1992, Ohring2002]. However, for the study of thin, polycrystalline coatings like in the present work, the so-called grazing-incidence mode can also be used, where in this work the angle (θ) of the incident beam was fixed at 2° relative to the sample surface, and only the diffraction angle, 2θ, was varied. This mode enables to minimize the penetration depth of the X-rays into the material in order to avoid a detection of peaks coming from the substrate located below the coating [Birkholz2006]. The phase identification of the grown and annealed coatings was conducted by comparing the measured peak positions with a reference position of the International Center for Diffraction Data, ICDD – JCPDS. Additionally, the peak broadening was taken into account, since useful information concerning grain size and a possibly existing

amorphous fraction can be detected. Due to the relatively large area hit by the incident X-ray beam, it can be said, that XRD is a macroscopic method to determine microstructure, crystallinity and grain size in contrary for example to transmission electron microscopy, which also was employed to confirm the results obtained by XRD and to study the coating morphology in more detail, see Publications II and III.

In this work, XRD analysis was done using an XRD diffractometer Siemens D500 in the Bragg–Brentano ($\theta-2\theta$) configuration with CuKα (λ=0.154056 nm) radiation. Additionally, a Bruker-AXS D8 Advance diffractometer at 2θ angles from 20 to 70° and an angle of incidence of 2° of the primary beam (CuKα radiation) was employed, see Publications II and III.

5.2 Scanning electron microscopy

Scanning electron microscopy (SEM) is a widely applied technique to provide high magnification images and compositional maps over a sample [Goldstein1981]. The technique is based on scanning a high energetic (a few keV to 50 keV) focused electron beam from a cathode filament across a sample surface in a raster scan pattern. The primary scanning electron beam interacts with the sample in several different ways and emits X-rays and electrons, which can be further divided into secondary electrons, back-scattered electrons and Auger electrons. The latter are used for Auger electron spectroscopy and thus not considered here [Gissler1992, Goldstein1981, Ohring2002, Verhoeven1986]. Secondary electrons generated from the inelastic interaction of the primary beam electrons with valence electrons of the atoms in the sample originate from a surface depth of not larger than a few nanometers due to their low energy (< 50 eV). Additional information can be obtained by detecting back-scattered electrons, providing mass contrast in the image, which is useful for qualitative phase identification. Since the amount of back-scattered electrons depends on the atomic number, a difference in brightness of the image is observed. The emitted X-ray

radiation can be used for quantitative elemental analysis by using proper chemical standards. This mode is called energy-dispersive X-ray spectroscopy (EDX), which uses a measurement of the energy of characteristic photons emitted from elements in the sample. Further information about SEM can be found in literature [Goldstein1981, Verhoeven1986].

In this work, SEM analysis was done by using a Zeiss EVO 50 equipped with an energy-dispersive X-ray analyzer (EDX, Oxford Instruments INCA) to study the coating morphology of Al_2O_3 coatings and the coating/substrate interface by examining fracture cross-sections, see Publication I.

5.3 Transmission electron microscopy

Transmission electron microscopy (TEM) is a powerful technique for investigating materials on the nanometer scale. The key benefit in using an electron source is that the wavelength is significantly smaller than other wave forms such as visible light or X-rays [Williams1996]. Since the TEM is the electron analogue of a conventional optical microscope operating with visible light, several optical lenses, a sample holder and an objective to form the primary image, a basic principle of a TEM can be drawn, if the light is exchanged by an electron source, the optical lenses are substituted by high quality electromagnetic lenses having a variable focal length in order to focus the electron beam and magnify or condense the image, and the sample holder is exchanged to a complex tilting- and translating system featuring a very high mechanical stability. Additionally, a detector like a fluorescent screen or a charge coupled device (CCD) camera is required which converts electrons into light [Fultz2002]. Consequently, a skilled operator is needed, too. Compared to the above described SEM technique, TEM is able to produce images with superior resolution. Another main advantage of a TEM over other microscopes is that it can simultaneously give information in real space (in the imaging mode) and reciprocal space (in the

diffraction mode). Therefore, the samples that contain the structural features of interest have to fulfill certain requirements such as electron transparency, as a thick sample would cause too much interactions leaving no intensity of the transmitted beam.

- Sample preparation

Samples are generally prepared by a combination of mechanical abrasion and ion etching in order to minimize the sample thickness. It has to be taken into account, that such a thin sample can easily be damaged, not only by mechanical forces due to the thinning techniques but also by the thermal energy that is required to remove material and implantation effects due to the ion etching [Scheu2003, Williams1996]. For example during the preparation process of samples containing metastable phases of Al_2O_3 there exists a risk that a phase transformation may occur, since the electron beam of a TEM possesses kinetic energies of 120 to 300 kV. TEM samples can be prepared using various different methods. The cross-sectional Al_2O_3 samples discussed in Publication II were prepared following the procedure described by Strecker *et al.* [Strecker1993]. For the final thinning to electron transparency, the samples were ion-milled with argon ions at 3 kV using a Gatan PIPS until perforation was obtained. In the last step, low energy ion-milling was performed at 0.9, 0.6 and 0.3 kV for 20 min each, to minimize beam damage of the sample. The $(Al_xCr_{1-x})_2O_3$ samples studied in Publication III were prepared using a FEI NOVA 200DB FIB/SEM (focused ion beam) instrument with an OMNIPROBE in-situ lift-out technique using a standard FIB preparation according to Giannuzzi *et al.* [Giannuzzi1999].

- Imaging mode

There are several different imaging modes in TEM established. The most common way to obtain an image is to detect the directly transmitted beam exclusively and to block the scattered electrons by an aperture. This mode is called bright-field (BF) imaging as illustrated in Figure 10. For BF imaging, which is also referred to as

conventional TEM, regions of the sample being thinner or exhibiting a lower atomic number appear brighter than the thick ones due to the lower probability for scattering. Furthermore, the BF imaging mode is also sensitive to lattice defects, such as point defects or dislocations as the disorientation of crystalline planes causes intensity variations in the resulting image. In the dark-field (DF) imaging mode, the directly transmitted electrons are blocked, whereas the diffracted electrons are allowed to pass through an objective aperture. This mode allows an investigation of the crystal distribution and orientation into the sample, since only a crystal that satisfies a specific diffraction condition becomes bright in the DF image [Gissler1992, Krumeich2014].
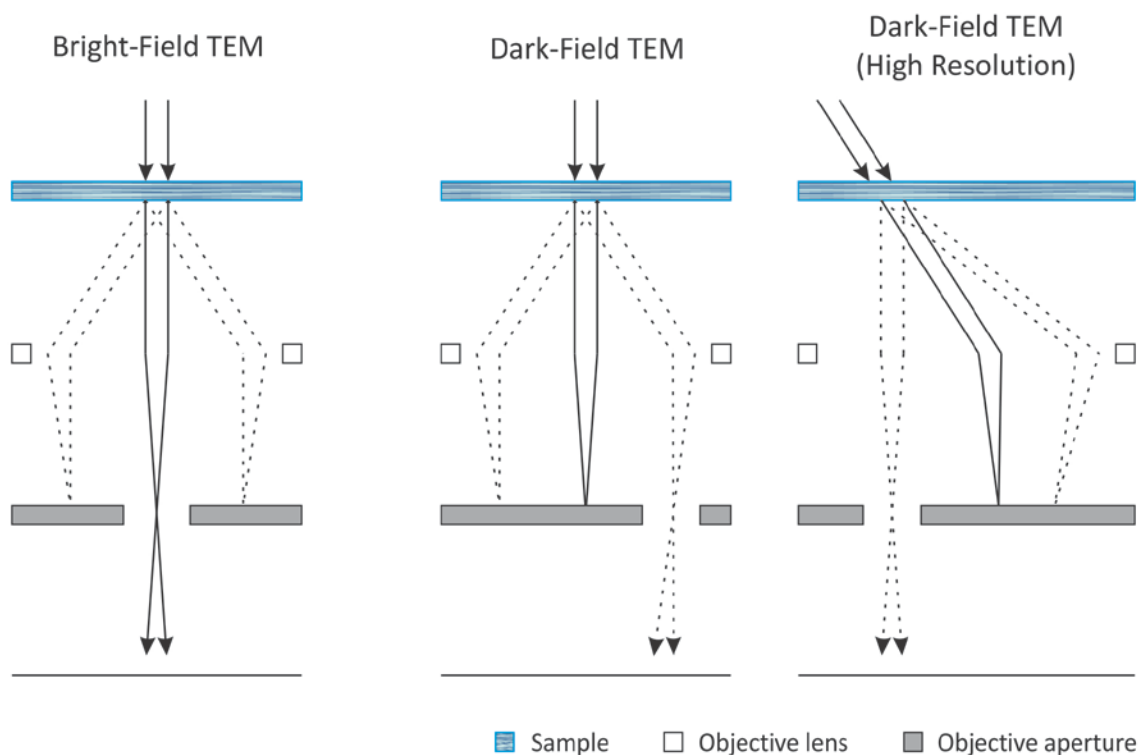

Figure 10: Comparison of TEM bright-field and dark-field imaging (modified after Williams *et al.* [Williams1996]).

By imaging using a combination of the directly transmitted beam and diffracted beams, it is possible to produce images with lattice resolution due to phase contrast. The phase contrast can be described as interference of the diffracted beams with the

direct beam. This technique is known as high resolution TEM (HRTEM) and is also schematically illustrated in Figure 10. However, if the point resolution of the microscope is sufficiently high and a suitable crystalline sample is oriented along a zone axis, then HRTEM images with detectable features as small as the unit cell of a crystal are obtained [O´Keefe1978]. Publication II presents several HRTEM images showing different crystalline modifications of Al_2O_3.

- Diffraction mode

Furthermore, TEM investigations can not only be used for imaging but also for diffraction studies. In general, when the electron beam passes only one crystal, then a single diffraction pattern arises, as it is shown schematically in Figure 11a. Contrary, a polycrystalline sample of the same material contains multiple grains and therefore shows a ring pattern (Figure 11c). Subsequently, these rings can be attributed to certain lattice planes and assigned with indices in respect of the present type of unit cell. Any kind of intermediate state of crystallinity between single crystalline and polycrystalline diffraction patterns can appear, which leads to reflections of several randomly oriented microcrystals. Some of the coatings investigated in Publication II and III show preferred orientation and hence exhibit several superimposed diffraction patterns, but with only certain orientations present.
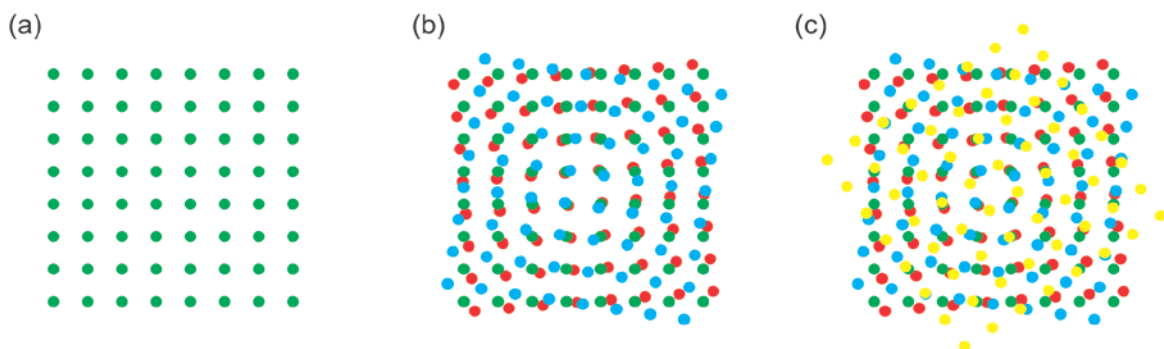

Figure 11: (a) Diffraction pattern of a single crystal, (b) Three slightly rotated single crystals, and (c) Four single crystals.

Diffraction pattern provide information regarding the crystal lattice spacings, symmetry, orientation and distribution of grain sizes. Individual areas of the coating can be selected through the use of a selected-area aperture, allowing analysis of the diffraction pattern from different areas. This type of diffraction is called selected area electron diffraction (SAED), which is useful for phase identification and provides information that is equivalent to XRD [Fultz2002]. The use of SAED pattern in combination with BF imaging provides information concerning the structure and is often presented together, see Publication II and Publication III.

- Energy-dispersive spectroscopy

Another analytical capability is energy-dispersive spectroscopy (EDX), where, similar to SEM, elemental identification is achieved through measurement of characteristic X-ray energies. Since in this work light elements like oxygen had to be detected, which were difficult to quantify with EDX, mainly electron energy loss spectroscopy was employed instead of EDS. Nevertheless, further information concerning EDX is given in Section 5.6 (Energy dispersive X-ray spectroscopy).

- Electron energy loss spectroscopy

An important analytical tool for the characterization of materials in terms of elemental composition is the electron energy loss spectroscopy (EELS), which is based upon the atomic transition during the interaction between an incident electron and a sample electron. The inelastic interactions need energy that is taken from the electron in the incoming beam. As a result, the electron suffers a loss of energy which can be measured by EELS. This can be done by using a magnetic prism spectrometer located after the main imaging lenses, which can collect the transmitted beam and disperse the electrons according to energy loss. Since each element features characteristic ionization energy, the energy loss is also characteristic for an element and can thus be used for characterization of elements within a sample.

Figure 12a shows a schematic diagram of a typical EEL spectrum, which displays the scattered electron intensity as a function of the decrease in kinetic energy, the energy loss E, of the transmitted electrons. In general, an EEL spectrum essentially comprises three different signals; the so-called zero-loss peak, the low-loss region, and the high-loss region. The first peak appears at an energy loss of zero and is therefore called zero-loss peak. This is by far the most intense signal and contains all electrons that have passed the sample without any interaction or with elastic interaction only, but is not important for spectroscopy. The low-loss region includes the energy losses between the zero-loss peak and about $50-100$ eV, where electrons that have plasmon oscillations occur. These plasmon peaks are the predominant feature, since the plasmon generation is the most frequent inelastic interaction of the electrons with the sample. Plasmon excitation arises from the fact that outer shell electrons, conduction electrons or valence electrons, in metals or semiconductors and insulators, respectively, are only weakly bound to atoms but are coupled to each other by electrostatic forces. However, the intensity of this peak is governed by the density of the valence electrons and by its width by the rate of decay of this resonant mode. Hence, the sample thickness can be derived. The more intense this plasmon peak is, the thicker the investigated sample area has to be. However, the high-loss region of the EEL spectrum extends from $50-100$ eV to several thousand electron volts, where ionization edges are present corresponding to the ionization of core shell electrons. These ionization edges, which appear at electron losses that are typical to a specific element, are illustrated as well-defined peaks in the EEL spectrum above the background. The onset of such an ionization edge corresponds to a threshold energy that is necessary to promote a core shell electron from its energetically favored ground level to the lowest unoccupied level. This energy is specific for a certain shell and for a certain element. This region therefore more reflects the atomic character of the sample. The spectrum which is attributed to the electron transition of core shell to the valence band is called energy-loss near-edge structure (ELNES) and is sensitive to chemical bonding effects and valence state information. The region in Figure 12 marked as "EXELFS" provides information about the local coordination of an atom and

is the abbreviation of extended energy loss fine structure [Brydson2001, Brydson2014, Egerton2009, Krumeich2014].
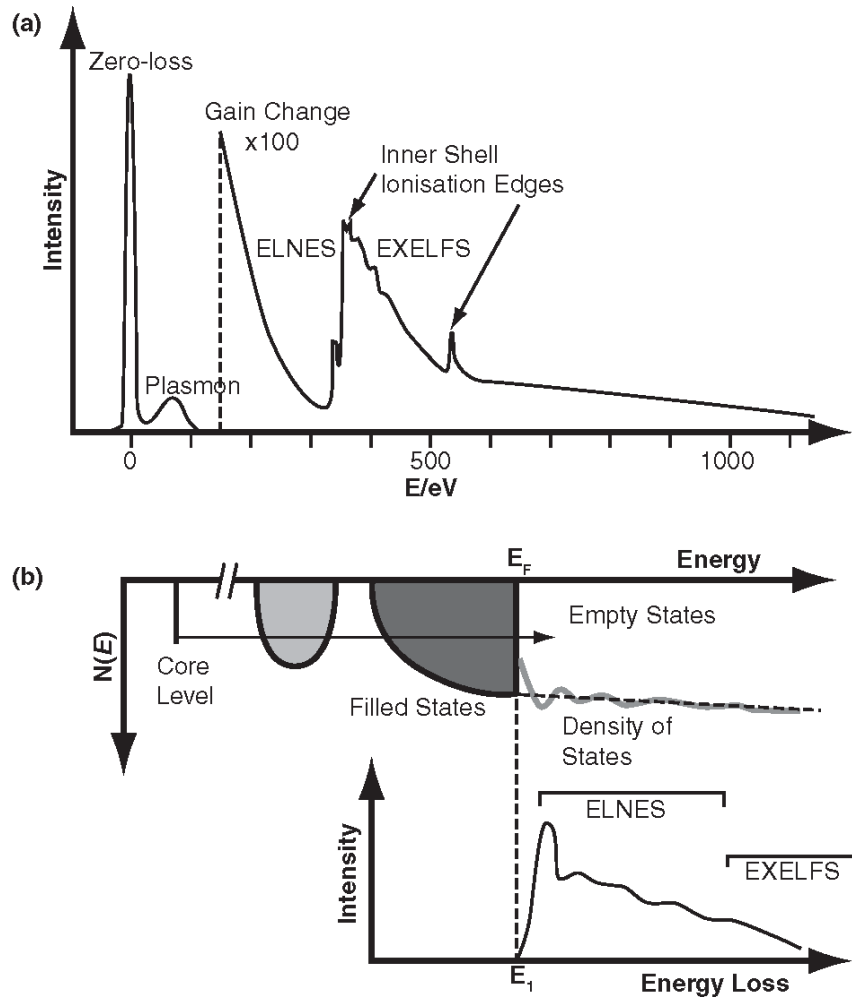

Figure 12:   Schematic diagram of (a) a general EEL spectrum showing all of the observable features and (b) an enlarged version the (background-subtracted) ELNES intensity indicating how it reflects transitions from atomic core levels to the unoccupied density of states above the Fermi level [Brydson2014].

In this study, EELS/ELNES measurements were performed at 300 kV in diffraction mode using a SAED aperture. To verify that the coating structure of the transformation-sensitive Al_2O_3 was in fact not altered by the electron bombardment, also EELS measurements at 80 kV for selected samples were conducted, which

revealed the same ELNES features. Further details are given in Publication II, where the metastable $\gamma-$, $\delta-$ and the stable $\alpha-$modification of Al_2O_3 was investigated.

- Energy-filtered transmission electron microscopy

In energy-filtered transmission electron microscopy (EFTEM), the parallel beam imaging mode in a TEM is coupled with principles of EELS to yield a filtered image or an elemental map. Both, EELS and EFTEM use the inelastic scattering of electrons, while EELS requires a spectrometer and EFTEM needs an energy filter. These filters use a series of magnetic prisms or magnetic sectors. If EFTEM is used for elemental mapping, a so-called energy slit is used to select a particular energy window. This window is characterized on one hand by the position along the energy axis and on the other by its width. Furthermore, it corresponds to an element-specific energy loss, which can be attributed to the core loss edge. Hence, a projection along this energy axis yields an image containing electrons of only that particular preselected energy range. After an appropriate subtraction of the background, the EFTEM image will show the distribution of that particular element in the sample in nanometer resolution.

EFTEM using a Gatan image filter (GIF) in imaging mode was employed to obtain a series of elemental distribution maps of Al, Cr and O of the investigated $(Al_xCr_{1-x})_2O_3$ coatings, which are presented in Publication III.

More detailed information on the various TEM techniques can be found in References [Fultz2002, Ohring2002, Thomas1979, Williams1996a-d].

5.4 Elastic recoil detection analysis

Elastic recoil detection analysis (ERDA) is used for quantification of the elemental composition of a coating. By exposing the sample to a beam of highly

energetic ions (in this work, Cl^{7+} ions with an energy of 35 MeV) at a certain angle with respect to the sample surface, the atoms of the coating are forwardly scattered away from the surface (recoiled) through elastic collisions. By detecting the mass and energy of these recoiled atoms by a Bragg ionization chamber, a depth-resolved composition profile is obtained. The big advantage of this method in comparison to EDX which is described in Section 5.6 (Energy dispersive X-ray spectroscopy), is that ERDA allows a reliable quantification of compounds which consist of relatively light elements in thin film samples [Tesmer1995]. More details concerning this method are found in References [Bohne1998, Bubert2002].

In this work, the absolute atomic concentration of aluminum, chromium, oxygen and hydrogen of the Al_2O_3 and $(Al_xCr_{1-x})_2O_3$ coatings was determined by using a 35 MeV Cl^{7+} ion beam with an analyzed area of 1.5×1.5 mm^2 and a depth of information of ~600 nm. In addition, the ERDA results have been cross-checked by EDX, see Publication I and Publication III.

5.5 Raman spectroscopy

Raman spectroscopy is a non-destructive technique used for structural and chemical characterization. It deals with the interaction of light and optical oscillations of molecules or crystals [Brundle1992, McCreery2000, Smith2005]. This technique is based on the so-called Raman effect, where a monochromatic light beam impinges on a sample and after collision with a molecule or crystal, a fraction of the incident photons is scattered either with the same frequency (Rayleigh scattering) or with a different material specific frequency (Raman scattering). However, some photons transfer their energy to the sample exciting vibrational modes of the crystal lattice (Stokes scattering) or gain energy because of annihilation of vibrational modes (anti-Stokes scattering). Both, Stokes and anti-Stokes peaks are symmetrically positioned with respect to the Rayleigh scattering, but are of different intensities. Furthermore,

anti-Stokes scattering depends on the existence of thermally activated lattice vibrations and, thus, yields a very weak peak intensity, whereas Stokes scattering is only less influenced by the temperature [Weber2000]. The Raman spectra are usually illustrated in terms of the so-called Raman shift as a function of wave number in reciprocal centimeters, wherein the Raman shift can be defined by the difference between the frequency of the Rayleigh scattering and the Stokes scattering. The Raman shift depends on the crystallinity, the defects, structural disorder and stresses in materials. Furthermore, quantitative information can be obtained from the peak intensities, whereas the peak position provides information about the stoichiometry. Hence, Raman spectroscopy can also be used to identify materials by comparing the measured spectrum with a database containing reference spectra [Brundle1992, McCreery2000, Parker1990, Smith2005].

In this work, a HORIBA Jobin Yvon Labram-HR800 for sample excitation and a CCD-camera with 100× objective for signal detection was used complementary to XRD experiments, see Publication I. Additionally, a Dilor LABRAM confocal Raman spectrometer was employed to obtain the Raman spectra, see Publication III.

5.6 Energy dispersive X-ray spectroscopy

Energy dispersive X-ray spectroscopy (EDX) is a fast and common method to determine an elemental composition of materials. It is based on the interaction of the primary electron beam with the sample, which generates an element specific X-ray spectrum. This can be used for quantitative elemental analysis if proper chemical standards are used and the elements are not too light [Bubert2002]. For a short description of EDX, see also Section 5.2 (Scanning electron microscopy) and Section 5.3 (Transmission electron microscopy). Within this thesis, a Zeiss EVO 50 SEM equipped with an EDX analyzer (Oxford Instruments INCA) was employed for chemical analysis of

the coatings studied to cross-check the results obtained by ERDA, see Publication I and Publication III.

5.7 Differential scanning calorimetry

Differential scanning calorimetry (DSC) is a common thermo-analytical technique to determine in-situ, for example, temperatures of phase transformation, crystallization and oxidation by measuring an heat flow to or from a sample. The heat-flow is detected by a differential thermocouple that measures the temperature difference between the sample and an inert reference sample. Both, the sample and the reference sample are exposed to the same programmable thermal heating procedure and to a specified atmosphere (e.g. argon for an inert environment). Subsequently, the heat flow rate is continuously monitored during altering the temperature (dynamic) or time (isothermal) [Brown1998]. Thus, the enthalpy generated or consumed during a physical or chemical reaction in the sample material can either increase, in case of endothermic reactions such as melting or evaporation, or decrease, in case of exothermic reactions such as crystallization or oxidation.

In order to avoid substrate interference during the DSC measurement, powder specimens of the coatings have been prepared for this experiment. There, the coatings have been deposited on iron-foil which was chemically dissolved in nitric acid after deposition. The remaining coating material was grinded manually to powder. For the in-situ DSC investigation of the microstructural changes of the coatings with temperature and time, a Netzsch-STA 409C thermal analysis instrument (see Publication I) and a Setaram LabsysEvo (see Publication III) was employed to investigate phase transformations of Al_2O_3 and $(Al_xCr_{1-x})_2O_3$ coatings. But also ex-situ techniques, like post-deposition annealing and subsequent investigations were performed to compare the material response to the applied temperature program.

Further results obtained for Al_2O_3 and $(Al_xCr_{1-x})_2O_3$ coatings are given in Publications I and III, respectively.

6. Summary and conclusions

Within the present thesis, the thermal stability of sputtered and arc evaporated alumina-based coating materials was investigated in terms of changes of their morphology during thermal load. Since alumina exists, besides the thermally stable corundum structured $\alpha-Al_2O_3$ in a variety of metastable modifications, for their application as protective coatings on cutting tools, the knowledge of their thermal stability is of vital importance. Therefore, different metastable Al_2O_3 coatings were produced by magnetron sputtering and the transformation into the $\alpha-Al_2O_3$ phase was investigated in detail. In order to meet the demand of low deposition temperatures and thus to synthesize a protective coating for thermally sensitive cutting tools, in a second attempt the $\alpha-Al_2O_3$ phase was stabilized by the isostructural Cr_2O_3 phase, forming a corundum-based $(Al_xCr_{1-x})_2O_3$ solid solution. The solid solutions synthesized by arc evaporation were investigated and the thermal stability against decomposition was also determined.

Al_2O_3 coatings were deposited at a substrate temperature of 640 °C by using an industrial scale magnetron sputter system under different ion bombardment conditions. The coatings deposited onto silicon substrates and under low ion bombardment conditions exhibited in the as deposited state small metastable $\gamma-Al_2O_3$ grains embedded in an amorphous phase, with higher $\gamma-Al_2O_3$ content close to the interface to the silicon substrate. The grain size at the region close to the interface was much larger than that of the remaining coating. During annealing, growth of the $\gamma-Al_2O_3$ phase was promoted and after an annealing treatment at 1000 °C for 12 h the coating became fully crystalline, consisting of rather small $\gamma-Al_2O_3$ grains, but still no transformation to $\alpha-Al_2O_3$ was detected. In contrast, the coating deposited at enhanced ion bombardment conditions showed clear evidence for $\gamma-Al_2O_3$ formation

in the upper part of the coating with a grain size much larger than the coating deposited under low ion bombardment conditions, but these coatings were predominantly amorphous at the interface region. During annealing, nucleation of $\alpha-Al_2O_3$ started at the coating surface, proceeding towards the interface. After the treatment at 1000 °C for 12 h, still an area of $\gamma-Al_2O_3$ grains, not yet transformed to $\alpha-Al_2O_3$, was visible close to the substrate.

Annealing of metastable Al_2O_3 coatings deposited on silicon substrate results in the irreversible formation of the thermodynamically stable $\alpha-Al_2O_3$ phase. However, it could be shown that the transformation sequence is essentially determined by the substrate material. For coatings deposited on iron foil, it seemed that the formation of $\gamma-Al_2O_3$ is fostered. While coatings on silicon transformed directly from the metastable $\gamma-Al_2O_3$ into the $\alpha-Al_2O_3$ phase, the coating deposited on iron foil exhibited the so-called transition phase $\delta-Al_2O_3$. However, the coatings deposited on iron foil under low ion bombardment conditions transformed to the stable $\alpha-Al_2O_3$ modification at ~1150 °C, while the transformation of the coating deposited under enhanced ion bombardment conditions is retarded to ~1260 °C.

Furthermore, arc evaporated corundum-based $(Al_xCr_{1-x})_2O_3$ solid solution coatings with an Al/Cr atomic ratio of ~1 were investigated. The coatings were deposited at 550 °C and are dominated by the corundum-based $(Al_xCr_{1-x})_2O_3$ solid solution. Additionally, a smaller fraction of the cubic $(Al_xCr_{1-x})_2O_3$ phase as well as metallic chromium and an aluminum-rich amorphous phase originating from droplets could be detected. However, after an annealing treatment at 1050 °C for 2 h no unambiguous evidence for spinodal decomposition of the corundum- and cubic $(Al_xCr_{1-x})_2O_3$ solid solutions was found. However, a transformation of the cubic $(Al_xCr_{1-x})_2O_3$ fraction to the corundum-based $(Al_xCr_{1-x})_2O_3$ phase occurred at elevated temperatures, while the latter was stable during an annealing treatment at 1050 °C for 2 h. Hence, it can be concluded that the demand for protective coatings, which can be synthesized at low deposition temperatures and exhibit a remarkable thermal stability,

is fulfilled with the metastable corundum-based $(Al_xCr_{1-x})_2O_3$ solid solutions. These coatings might be interesting candidates for high-temperature and cutting applications, where high performance materials are needed.

7. Bibliography

Anders2008:   A. Anders, Cathodic Arcs: From Fractal Spots to Energetic Condensation, Springer, New York, 2008.

Anders2010:   A. Anders, Thin Solid Films 518 (2010) 4087–4090.

Ashenford1999:   D.E. Ashenford, F. Long, W.E. Hagston, B. Lunn, A. Matthews, Surface and Coatings Technology 116–119 (1999) 699−704.

Astrand2004:   A. Astrand, T.I. Selinder, F. Fietzke, H. Klostermann, Surface and Coatings Technology 188–189 (2004) 186–192.

Barna1998:   P.B. Barna, M. Adamik, Thin Solid Films 317 (1998) 27–33.

Besmann2006:   T.M. Besmann, N.S. Kulkarni, K.E. Spear, Journal of the American Ceramic Society 89 (2006) 638–644.

Birkholz2006:   M. Birkholz, Thin Film Analysis by X–ray Scattering, Wiley–VCH, Weinheim, 2006.

Bohne1998:   W. Bohne, J. Röhrich, G. Röschert, Nuclear Instruments and Methods in Physics Research B 139 (1998) 219–224.

Bondioli2000:   F. Bondioli, A.M. Ferrari, C. Leonelli, T. Manfredini, Journal of the American Ceramic Society 83 (8) (2000) 2036–2040.

Bragg1913:   W.H. Bragg, W.L. Bragg, Proceedings of the Royal Society of London. Series A, Containing Papers of a Mathematical and Physical Character 88 (605) (1913) 428–438.

Bragg1916:   W.H. Bragg and W.L. Bragg: X–Rays and Crystal Structure, Bell & Sons, London, 1916, pp. 169.

Brown1998:   M.E. Brown, Handbook of Thermal Analysis and Calorimetry, Elsevier Science B.V., Amsterdam, 1998.

Brundle1992:   R.C. Brundle, C.A. Evans Jr., S. Wilson, Encyclopedia of Materials Characterization, Butterworth – Heinemann, Boston, 1992.

Brydson2001:   R. Brydson, Electron Energy Loss Spectroscopy, BIOS Scientific Publishers, London, 2001.

Brydson2014:   R. Brydson, A. Brown, L.G. Benning, Analytical Transmission Electron Microscopy, Reviews in Mineralogy Geochemistry, Vol. 78, 2014, pp. 2019–269.

Bubert2002:   H. Bubert, H. Jenett, Surface and Thin Film Analysis, Wiley–VCH, Weinheim, 2002.

Buerger1951:   M.J. Buerger, Phase Transformations in Solids, John Wiley & Sons, New York, 1951, pp. 202.

Bunshah1982:   R.F. Bunshah, Deposition Technologies for Films and Coatings – Developments and Applications, Noyes Publications, Park Ridge, New Jersey, 1982.

Bunshah2001:   R.F. Bunshah in: R.F. Bunshah, G.M. McGuire, S.M. Rossnagel, eds., Handbook of Hard Coatings, Noyes Publications, New Jersey, 2001.

Bunting1931:   E.N. Bunting, Journal of Research of the National Bureau of Standards 6 (1931) 947–949.

Chapman1980:   B. Chapman, Glow discharge processes, John Wiley & Sons, New York, 1980.

Chiang1996:   Y.–M. Chiang in: Physical Ceramics: Principles for Ceramic Science and Engineering, D.P. Birnie, W.D. Kingery, eds., John Wiley & Sons, New York, 1996.

Chou1991:   T.C. Chou, D. Adamson, J. Mardinly, T.G. Nieh, Thin Solid Films 2005 (1991) 131–139.

Choy2000:   K.L. Choy in: 'Handbook of Nanostructured Materials and Nanotechnology', Vol. 1, H.S. Nalwa, eds. , Academic Press, San Diego, 2000, pp. 57–170.

Cremer1999:   R. Cremer, M. Witthaut, D. Neuschütz, G. Erkens, T. Leyendecker, M. Feldhege, Surface and Coatings Technology 120 (1999) 213−218.

Cullity1978:   B.D. Cullity, Elements of X–Ray Diffraction, Addison–Wesley Publishing Company Inc., 1978.

Diechle2010:   D. Diechle, M. Stueber, H. Leiste, S. Ulrich, V. Schier, Surface and Coatings Technology 204 (2010) 3258–3264.

Dörre1984:   E. Dörre, H. Hübner, Alumina: Materials Research and Engineering, Springer Verlag, Berlin, Heidelberg, New York, Tokyo, pp. 184.

Egerton2009:   R.F. Egerton, Reports on Progress in Physics 72 (2009) 016502.

Eklund2009:   P. Eklund, M. Sridharan, G. Singh, J. Bøttiger, Plasma Processes and Polymers 6 (2009) 907–911.

Ensinger1997:   W. Ensinger, Nuclear Instruments and Methods in Physics Research B 127–128 (1997) 796–808.

Frey1995:   H. Frey, Vakuumbeschichtung 1, Plasmaphysik – Plasmadiagnostik – Analytik, VDI Verlag, Düsseldorf, 1995.

Fultz2002:   B. Fultz, J. Howe, Transmission Electron Microscopy and Diffractometry of Materials, 2nd Edition, Springer, Berlin, 2002.

Giannuzzi1999:   L.A. Giannuzzi, F.A. Stevie, Micron 30 (1999) 197–204.

Gissler1992:   W. Gissler, H.A. Jehn, Advanced Techniques for Surface Engineering, Kluwer Academic Publishers, Dordrecht, 1992.

Gold2014:   National Mining Association, 'The History of Gold', Washington. http://www.nma.org/pdf/gold/gold_history.pdf, August 2014.

Goldstein1981:   J.I. Goldstein, D.E. Newbury, P. Echlin, D.C. Joy, C. Fiori, E. Lifshin, Scanning Electron Microscopy and X–ray Microanalysis, Plenum Press, New York, 1981.

Greene1993:   J.E. Greene in: Handbook of Crystal Growth, Vol. 1, D.T.J. Hurleed, Elsevier Science Publishers, Amsterdam, 1993, pp. 640.

Greene1994:   J.E. Greene, Handbook of Deposition Technologies for Films and Coatings, Noyes Publications, Park Ridge, New Jersey, 1994, pp. 681.

Greene2009:   J.E. Greene, Thin Film Nucleation, Growth and Microstructure Evolution, AVScourse at the ICMCTF, San Diego, 2009.

Haasen1978:   P. Haasen, Physical Metallurgy, Cambridge University Press, London, 1978.

Häfer1987:   R.A. Häfer, Oberflächen– und Dünnschicht–Technologie, Teil I: Beschichtungen von Oberflächen, Springer Verlag, Berlin, 1987.

Hocking1989:   M.G. Hocking, V. Vasantasree, P.S. Sidky, Metallic and Ceramic Coatings, Wiley, New York, 1989.

Hörling2002:   A. Hörling, L. Hultman, M. Odén, J. Sjölén, L. Karlsson, Journal of Vacuum Science & Technology A 20 (2002) 1815–1823.

Hultman2000:   L. Hultman, Vacuum 57 (2000) 1–30.

Hunt1973:   L. B. Hunt, Gold Bulletin 6 (1) (1973) 16–27.

Jehn1992:   H.A. Jehn in: Advanced Techniques for Surface Engineering, W. Gissler, H.A. Jehn, eds., Kluwer Academic Publisher, Dordrecht, 1992, pp. 5–29.

Kathrein2003:   M. Kathrein, W. Schintlmeister, W. Wallgram, U. Schleinkofer, Surface and Coatings Technology 163–164 (2003) 181–188.

Khatibi2011:   A. Khatibi, J. Palisaitis, C. Höglund, A. Eriksson, P.O.Å. Persson, J. Jensen, J. Birch, P. Eklund, L. Hultman, Thin Solid Films 519 (2011) 2426–2429.

Khatibi2012:   A. Khatibi, J. Sjölen, G. Greczynski, J. Jensen, P. Eklund, L. Hultman, Acta Materialia 60 (19) (2012) 6494–6507.

Kienel1995:   G. Kienel, K. Röll, Vakuumbeschichtung 2, Verfahren und Anlagen, VDI Verlag, Düsseldorf, 1995.

Kohara2004:   T. Kohara, H. Tamagaki, Y. Ikari, H. Fujii, Surface and Coatings Technology 185 (2004) 166–171.

Konuma1992:   M. Konuma, Film Deposition by Plasma Techniques, 10, Springer
                   Verlag, Berlin Heidelberg, 1992.

Krumeich2014:   F. Krumeich, Properties of Electrons, their Interaction with Matter
                   and Applications in Electron Microscopy, Laboratory of Inorganic
                   Chemistry, ETH Zurich.

                   http://www.microscopy.ethz.ch/downloads/Interactions.pdf,
                   October 2014.

Lee1985:   W.E. Lee, K.P.D. Lagerlof, Journal of Electron Microscopy
                   Technique 2 (1985) 247–258.

Levin1964:   E.M. Levin, C.R. Robbins, H.F. McMurdie, Phase Diagrams for
                   Ceramists, Vol I–XIII; The American Ceramic Society, 1964–2002.

Levin1998a: I. Levin, D. Brandon, Journal of the American Ceramic Society 81
                   (8) (1998) 1995–2012.

Levin1998b: I. Levin, A. Berner, C. Scheu, H. Müllejans, D.G. Brandon,
                   Mikrochimica Acta 15 (1998) 93–96.

Lippens1964:   B.C. Lippens, J.H. De Boer, Acta Crystallographica 17 (1964) 1312–
                   1321.

MacKenzie2000:   K.J.D. MacKenzie, J. Temuujin, M.E. Smith, P. Angerer,
                   Y. Kameshima, Thermochimica Acta 359 (2000) 87–94.

Mattox1989:   D.M. Mattox, Journal of Vacuum Science & Technology. A 7 (3)
                   (1989) 1105–1114.

Mattox2010:   D.M. Mattox, Handbook of Physical Vapor Deposition (PVD)
                   Processing, 2nd edition, Elsevier, Oxford, 2010.

Mayrhofer2001:   P.H. Mayrhofer, Ph.D Thesis, Montanuniversität Leoben, 2001.

Mayrhofer2006:   P.H. Mayrhofer, C. Mitterer, L. Hultman, H. Clemens, Progress in Materials Science. 51 (2006) 1032–1114.

McCreery2000:   R. McCreery, Raman Spectroscopy for Chemical Analysis of Chemical Analysis,Vol. 157, John Wiley Inc., New York, 2000.

Messier1984:   R. Messier, A.P. Giri, R.A. Roy, Journal of Vacuum Science & Technology A 2 (1984) 500–503.

Mitterer2014:   C. Mitterer in: PVD and CVD Hard Coatings: Comprehensive Hard Metals, V.K. Sarin, L. Llanes, D. Mari, eds., Elsevier, 2014, pp. 449–467.

Moll1992:   E. Moll in: Advanced Techniques for Surface Engineering, W. Gissler, H.A. Jehn, eds., Kluwer Academic Publisher, Dordrecht, 1992, pp. 181.

Moser2008:   M. Moser, Ph.D. Thesis, Montanuniversität Leoben, 2008.

Movchan1969:   B.A. Movchan, A.V. Demchishin, The Physics of Metals and Metallography 28 (1969) 653–660.

Najafi2013:   H. Najafi, A. Karimi, P. Dessarzin, M. Morstein, Surface and Coatings Technology 214 (2013) 46–52.

Nicholson1979:   E. D. Nicholson, Gold Bulletin 12 (4) (1979) 161–166.

Oddy1981:   A. Oddy, Gold Bulletin 14 (2) (1981) 75–79.

Ohring1991:   M. Ohring, The Materials Science of Thin Films, Academic Press, San Diego, 1991.

Ohring2002:   M. Ohring, Materials Science of Thin Films – Deposition & Structure, Academic Press, San Diego, 2002.

O´Keefe1978:   M. O´Keefe, P. Buseck, S. Iijima, Nature 274 (1978) 322–324.

Paglia2005:   G. Paglia, A.L. Rohl, C.E. Buckley, J.D. Gale, Physical Review B 71 (2005) 224115-1 – 224115-16.

Parker1990:   J.C. Parker, R.W. Siegel, Applied Physical Letters 57 (1990) 943–945.

Pauling1925:   L. Pauling, S.B. Hendricks, Journal of the American Chemical Society 47 (1925) 781–790.

Petrov1992:   I. Petrov, F. Adibi, J.E. Greene, W.D. Sproul, W.D. Munz, Journal of Vacuum Science & Technology A (10) (1992) 3283–3287.

Petrov1997:   I. Petrov, P. Losbichler, D. Bergstrom, J.E. Greene, W.–D. Münz, T. Hurkmans, T. Trinh, Thin Solid Films 302 (1997) 179–192.

Petrov2003:   I. Petrov, P.B. Barna, L. Hultman, J.E. Greene, Journal of Vacuum Science & Technology A 21 (2003) 117–128.

Pohler2014:   M. Pohler, R. Franz, J. Ramm, P. Polcik, C. Mitterer, Thin Solid Films 550 (2014) 95–104.

Ramm2007a: J. Ramm, M. Ante, H. Brändle, A. Neels, A. Dommann, M. Döbeli, Advanced Engineering Materials 9 (2007) 604–608.

Ramm2007b: J. Ramm, M. Ante, T. Bachmann, B. Widrig, H. Brändle, M. Döbeli, Surface and Coatings Technology 202 (2007) 876–883.

Risic1993:   M. Ristic, S. Popovic, S. Msic, Materials Letters 1 (6) (1993) 309−612.

Rooksby1961:   H.P. Rooksby, C.J.M. Rooymans, The Formation and Structure of Delta Alumina, Philips Research Laboratories, Eindhoven, Netherlands, 1961, pp. 235.

Rother1992:   B. Rother, J. Vetter, Plasmabeschichtungsverfahren und Hartstoffschichten, Deutscher Verlag für Grundstoffindustrie, Leipzig, 1992.

Rossi1970:   L.R. Rossi, W.G. Lawrence, Journal of the American Ceramic Society 53 (1970) 604–608.

Roy1972:   D.M. Roy and R.E. Barks, Nature, 235 (1972) 118–119.

Scheu2003:   C. Scheu, M. Gao, K. van Benthem, S. Tsukimoto, S. Schmidt, W. Sigle, G. Richter, J. Thomas, Journal of Microscopy 210 (2003) 16−24.

Schulze2000:   M. Schulze, Ph.D. Thesis, Otto–von–Guericke Universität, Magdeburg, 2000.

Sitte1985:   W. Sitte in: Reactivity of Solids, P. Barret, L.–C. Dufour, eds., Elsevier, Dijon, 1985, pp. 451–456.

Smith1995:   D.L. Smith in: Thin–Film Deposition: Principles & Practice, McGraw–Hill Inc., New York, 1995.

Smith2005:   E. Smith, G. Dent, Modern Raman Spectroscopy – A Practical Approach, Wiley & Sons Ltd, Chichester, 2005.

Sproul1991:   W.D. Sproul, Surface and Coatings Technology 49 (1991) 284–289.

Sproul2005:   W.D. Sproul, D.J. Christie, D.C. Carter, Thin Solid Films 491 (2005) 1–17.

Steffens1996:   H.–D. Steffens, J. Wilden, Moderne Beschichtungsverfahren, DGM Informationsgesellschaft, Oberursel, 1996.

Strecker1993:   A. Strecker, U. Salzberger, J. Mayer, Praktische Metallographie 30 (1993) 482–495.

Tesmer1995:   J.R. Tesmer, M. Nastasi, Handbook of Modern Ion Beam Materials Analysis, Materials Research Society, Pittsburgh 1995, pp. 83–138.

Thomas1979:   G. Thomas, M.J. Goringe, Transmission Electron Microscopy of Materials, John Wiley & Sons, New York, 1979.

Thornton1974:   J.A. Thornton, Journal of Vacuum Science & Technology 11 (1974) 666–670.

Thornton1977:   J.A. Thornton, Annual Review of Materials Science 7 (1977) 239−260.

Verhoeven1986:   J.D. Verhoeven, Scanning Electron Microscopy, Material Characterization, Vol 10, ASM International (1986)490–515.

Vuorinen1992:   S. Vuorinen, L. Karlsson, Thin Solid Films 214 (1992) 132–143.

Weber2000:   W.H. Weber, R. Merlin, Raman Scattering in Materials Science, Springer–Verlag, Berlin, 2000.

Williams1996a: D.B. Williams, C.B. Carter, Transmission Electron Microscopy: Vol.1 Basics, Springer Science + Business Media Inc., New York, 1996.

Williams1996b: D.B. Williams, C.B. Carter, Transmission Electron Microscopy: Vol.2 Diffraction, Springer Science + Business Media Inc., New York, 1996.

Williams1996c: D.B. Williams, C.B. Carter, Transmission Electron Microscopy: Vol.3 Imaging, Springer Science + Business Media Inc., New York, 1996.

Williams1996d: D.B. Williams, C.B. Carter, Transmission Electron Microscopy: Vol.4 Spectrometry, Springer Science + Business Media Inc., New York, 1996.

Williams1996:   D.B. Williams, C.B. Carter, Transmission Electron Microscopy: A Textbook for Materials Science, Plenum Press, New York, 1996.

Willmann2007:   H. Willmann, Ph.D. Thesis, Montanuniversität Leoben, 2007.

Witthaut2000:   M. Witthaut, R. Cremer, K. Reichert, D. Neuschütz, Microchimica Acta 133 (2000) 191–196.

Wriedt1985:   H.A. Wriedt in: Binary Alloy Phase Diagrams, T.B. Massalski, eds., ASM Metals Park, Ohio, 1985, pp. 185.

Wyckoff1964:   R.W.G. Wyckoff, Crystal Structures, Vol. 2, 2nd Edition, Interscience Publishers, New York, 1964, pp. 6–8.

Zhou1964:   R.–S. Zhou, R.L Snyder, Acta Crystallographica B 47 (1991) 617−630.

Zywitzki1997:   O. Zywitzki, G. Hoetzsch, Surface and Coatings Technology 94−95 (1997) 303–308.

8. Publications

8.1 List of included publications

I.   Thermal stability of sputtered Al_2O_3 coatings

V. Edlmayr, M. Moser, C. Walter, C. Mitterer

Surface and Coatings Technology 204 (2010) 1576–1581.

II.   Effects of thermal annealing on the microstructure of sputtered Al_2O_3 coatings

V. Edlmayr, T.P. Harzer, R. Hoffmann, D. Kiener, C. Scheu, C. Mitterer

Journal of Vacuum Science and Technology, A 29 (4) (2011) 041506.

III.   Microstructure and thermal stability of corundum-type $(Al_{0.5}Cr_{0.5})_2O_3$ solid solution coatings grown by cathodic arc evaporation

V. Edlmayr, M. Pohler, I. Letofsky-Papst, C. Mitterer

Thin Solid Films 534 (2013) 373–379.

8.2 My contribution to appended publications

Publication I

Within this publication, my contribution was to design and perform the deposition process in an industrial scale sputter deposition plant. I deposited different substrates and in order to get powder specimen for DSC analysis I planned and optimized the process of dissolving an iron foil substrate. Several annealing treatments

as well as the Raman, DSC and XRD measurements were carried out by myself. I conducted all of the experiments by myself except for the SEM images, which were taken by Gerhard Hawranek and the ERDA measurements which were done at the Forschungszentrum Rossendorf. Concerning the analysis and interpretation part, all evaluation was done by myself except for the DSC interpretation, where Dr. Martin Moser was involved. The manuscript was prepared by myself.

Publication II

Also for this paper, I designed, optimized and performed the deposition process. Similar to the first publication, I performed and evaluated the XRD analysis and the annealing treatments. The preparation of several TEM samples was carried out by myself. (HR)TEM analysis was performed by Dr. Christina Scheu and is included in this paper with her support. I had the main responsibility of preparation and writing the paper.

Publication III

My contribution to this manuscript was to develop the concept the manuscript, to prepare powder samples of the coatings deposited on an industrial scale arc evaporation furnace. The coatings were produced by Markus Pohler. I conducted several Raman and XRD measurements, the heat treatments and the thermal analysis by myself. The TEM analyses were done by Dr. Ilse Letofsky-Papst wherein I mainly was responsible for the planning and interpretation. I investigated the processed data and prepared the major part of the paper by myself.

Summary

The proportion of my contribution in percent is summarized in the table below.

	Conception and planning[1]	Experiments	Analysis and interpretation	Manuscript preparation[1]
Publication I	100%	95%	95%	100%
Publication II	100%	85%	80%	95%
Publication III	100%	65%	90%	100%

[1] Supervision is not included!

8.3 Publications related to this thesis

IV.   Deposition of Ti–Al–N coatings by thermal CVD

J. Wagner, V. Edlmayr, M. Penoy, C. Michotte, C. Mitterer , M. Kathrein

International Journal of Refractory Metals & Hard Materials 26 (2008) 563–568.

V.   The effect of temperature and strain rate on the periodic cracking of amorphous Al_xO_y films on Cu

A.A. Taylor, V. Edlmayr, M.J. Cordill, G. Dehm

Surface and Coatings Technology 206 (2011) 1855-1859.

VI.   The effect of film thickness variations in periodic cracking: Analysis and experiments

A.A. Taylor, V. Edlmayr, M.J. Cordill, G. Dehm

Surface and Coatings Technology 206 (2011) 1830-1836.

9. Publication I

Publication I

Thermal stability of sputtered Al$_2$O$_3$ coatings

V. Edlmayr, M. Moser, C. Walter, C. Mitterer

Department Physical Metallurgy and Materials Testing, Montanuniversität Leoben,

8700 Leoben, Austria

Thermal stability of sputtered Al$_2$O$_3$ coatings

V. Edlmayr, M. Moser, C. Walter, C. Mitterer

Department Physical Metallurgy and Materials Testing, Montanuniversität Leoben,
8700 Leoben, Austria

Abstract

Al$_2$O$_3$ has a high potential as a hard compound for wear and corrosion protection because of its chemical inertness, high corrosion resistance and hardness. This work focuses on the influence of ion bombardment on the thermal stability of sputtered Al$_2$O$_3$ films. An industrial scale sputter system equipped with bipolar pulsed magnetrons was used to grow coatings at 640 °C in an argon-/oxygen atmosphere under different ion bombardment conditions. To evaluate the thermal stability, heat treatments were done in vacuum combined with differential scanning calorimetry. The crystal structure was examined by X-ray diffraction and nanoindentation was used to determine coating hardness.

The structure of the coatings grown on silicon substrates is either predominantly X-ray amorphous for low ion bombardment conditions or γ–Al$_2$O$_3$ structured for enhanced ion bombardment. For iron substrates, the formation of γ–Al$_2$O$_3$ is fostered. Two different transformation sequences were found, both ending in the formation of the thermodynamically stable α–Al$_2$O$_3$. While the γ to α–transformation on coatings deposited on iron foil occurs via the transition phase δ–Al$_2$O$_3$, coatings deposited on silicon transform directly into α–Al$_2$O$_3$. The amorphous coatings transform at lower temperatures than the coatings with γ–Al$_2$O$_3$ structure in the as deposited state. Hardness values of 10 GPa for the amorphous coating, 14 GPa for γ–Al$_2$O$_3$ and 22 GPa for α–Al$_2$O$_3$ were measured.

Introduction

Crystalline Al_2O_3 performs well as a hard compound in wear and corrosion protection, because of its excellent properties such as chemical inertness, corrosion resistance and high hardness. Hence, it is a state-of-the-art protective coating material for cemented carbide cutting tools. Al_2O_3 coatings improve the productivity of machining operations by increasing the tool life and cutting speed due to their excellent wear protection, high hot hardness and stability at elevated temperatures [1]. For about three decades, Al_2O_3 coatings have been produced using chemical vapour deposition (CVD) [2]. Using this technique, the choice of substrates is limited because of the high deposition temperature of at least 1000 °C which is required for formation of the stable $\alpha-Al_2O_3$. This drawback can be minimized by using physical vapour deposition (PVD) operating at lower temperatures. Additionally, PVD techniques offer the advantage to introduce compressive stresses in the coatings which leads to enhanced fatigue and thermal shock resistance [3]. In comparison to CVD, PVD coatings have no chlorine impurities, resulting from $AlCl_3$ precursors, and edge blunting can be avoided, which keeps sharp cutting edges of the tools [4].

Alumina modifications exist as the thermodynamically stable $\alpha-Al_2O_3$ phase (corundum-type structure) and as metastable modifications such as γ, δ, η, χ, θ and κ [5]. The alumina phases commonly used for coating applications deposited via PVD processes are $\alpha-Al_2O_3$ and $\gamma-Al_2O_3$ [3,6]. At low deposition temperatures, alumina coatings are reported to be X-ray amorphous [7,8]. $\gamma-Al_2O_3$ has been deposited using CVD at temperatures of approximately 800 °C [9], while only temperatures between 350 and 550 °C [3,6,10] are required in PVD processes. The deposition temperatures for the desired stable $\alpha-Al_2O_3$ coatings have been reported as 1000 °C for CVD and

59

700 °C for PVD [11-13]. Hence, depositing α–Al_2O_3 on steel substrates is presently not straightforward, due to the high deposition temperatures needed for formation. Further, γ–Al_2O_3 is metastable and at the high temperatures during machining it may irreversibly transform into the thermodynamically stable α–Al_2O_3 phase. This transformation is associated with a cell volume decrease of approximately 8 % and can lead to cracking and failure of the coating [5].

To elucidate the potential of metastable alumina modifications for machining applications, this work focuses on the influence of ion bombardment on phase formation and on the thermal stability of sputtered alumina films. Predominantly X-ray amorphous as well as γ–Al_2O_3 containing alumina coatings have been deposited by varying the ion bombardment conditions and their thermal stability in terms of crystal structure, morphology and mechanical properties was investigated.

Experimental Details

2.1 Coating Deposition

Alumina films were deposited in a commercial CemeCon CC800/9MLT system by reactive magnetron sputtering. The system is equipped with four unbalanced magnetrons. The power at each magnetron was bipolar pulsed and voltage controlled at -340 V with a pulsing frequency of 50 kHz using Advanced Energy Pinnacle dc power supplies (20 kW output) with Advanced Energy Astral pulsing units. The aluminium targets had a size of 500×88×10 mm. Argon was used as working gas with a constant flow rate of 400 sccm and oxygen as reactive gas. The oxygen flow was in the rage of 50-80 sccm controlled by the target voltage. During deposition, the total pressure was 0.87 Pa. Silicon (100) and iron foil were used as substrates. The substrate temperature was approximately 640 °C. For cleaning purposes, the samples as well as the iron foil were heated to 600 °C and Ar ion etched (0.4 Pa) for 13 min prior to deposition. A

pulsed dc bias voltage was applied to the substrate carrousel with a frequency of 350 kHz and a pulse reverse time of 500 ns. The ion bombardment was varied by substrate bias, where the ion current was enhanced by the CemeCon booster technology [14]. During deposition, the sample carrousel was rotating and a deposition time of 3.3 hours was chosen to obtain a film thickness in the range of $3-4$ μm.

2.2 Heat Treatment

After deposition, the coatings were annealed in a vacuum furnace with a heating rate of 5 K/min and a pressure of 10^{-2} Pa. Annealing treatments were performed for 3 and 12 h at a constant temperature of 700, 800, and 1000 °C.

2.3 Coating Analysis

The iron foil substrates were used to prepare coating powder specimen for differential scanning calorimetry (DSC). After coating deposition, the iron foil was chemically dissolved in a $4:1$ solution of distilled water and 66% nitric acid at 75 °C. The resulting coating flakes were dried and milled to a fine powder. All other analyses were performed on the coatings deposited on silicon, unless mentioned otherwise.

Elastic recoil detection analysis (ERDA) was used in order to determine the chemical composition including the absolute atomic concentration of aluminum, oxygen and light elements (such as hydrogen) as well as impurities, see Ref. [15] for details.

A Zeiss EVO 50 scanning electron microscope (SEM) equipped with an energy-dispersive X-ray analyzer (EDX, Oxford Instruments INCA) was employed to study the coating morphology by examining fracture cross-sections.

X-ray diffraction (XRD) analysis was done using an XRD diffractometer Siemens D500 in the Bragg-Brentano *(θ–2θ)* configuration with CuKα (λ=0.154056 nm) radiation. Additionally, a D8 Advance diffractometer from Bruker-AXS with parallel

beam optics (Goebel mirror) and an energy-dispersive Sol-X detector was used to identify the crystal structure of the coatings.

Complementary to the XRD experiments, also Raman spectroscopy was performed with a HORIBA Jobin Yvon Labram-HR800 with a laser-wavelength of 632 nm (He–Ne–Laser) for sample excitation and a CCD-camera with 100× objective for signal detection.

Hardness was assessed by nanoindentation using a UMIS ultra-micro indentation system with a Berkovich indenter calibrated in fused silica according to Oliver and Pharr [16]. The loads were stepwise increased from 1 to 50 mN for each measurement, keeping the maximum penetration depth below 10% of the film thickness.

For detailed investigations of microstructural changes with temperature and time, DSC was used in combination with XRD. For DSC measurements, 8 mg of the above mentioned powder specimen was transferred to a platinum crucible with alumina inserts. The measurements were performed using a Netzsch-STA 409C thermal analysis instrument with a heating rate of 20 K/min under continuous argon flow up to 1400 °C [17]. The cooling rate was set to 20 K/min. In order to remove volatile contaminations, such as water or hydrocarbons, an isothermal step at a temperature of 150 °C was used.

Results and Discussion

In this work, two kinds of Al_2O_3 films are compared, which will be referred to as sample A and B in the following. They were deposited under identical conditions, but sample B was subjected to enhanced ion bombardment due to the applied -40 V bias voltage in comparison to sample A, which was grown at floating potential. This results in sample A showing a film thickness of 3 μm and essentially X-ray amorphous

structure in the as deposited state, while sample B shows a thickness of 4 µm and $\gamma-Al_2O_3$ phase.

All coatings were well adherent to the silicon (100) substrate as well as iron foil. The X-ray amorphous films show a matt surface while the crystalline films exhibit a shiny appearance with different interference coloration depending on the film thickness ranging from yellow to violet.

3.1 Composition

Chemical composition of the films on Si substrates was determined by ERDA, yielding 39.7 at.% aluminum, 58.6 at.% oxygen and minor impurities such as 1.2 at.% hydrogen, 0.3 at.% nitrogen and 0.1 at.% carbon. Hence, the atomic ratio Al/O is with a value of 0.68 close to the stoichiometric composition of Al_2O_3 (Al/O = 0.66). EDX measurements on fracture cross-sections confirmed that no silicon from the substrate diffused into the film, neither during deposition nor during the annealing processes.

3.2 Phase Evolution

Fig. 1 shows the influence of annealing time and temperature on sample A. The as deposited film on a silicon substrate is basically X-ray amorphous with only a very weak and broad feature at $2\theta \sim 46°$ as shown in the XRD pattern on the bottom of Fig. 1. After an annealing treatment of 3 h at 700 °C, no significant changes in structure can be seen. However, at temperatures above 800 °C unambiguous formation of $\gamma-Al_2O_3$ was detected, but no further changes in structure were observed after annealing at 1000 °C for 12 h. No evidence for $\alpha-Al_2O_3$ formation was detected.
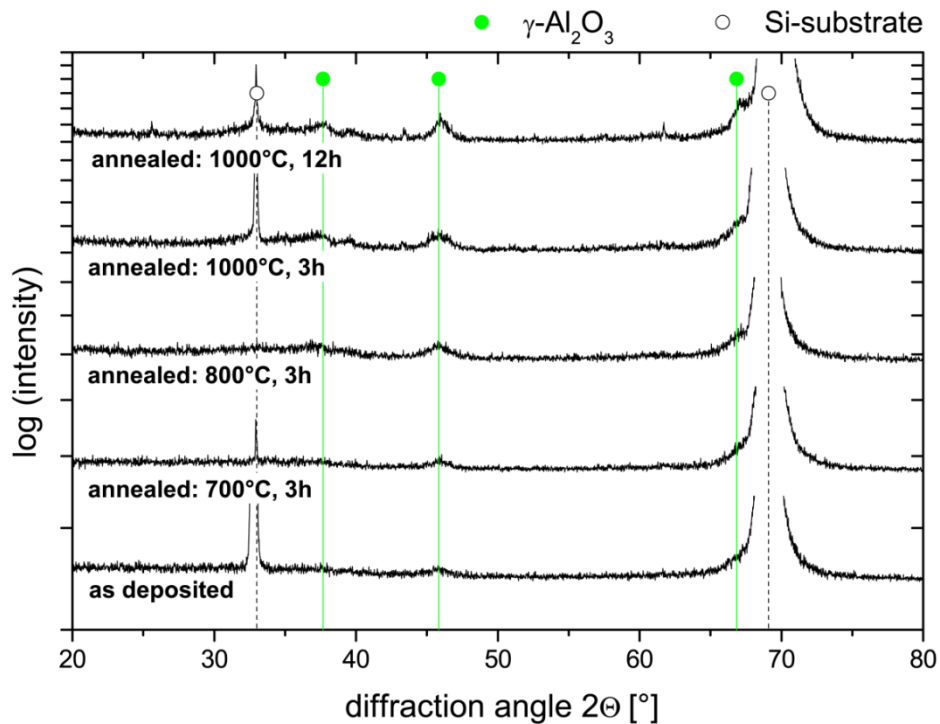
Figure 1:   XRD patterns of sample A in the as deposited state and after different annealing treatments.

In comparison, sample B has clear indications for crystalline γ–Al_2O_3 in the as deposited state, which is illustrated in Fig. 2. This is in agreement with literature, where a strong dependence of the structure evolution on the ion bombardment during film growth is reported [14,18,19,20]; however, an additional amorphous phase can not be excluded. In contrast to sample A, first signs of a phase transformation to α–Al_2O_3 were detected after annealing for 3 h at 1000 °C. A considerable change in the diffraction pattern was observed after a heat treatment at 1000 °C for 12 h. There, the intensity of the γ–Al_2O_3 peak at $2\theta \sim 46°$ is reduced and the film consists pre-dominantly of α–Al_2O_3.
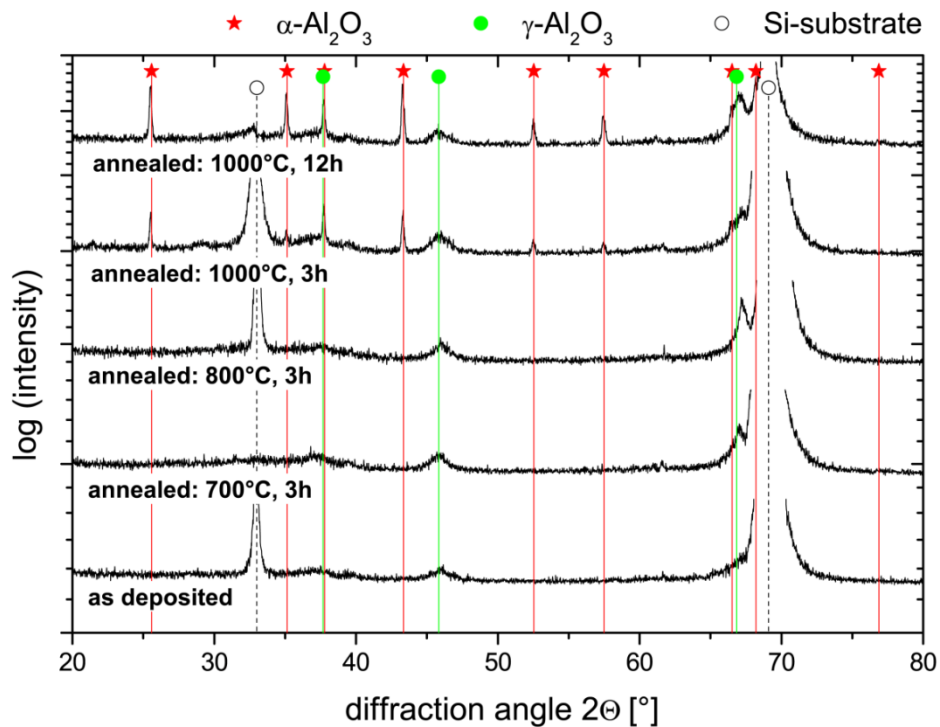
Figure 2:   XRD patterns of sample B in the as deposited state and after different annealing treatments.

To support the XRD results, Raman spectroscopy was conducted. Fig. 3 shows the Raman spectra of the uncoated silicon substrate, an α–Al_2O_3 reference as well as spectra from sample A and sample B in the as deposited state and after annealing for 12 h at 1000 °C. According to Mortensen *et al.*, γ–Al_2O_3 is not Raman active [21]; thus peaks are only visible for sample B after annealing. These peaks match the α–Al_2O_3 reference and confirm the presence of α–Al_2O_3 [21,22].
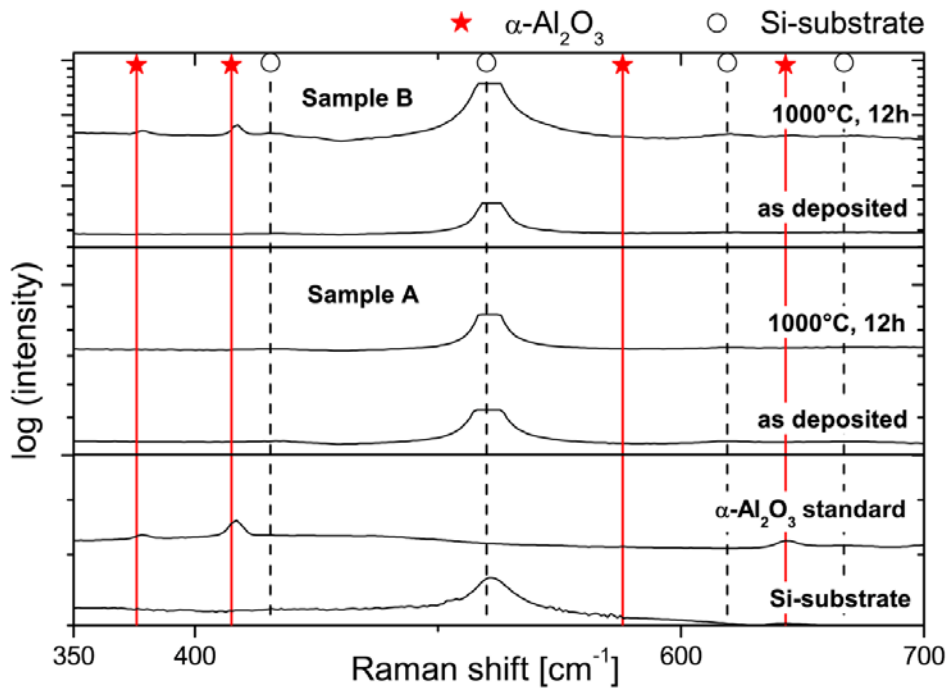
Figure 3:   Raman spectra of sample A and B in the as deposited state and after annealing at 1000 °C for 12 h. For comparison, spectra of an $\alpha-Al_2O_3$ reference as well as the uncoated Si substrate are presented.

3.3 Hardness

In the as deposited state the X-ray amorphous sample A exhibits a hardness of 10±0.4 GPa, while the annealed sample (1000 °C, 12 h) with $\gamma-Al_2O_3$ phase reaches a value of 14±0.6 GPa. The as deposited sample B with the $\gamma-Al_2O_3$ phase already in the as deposited state shows a hardness of 16±0.6 GPa, whereas values of 22±1.4 GPa were measured on the $\alpha-Al_2O_3$ structured sample B after annealing at 1000 °C for 12 h. These data are in good agreement with recent literature [11,13,18,23,24].

3.4 Morphology

The influence of a heat treatment up to 1000 °C for 12 h on the film morphology was investigated on SEM fracture cross-sections presented in Fig. 4. The in the as deposited state predominantly X-ray amorphous sample A shows a columnar growth structure and high surface roughness (Fig. 4a). During annealing thermal cracks as marked by the white arrows in Fig. 4b were formed. These cracks are also seen as a crack network on the coating surface, similar to CVD [25] and PVD [26] alumina coatings. In comparison, the more crystalline sample B exhibits a more fine-grained morphology prior to annealing (Fig. 4c), comparable to the structure reported by Zywitzki *et al.* [18]. After annealing thermal cracks can be seen for sample B (Fig. 4d), which are due to the mismatch between the thermal expansion of film and substrate and the phase transformation from $\gamma-Al_2O_3$ to $\alpha-Al_2O_3$.
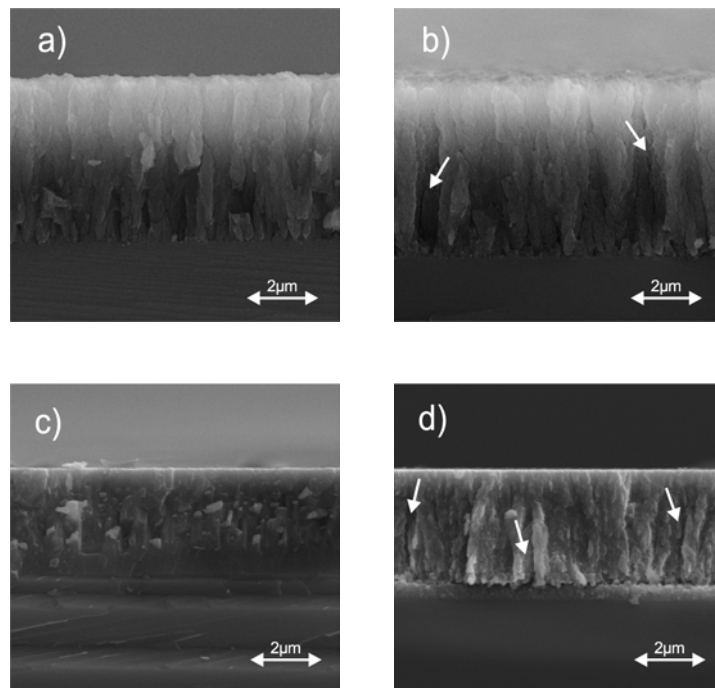
Figure 4:   SEM fracture cross-sections of a) sample A in as deposited state, b) sample A after annealing at 1000 °C for 12 h, c) sample B as deposited, d) sample B after annealing at 1000 °C for 12 h. Examples for cracks formed in the annealed samples are marked by white arrows.

3.5 Thermal Analysis by DSC

The microstructural changes during annealing were investigated in detail by dynamic DSC measurements of coating powder samples in argon up to 1400 °C. In comparison to the annealing treatment performed for the coatings deposited on silicon the DSC analysis has the advantage to be an in-situ measurement, which enables a continuous measurement of transformation processes during temperature increase. However, the necessarily different kinetics for the DSC measurement differs from the annealing treatment and this does not allow for a direct comparison of results obtained from the two methods.

3.5.1 Powder Specimen A

In order to follow the structural evolution upon annealing, XRD patterns were recorded on powder samples heated in the DSC up to 900, 1100 and 1200 °C. Fig. 5 shows the respective diffractograms obtained in the as deposited state and after annealing in the DSC. Due to the variation of substrate material (i.e. the dissolved iron foil instead of silicon), the XRD pattern of the powder specimen of sample A differs slightly from the coating sample A. While sample A deposited on silicon shows essentially X-ray amorphous structure (see Fig. 1), an amorphous background as well as small indications for the formation of the $\gamma-Al_2O_3$ phase were detected for the powder specimen. The appearance of these peaks could be an effect of more randomly oriented grains of the powder sample. According to Ref. [27], iron increases the transformation velocity of alumina. No evidence for iron or iron oxides could be detected by XRD, but since the tested powder have been grown on iron foil, it might be assumed that during deposition at 640 °C for about 3 h iron-stimulated transformation from amorphous to $\gamma-Al_2O_3$ had already started. At 900 °C, the amorphous background is still present, while the peaks of the $\gamma-Al_2O_3$ phase are gaining intensity. Additionally, peaks of $\delta-Al_2O_3$ are present. This $\delta-Al_2O_3$ phase was not detected within the films grown on silicon. Further heat treatment up to 1100 °C

confirms the presence of γ–Al_2O_3 and δ–Al_2O_3, with a shift of the peak at $2\theta \sim 46°$ to lower angles, approaching the δ–Al_2O_3 position. It can not be excluded that besides δ–Al_2O_3 also θ–Al_2O_3 is present [19,28], since the JCPDS standard peak positions for θ–Al_2O_3 are very similar to those of δ–Al_2O_3 [26,29]. δ–Al_2O_3 exhibits additional diffraction peaks compared to θ–Al_2O_3, however, all peak positions of θ–Al_2O_3 overlap with those of δ–Al_2O_3. After annealing at 1100 °C clear indications for α–Al_2O_3 appear. After the heat treatment at 1200 °C, only those peaks characteristic for the thermodynamically stable α–Al_2O_3 are present.
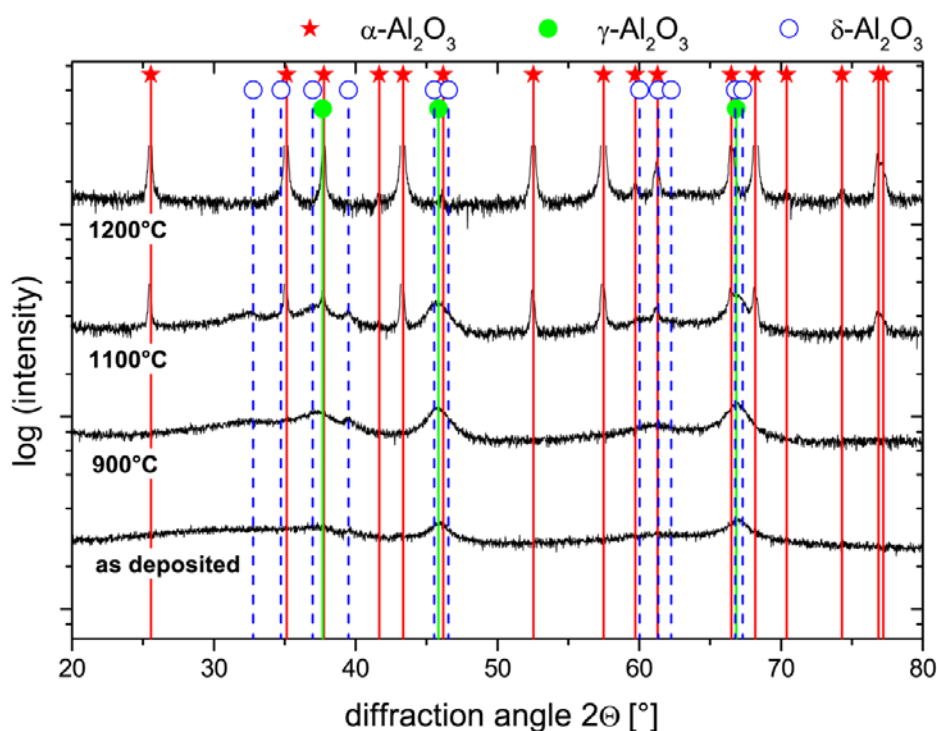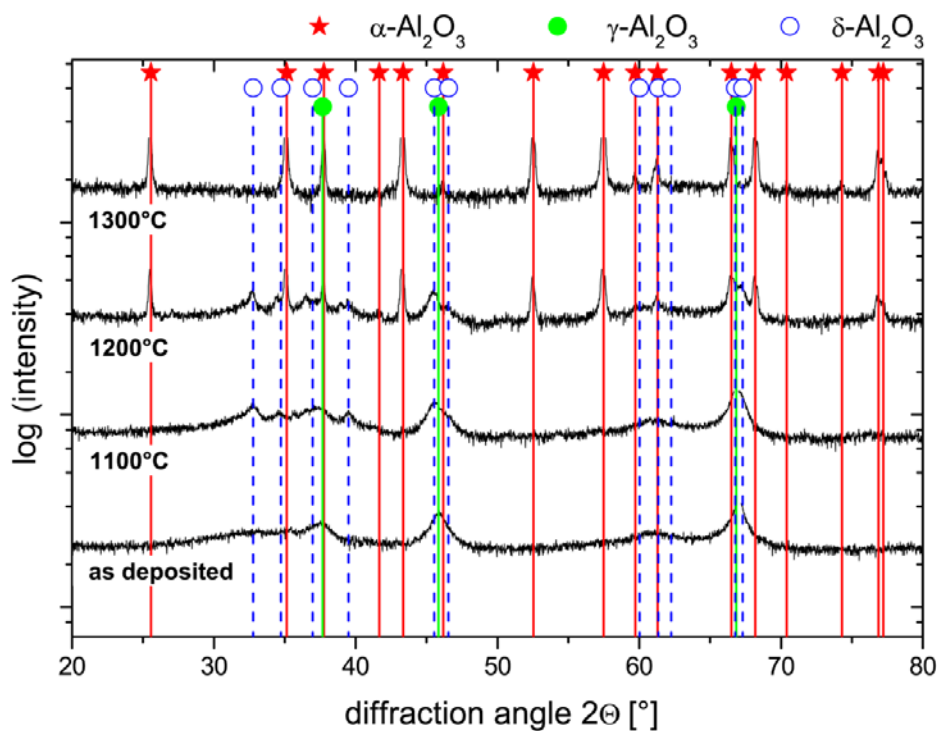

Figure 5:   XRD patterns of powder sample A in the as deposited state and after annealing in the DSC up to the given temperatures.

3.5.2 Powder Specimen B

The results of XRD measurements of the powder sample B prior to and after heat treatment are illustrated in Fig. 6. The XRD pattern of the as deposited iron grown powder sample is comparable to the silicon grown film shown in Fig. 2, indicating the existence of $\gamma-Al_2O_3$, only the $\gamma-Al_2O_3$ phase is much more pronounced in case of the powder specimen. After annealing at 1100 °C, a phase composition of $\gamma-Al_2O_3$ and $\delta-Al_2O_3$ was observed. Further annealing at 1200 °C results in a mixture of $\gamma-Al_2O_3$, $\delta-Al_2O_3$ and $\alpha-Al_2O_3$. $\gamma-Al_2O_3$ and $\delta-Al_2O_3$ fully transform to $\alpha-Al_2O_3$ after annealing at 1300 °C.

Figure 6: XRD patterns of powder sample B in the as deposited state and after annealing in the DSC up to the given temperatures.

Fig. 7 compares the DSC signals obtained during heating of powder samples A and B up to 1400 °C. Sample A shows a first exothermic peak between 800 and 900 °C, which is – in accordance with the results of the XRD investigations – attributed to the crystallization of $\gamma-Al_2O_3$, and a second exothermic peak at ~1150 °C indicative for transformation into the thermodynamically stable $\alpha-Al_2O_3$ phase. This temperature range agrees well with literature values for the respective phase transformation temperatures [30]; however, other studies have found temperature values from 975 °C to 1300 °C [26,31]. A slow rise of the heat flow between the two transformation peaks can be observed. This slow rise might be explained on the one hand by ongoing nucleation, growth and recovery mechanisms and on the other hand by formation of the so-called transition phases of alumina, such as $\delta-Al_2O_3$ and $\theta-Al_2O_3$ [28,32-34] as shown in Fig. 5.
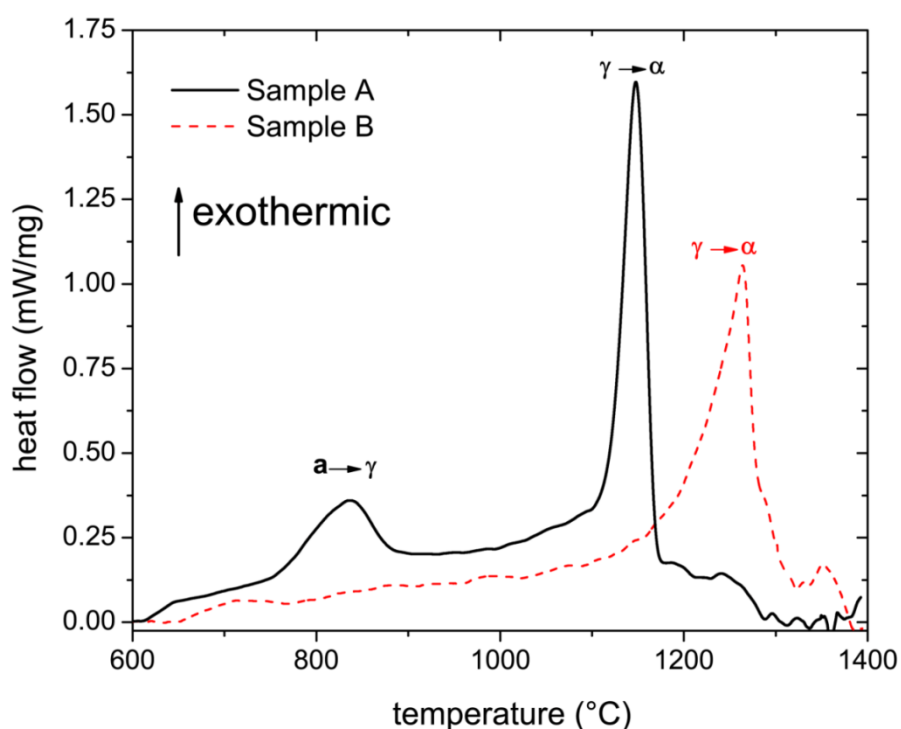
Figure 7:   Heat flow of dynamic DSC scans taken of powders of sample A and sample B; heating rate 20 K/min.

For the powder sample B, which consists predominantly of γ–Al_2O_3 prior to annealing, the above mentioned increase in heat flow is also observed and followed by a sharp exothermic peak indicative for the transformation to α–Al_2O_3. Due to the higher activation energy necessary for the phase transformation, α–Al_2O_3 transformation peaks are generally sharper and more intense than the γ–Al_2O_3 transformation peak [33,35]. The α–Al_2O_3 transformation peak of powder specimen B is less sharp than that of powder specimen A and it is delayed to higher temperatures (from 1150 to 1260 °C, see Fig. 7). Wen *et al.* reported that the peak position of the transformation to α–Al_2O_3 depends on the evolution of its crystallite size during heating. The earlier these crystallites reach a critical size, the lower is the transformation temperature needed for nucleation of α–Al_2O_3. Therefore, the peak intensity can be correlated with the amount of crystallites of alumina transition phases simultaneously available for α–Al_2O_3 nucleation [32,33,35,36]. As shown in Fig. 5 for powder specimen A, the first indications of δ–Al_2O_3 are obtained after annealing at 900 °C, while sample B needed 1100 °C to form δ–Al_2O_3 (see Fig. 6). This is in good agreement with the onset temperature needed for transformation into the thermodynamically stable α–Al_2O_3 phase of powder specimen A and powder specimen B, with a higher onset temperature for powder specimen B.

This is also supported by the higher range of order of the Al cations in the δ–Al_2O_3 phase compared to the γ–Al_2O_3 [37]. Thus, a higher thermal stability of the δ–Al_2O_3 phase can be expected.

Conclusions

From this initial study on the thermal stability of sputtered alumina films, the following conclusions can be drawn:

The structure of Al_2O_3 coatings on silicon substrates can be either predominantly X-ray amorphous for low ion bombardment or $\gamma-Al_2O_3$ structured for enhanced ion bombardment. Powder specimens prepared from both coating types grown on iron foil, which has been chemically dissolved after deposition, exhibit $\gamma-Al_2O_3$, which is in the case of the low ion bombardment accompanied by an amorphous phase. The $\gamma-Al_2O_3$ peaks observed for enhanced ion bombardment are more pronounced, indicating suppression of amorphous growth by energetic ion bombardment.

Annealing results in the irreversible formation of $\alpha-Al_2O_3$; however, the transformation sequence is determined by the structure of the as deposited coating. It has been shown that there is the possibility to transform directly into $\alpha-Al_2O_3$ or via an intermediate transition phase, like $\delta-Al_2O_3$, depending on the substrate material. While sample A remains $\gamma-Al_2O_3$ structured up to 1000 °C for an annealing time of 12 h, sample B already contains $\alpha-Al_2O_3$ phase after the same annealing treatment. Additionally, the combination of DSC and XRD measurements shows that within the powder specimen $\delta-Al_2O_3$ was formed en route from $\gamma-Al_2O_3$ to the thermodynamically stable $\alpha-Al_2O_3$ phase, but this was not observed for coatings on silicon.

The obtained results are of importance for a fundamental understanding of the thermal stability of alumina phases formed in sputtered coatings and might be a pre-requisite for their application in high performance machining.

Acknowledgement

References

[1]   M. Kathrein, W. Schintlmeister, W. Wallgram, U. Schleinkofer, Surf. Coat. Technol. 163 −164 (2003) 181−188.

[2]   A. Larsson, M. Halvarsson, S. Ruppi, Surf. Coat. Technol. 111 (1999) 191−189.

[3]   A. Schütze, D.T. Quinto, Surf. Coat. Technol 162 (2003) 174−182.

[4]   K. Bobzin, E. Lugscheider, M. Maes, C. Pinero, Thin Solid Films 494 (2006) 255−262.

[5]   S. Vuorinen, L. Karlsson, Thin Solid Films 214 (1992) 132−143.

[6]   R. Cremer, M. Witthaut, D. Neuschütz, G. Erkens, T. Leyendecker, M. Feldhege, Surf. Coat. Technol. 120 (1999) 213−218.

[7]   J.A. Thornton, J. Am. Ceram. Soc. Bull. 56 (5) (1977) 504−508.

[8]   T.C. Chou, D. Adamson, J. Mardinly, T.G. Nieh, Thin Solid Films 205 (1991) 131−139.

[9]   S. Ruppi, A. Larsson, Thin Solid Films 388 (1−2) (2001) 50−61.

[10]   A. Astrand, T.I. Selinder, F. Fietzke, H. Klostermann, Surf. Coat. Technol. 188−189 (2004) 186−192.

[11]   O. Zywitzki, G. Hoetzsch, Surf. Coat. Technol. 94−95 (1997) 303−308.

[12]   F. Fietzke, G. Goedicke, W. Hempel, Surf. Coat. Techol. 86−87 (1996) 657−663.

[13]   T. Kohara, H. Tamagaki, Y. Ikari, H. Fujii, Surf. Coat. Technol. 185 (2004) 166−171.

[14]   K.-D. Bouzakis, G. Skordaris, N. Michailidis, I. Mirisidis, G. Erkens, R. Cremer, Surf. Coat. Technol. 202 (2007) 826−830.

[15]   W. Bohne, J. Röhrich, G. Röschert, Nucl. Instrum. Methods. Phys. Res. B 139 (1998) 219−224.

[16]   W.C. Oliver, G.M. Pharr, J. Mater. Res. 7 (1992) 1564−1583.

[17]   P.H. Mayrhofer, H. Willmann, C. Mitterer, Surf. Coat. Technol. 146−147 (2001) 222−228.

[18] O. Zywitzki, G. Hoetzsch, F. Fietzke, K. Goedicke, Surf. Coat. Technol. 82 (1996) 169−175.

[19] K.J.D. MacKenzie, J. Temuujin, M.E. Smith, P. Angerer, Y. Kameshima, Thermochim. Acta 359 (2000) 87−94.

[20] E.J.L. Rosén, Theoretical and Experimental Studies Related to the Compositional and Microstructural Evolutionof Alumina Thin Films, Ph.D. Thesis, University of Aachen, 2004.

[21] A. Mortensen, D.H. Christensen, O.F. Nielsen, E. Pedersen, J. Raman Spectrosc. 22 (1991) 47−49.

[22] A. Misra, H.D. Bist, M.S. Navati, R.K. Thareja, J. Narayan, Mater. Sci. Eng. B79 (2001) 49−54.

[23] O. Zywitzki, G. Hoetzsch, Surf. Coat. Technol. 86-87 (1996) 640−647.

[24] J.M. Andersson, Controlling the Formation and Stability of Alumina Phases, Ph.D. Thesis, Linköping University, 2005.

[25] D. Hochauer, C. Mitterer, M. Penoy, C. Michotte, H.P. Martinz, M. Kathrein, Surf. Coat. Technol. 203 (2008) 350−356.

[26] D.H. Trinh, K. Back, G. Pozina, H. Blomqvist, T. Selinder, M. Collin, I. Reineck, L. Hultman, H. Höberg, Surf. Coat. Technol. 203 (2009) 1682−1688.

[27] D.R. Clarke, Phys stat. sol. 166 (1998) 183−196.

[28] A. Boumaza, L. Favaro, J. Lédion, G. Sattonnay, J.B. Brubach, P. Berthet, A.M. Huntz, P. Roy, R. Tétot, J. Solid State Chem. 182 (2009) 1171−1176.

[29] J.R. Wynnyckyj, C.G. Morris, Met. Trans. B. 16B (1985) 345−353.

[30] M. Dressler, M. Nofz, F. Malz, J. Pauli, C. Jäger, S. Reinsch, G. Scholz, J Solid State Chem. 180 (2007) 2409−2419.

[31] J. Plewa, M. Wojcik, H. Uphoff, N. Munser, H. Altenburg, J. Therm. Anal. Cal. 56 (1999) 59−66.

[32] H.L. Wen, Y.Y. Chen, F.S. Yen and C.Y. Huang, Nanostruct. Mater. 11 (1999) 89−101.

[33] H.-L. Wen, F.-S. Yen, J. Crystal Growth 208 (2000) 696−708.

[34] C.J.-P. Steiner, D.P.H. Hasselman, R.M. Spriggs, J. Am. Ceram. Soc. 54 (1997) 412−413.

[35] F.S. Yen, H.L. Wen, Y.T. Hsu, J. Crystal Growth 233 (2001) 761−773.

[36] Q.Y. Zhang, W.J. Zhao, P.S. Wang, L. Wang, J.J. Xu, P.K. Chu, Nucl. Instr. Meth. Phys. Res. B 206 (2003) 357−361.

[37] I. Levin, L.A. Bendersky, D.G. Brandon, M. Rühle, Acta. Mater. 45 (1997) 3659−3669.

10. Publication II

Publication II

Effects of thermal annealing on the microstructure of sputtered Al$_2$O$_3$ coatings

V. Edlmayr[a], T.P. Harzer[b], R. Hoffmann[b], D. Kiener[b], C. Scheu[b], C. Mitterer[a]

[a]Department of Physical Metallurgy and Materials Testing, Montanuniversität Leoben,

8700 Leoben, Austria

[b]Department of Chemistry, Ludwig-Maximilians-University of Munich,

81377 Munich, Germany

Effects of thermal annealing on the microstructure

of sputtered Al$_2$O$_3$ coatings

V. Edlmayr[a], T.P. Harzer[b], R. Hoffmann[b], D. Kiener[b], C. Scheu[b], C. Mitterer[a]

[a]Department of Physical Metallurgy and Materials Testing, Montanuniversität Leoben,

8700 Leoben, Austria

[b]Department of Chemistry, Ludwig-Maximilians-University of Munich,

81377 Munich, Germany

Abstract

The morphology and microstructure of Al$_2$O$_3$ thin films deposited by pulsed direct current magnetron sputtering were studied in the as-grown state and after vacuum annealing at 1000 °C for 12 h using transmission electron microscopy. For the coating deposited under low ion bombardment conditions, the film consists of small $\gamma-$ and/or $\delta-$Al$_2$O$_3$ grains embedded in an amorphous matrix. The grain size at the region close to the interface to the substrate was much larger than that of the remaining layer. Growth of the $\gamma-$Al$_2$O$_3$ phase is promoted during annealing but no transformation to $\alpha-$Al$_2$O$_3$ was detected. For high-energetic growth conditions, clear evidence for $\gamma-$Al$_2$O$_3$ formation was found in the upper part of the coating with grain size much larger than for low-energetic growth, but the film was predominately

amorphous at the interface region. Annealing resulted in the transformation of γ–Al_2O_3 to α–Al_2O_3, while the mainly amorphous part crystallized to γ–Al_2O_3.

Keywords: Al_2O_3; Alumina; Sputtering; Coatings; Annealing; Thermal stability; TEM; EELS.

I. Introduction

Alumina thin films have been studied intensively in the recent years due to their outstanding properties such as chemical inertness, corrosion resistance and hardness, which make them interesting as protective coating for cutting tools.[1] In severe cutting applications such as high-speed and dry cutting, the temperature at the cutting edge can exceed 1000 °C.[2] The applied protective coating has to withstand these conditions and, thus, knowledge of its thermal stability is of vital importance. In general, alumina exhibits several metastable allotropic modifications such as γ, δ, η, θ, κ and, in addition, the thermodynamically stable α–Al_2O_3 phase.[3] α–Al_2O_3 belongs to the trigonal crystal system and has a rhombohedral lattice (space group $R\bar{3}c$). The crystal structure of α–Al_2O_3 can alternatively be described as a hexagonal close-packed oxygen superlattice, where 2/3 of the octahedral interstitial positions are filled with aluminum atoms.[4-6] Contrary, the metastable γ–Al_2O_3 phase possesses a spinel structure (space group $Fd\bar{3}m$) with oxygen anions in a face-centered cubic lattice. The Al cations possess not only octahedral but also a tetrahedral coordination.[4,7,8] The also metastable so-called transition phases δ– and θ–Al_2O_3 are often observed during transformation from γ–Al_2O_3 to α–Al_2O_3. δ–Al_2O_3 is viewed as a superstructure of γ–Al_2O_3 and is of tetragonal or orthorhombic symmetry, while θ–Al_2O_3 exhibits a monoclinic symmetry.[9,10]

We recently reported that stoichiometric Al_2O_3 films grown by pulsed dc magnetron sputtering can be grown predominantly amorphous for low ion

bombardment conditions or $\gamma–Al_2O_3$ structured for enhanced ion bombardment as determined by X-ray diffraction (XRD).[11] The enhanced ion bombardment seems to promote crystalline growth. Vacuum annealing experiments showed that in the amorphous coating $\gamma–Al_2O_3$ is formed at temperatures above 700 °C, which withstands annealing at 1000 °C for 12 h without transformation, while the already in the as-deposited state $\gamma–Al_2O_3$ structured coating transforms according to XRD to $\alpha–Al_2O_3$ after the same annealing treatment. A similar transformation behavior was also recently reported by other authors.[12-14] However, a detailed microstructural characterization of the transformed phases is still missing. The previously published studies[11-14] applied mainly XRD techniques, which do not provide local information about phase morphology and topography. Therefore, within this study a combination of various transmission electron microscopy (TEM) techniques, including selected area diffraction (SAD), high-resolution TEM (HRTEM), and electron energy-loss spectroscopy (EELS) were used to investigate the microstructure in more detail. The aim was to identify the various phases and their grain sizes within as-deposited and annealed coatings, in order to gain information about nucleation sites for the transformation into $\alpha–Al_2O_3$. Furthermore, we wanted to determine the homogeneity of the coating across the film thickness, an information which is not available from $\theta–2\theta$ XRD measurements. For phase identification, we also analyzed the electron energy-loss near-edge structure (ELNES) associated with each ionization-edge in the EELS spectrum. As the ELNES is sensitive to the bonding character and the structural arrangement of neighboring atoms; for different modifications the shape of the ELNES is different[15-17], thereby providing highly localized structural information.

II. Experimental details

A. Coating deposition and heat treatment

Coatings were deposited in a CemeCon CC800/9MLT system equipped with four unbalanced magnetrons by reactive magnetron sputtering. The power at each magnetron of ~3.7 kW was bipolar pulsed at a duty cycle of 50% and voltage controlled at -340 V with a pulsing frequency of 50 kHz using Advanced Energy Pinnacle dc power supplies with Advanced Energy Astral pulsing units. The reverse voltage was set to 10% of the operating voltage. The four aluminum targets used had a size of $500 \times 88 \times 10$ mm^3. Argon was used as working gas with a constant flow rate of 400 sccm and oxygen as reactive gas. The oxygen flow was in the range of $50-80$ sccm controlled via the target voltage. During deposition, the total pressure was 0.87 Pa. Single crystalline silicon (100) substrates were heated to 600 °C and Ar ion etched at 0.4 Pa for 13 min. A pulsed etching dc voltage of 650 V was applied to the substrate carrousel with a frequency of 350 kHz and a pulse reverse time of 500 ns, which leads to a 5 times higher pulse-on than pulse-off time. The ion current was enhanced by the CemeCon booster technology[18], which is in the system used based on an additional discharge between the gas inlet as cathode and a Ti anode placed between two targets, thus reaching substrate ion currents of 1.7 A. The ion bombardment during deposition was varied by the substrate bias, i.e. floating potential in case of sample A and -40 V for sample B. The substrate temperature, as measured by the softening of steel substrates, was ~640 °C for sample A grown at floating bias and ~660 °C for sample B, where the bias voltage of -40 V caused an ion current of ~12 A. The samples showed a twofold rotation with a substrate carrousel rotation speed of 1 rpm. The minimum substrate-to-target distance was 80 mm. A time of 3.3 h was chosen to obtain a film thickness in the range of $3-4$ µm. Prior to each deposition run a 300 nm thick Al layer was deposited and the Ti anode was cleaned thoroughly and to ensure similar electrical properties of the substrate carrousel and the whole reaction chamber.

After deposition, coatings were annealed in a vacuum furnace with a heating rate of 5 K/min and a pressure of 10^{-2} Pa. Annealing treatments were performed for 12 h at a constant temperature of 1000 °C.[11] Furthermore, biaxial coating stresses were measured using a bending technique and the modified Stoney equation was used for data analysis.[19,20]

B. TEM sample preparation and characterization

Cross-sectional TEM samples were prepared from the as-deposited and annealed coating material following the procedure described by Strecker *et al.*[21] For this method, the material is first cut into strips which are then embedded in an alumina tube. Subsequently, 3$-$mm$-$diameter disks were cut, mechanically thinned and polished, followed by mechanical dimpling until the thinnest part of the disk reaches a thickness of about 25 μm. For final thinning to electron transparency, the samples were ion-milled with argon ions at 3 kV using a Gatan PIPS until perforation was obtained. In a last step, low energy ion-milling was performed at 0.9, 0.6 and 0.3 kV for 20 min each, to minimize beam damage of the sample.[22]

TEM investigations were conducted using a FEI Titan microscope, which is equipped with a post-column energy filter (GIF Tridiem from Gatan) for analytical investigations. To study the film morphology and structure of the coatings, bright-field (BF) images and SAD pattern were taken. The grain size was determined from BF and HRTEM images. EELS/ELNES measurements were performed at 300 kV in diffraction mode using a SAD aperture, which selects an area of about 17600 nm^2 (equivalent to a diameter of 150 nm). This procedure minimizes beam damage of the transformation-sensitive alumina.[23] To verify that the coating structure was in fact not altered by the electron bombardment, we also conducted EELS measurements at 80 kV for selected samples, which revealed the same ELNES features.

The edges of interest for the EELS/ELNES studies are the Al-L$_{2,3}$-edge (edge onset around 75 eV) and the O-K edge (edge onset around 530 eV).[17,24] The spectra were recorded with dispersions of 0.1 eV/channel and 0.3 eV/channel. The energy resolution as measured by the full-width-at-half-maximum of the zero-loss peak was ranging between 0.8 and 1.2 eV, depending on the chosen dispersion. The convergence and collection semi-angles during analysis were ~0 mrad (parallel illumination) and < 8 mrad, respectively. To obtain a high signal-to-noise ratio, typical acquisition times of 10 to 100 s were used. All spectra were corrected for dark current and channel-to-channel gain variation. The pre-edge background was extrapolated using a power law function and subtracted from the original data.[17]

III. Results and discussion

In this work, two different Al$_2$O$_3$ films are investigated, which will be referred to as sample A and B in the following. They were deposited under identical conditions, but sample B was subjected to enhanced ion bombardment due to the applied -40 V bias voltage in comparison to sample A, which was grown at floating potential. According to XRD, the structure of the coatings was predominantly amorphous for sample A and γ–Al$_2$O$_3$ structured for sample B prior to annealing. The coating thickness, as determined by fracture cross-sections, was 3 and 4 µm for sample A and B, respectively.[11] After annealing, the XRD measurements had indicated the formation of γ–Al$_2$O$_3$ for sample A and α–Al$_2$O$_3$ for sample B.

A. As-deposited samples

All deposited coatings are well adherent to the silicon substrates. Fig. 1 shows TEM cross-section overviews of the low-energy ion bombardment sample A (Fig. 1(a)) and sample B (Fig. 1(b)), which was grown under enhanced ion bombardment conditions. In both cases, the film can be divided into areas differing in structure and

morphology. The area close to the substrate will be referred to in the following as near-interface-layer and the upper section of the coating as top-layer. While sample A exhibits an about 1890 nm thick near-interface-layer, the thickness of this layer in sample B is ~430 nm.
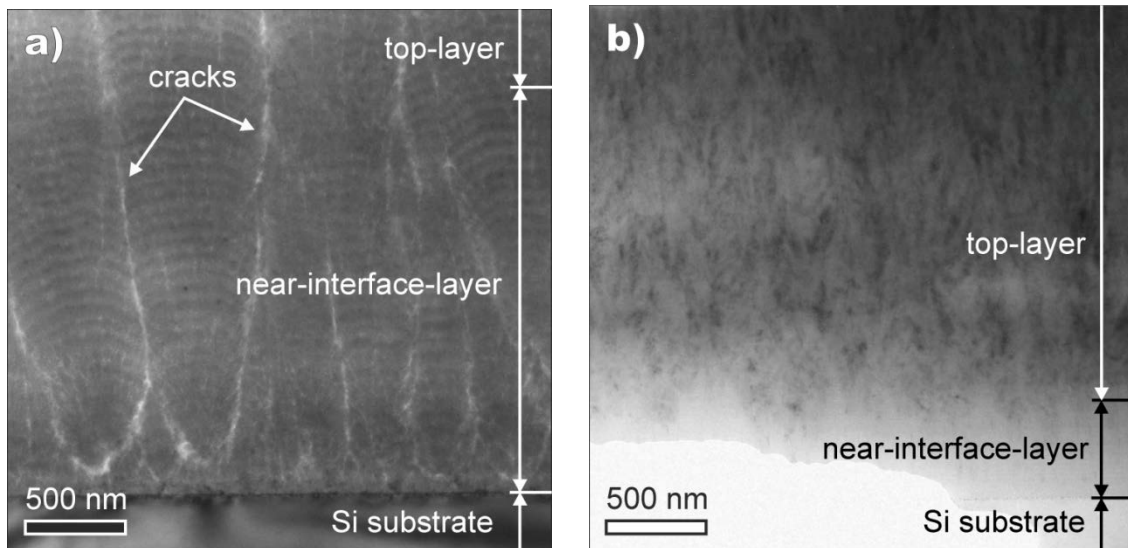

Figure 1.   TEM cross-section overview image of (a) sample A and (b) sample B in the as-deposited state.

Sample A in as-deposited state shows a layered structure (Fig. 1(a)), which is a result of the substrate rotation during deposition. There, depending on the position of the sample with respect to the magnetrons, the plasma conditions as well as the flux of sputtered Al atoms vary, which can lead to a modulation of composition and structure.[25,26] This layering seems to be promoted by the weak ion bombardment conditions used for sample A as it is not observed in sample B (see Fig. 1(b)). Furthermore, a crack network, preferably at column boundaries, can be seen for the low ion bombardment sample, which is assumed to be caused by cooling down after deposition. This network is a result of tensile stress formation due to the higher thermal expansion coefficient of alumina (7 to $8.3 \cdot 10^{-6}$ /K) compared to the silicon substrate ($3.55 \cdot 10^{-6}$ /K).[27,28] The originating tensile stress exceeds the strength of the weak interfaces formed without sufficient ion irradiation.[29] In contrast, sample B shows a dense structure with no visible cracks, i.e. the enhanced ion bombardment

seems to improve the strength of the interfaces. This interpretation is corroborated by the measured biaxial coating stress, with tensile stresses of 180 MPa for sample A and 520 MPa for sample B. The observed difference is related to partial stress relaxation within sample A due to tensile crack formation. This finding is in good agreement with results published in Refs.[30,31]

In order to obtain qualitative and quantitative insight into the crystallographic structure, SAD and HRTEM imaging were performed (Fig. 2). In the near-interface- and the top-layer of sample A, $\gamma-Al_2O_3$ crystallites were found which are most likely embedded in an amorphous phase; the presence of $\delta-Al_2O_3$ cannot be excluded since some of the characteristic reflections overlap with those of $\gamma-Al_2O_3$. The average crystallite sizes for the near-interface-layer and the top-layer of sample A have been determined to 22 ± 8nm and 6 ± 2 nm, respectively. In between, a 360 nm thick intermediate layer with a crystal size of 8 ± 3 nm was found. The near-interface-layer (Fig. 2(a)) shows more crystals and less amorphous areas than the top-layer (Fig 2(b)). In addition, areas with less thickness contrast are seen in the top-layer labeled as "holes", which might origin from phase-transformation or loss of $\gamma-Al_2O_3$ grains during ion-milling.
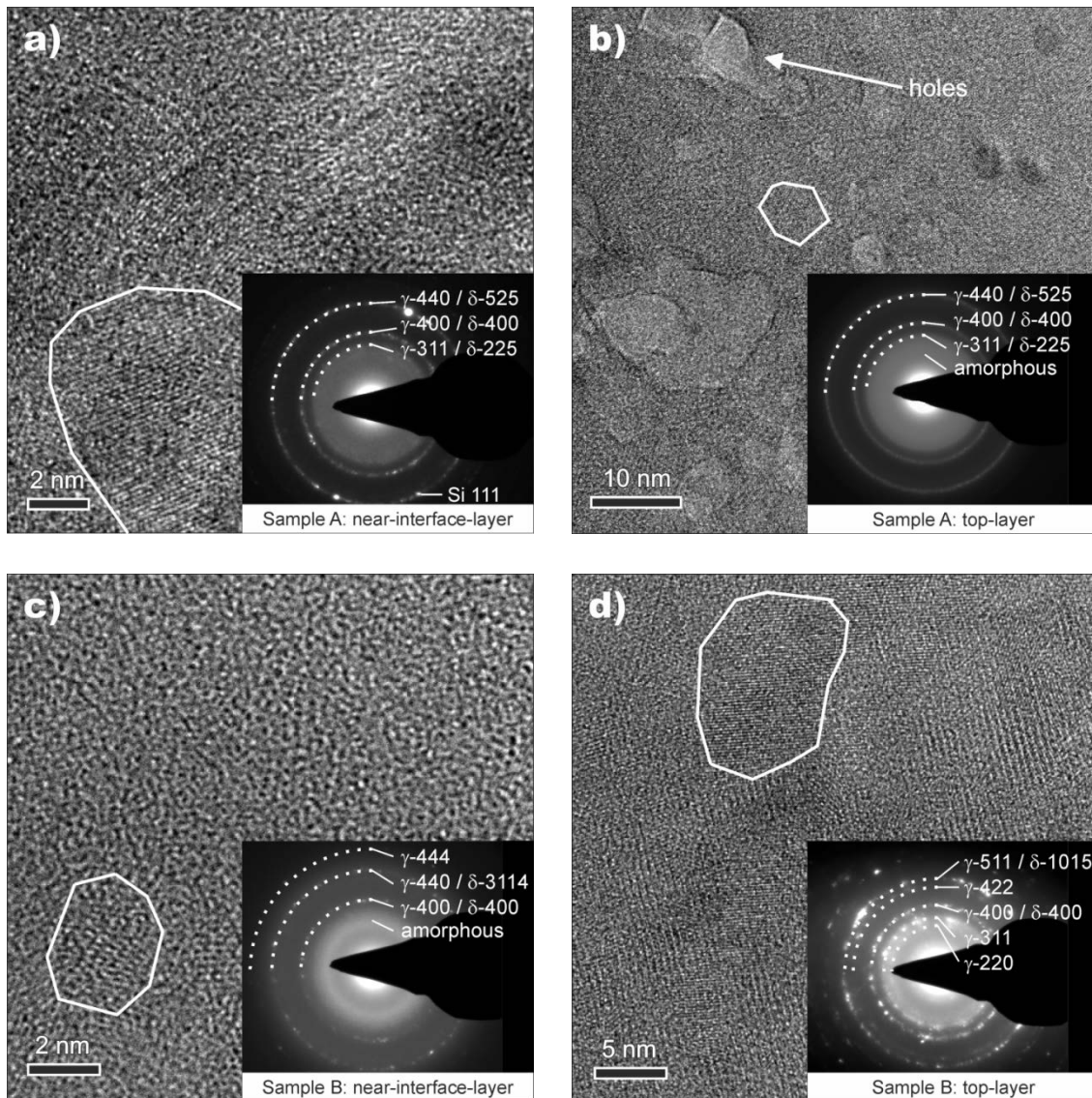
Figure 2.   HRTEM images with SAD pattern in the as-deposited state of (a) near-interface-layer of sample A, (b) top-layer of sample A, (c) near-interface-layer of sample B, and (d) top-layer of sample B.

The near-interface-layer of sample B consists of an amorphous matrix and a few very small $\gamma-Al_2O_3$ crystallites (Fig. 2(c)). In contrast to sample A, the crystallinity of the $\gamma-Al_2O_3$ phase is as a result of the intense ion bombardment more pronounced in the top-layer (see Fig. 2(d)). An average crystal size of 4 ± 2 nm for the near-interface-layer has been determined. The top-layer shows crystallites with bimodal size distribution; i.e. smaller ones with a grain size of 14 ± 4 nm as well as larger ones with

102±23 nm. For sample B no intermediate layer was found. These results are in agreement with an earlier XRD study, where sample A was reported to be predominantly amorphous and sample B γ–Al_2O_3 structured. It can be considered that the fine grained γ–Al_2O_3 crystallites in sample A embedded in an amorphous phase appear amorphous since they lead to extremely broad peaks on a diffuse background.[11]

The Al-$L_{2,3}$ and O-K ELNES spectra measured at 300 keV at the respective two layers of the as-deposited sample are given in Fig. 3. The near-interface-layer displays mainly the characteristic ELNES features of γ–Al_2O_3. Since δ–Al_2O_3 is viewed as a superstructure of γ–Al_2O_3, contributions of δ–Al_2O_3 can again not be fully excluded.[9] For the top-layer, the measured Al-$L_{2,3}$ ELNES can be treated as a superposition of γ–Al_2O_3 and amorphous Al_2O_3. The most important difference between these layers is that the shoulder at the low-energy side of the main peak of the near-interface-layer in the Al-$L_{2,3}$ ELNES at ~79 eV is less pronounced in the near-interface-layer than in the top-layer (see arrow in Fig. 3(a)). This energy-loss region is related to the number of Al atoms occupying tetrahedral sites of the O sub-lattice.[9,32,33,34] In γ–Al_2O_3, only a part of the Al atoms is located at these tetrahedral sites while most Al atoms occupy octahedral sites. In contrast, in amorphous Al_2O_3 the Al has mainly a tetrahedral coordination.[23] The higher intensity in this region for the top-layer thus indicates a higher amount of tetrahedrally coordinated Al atoms which might stem from a higher fraction of amorphous matrix.
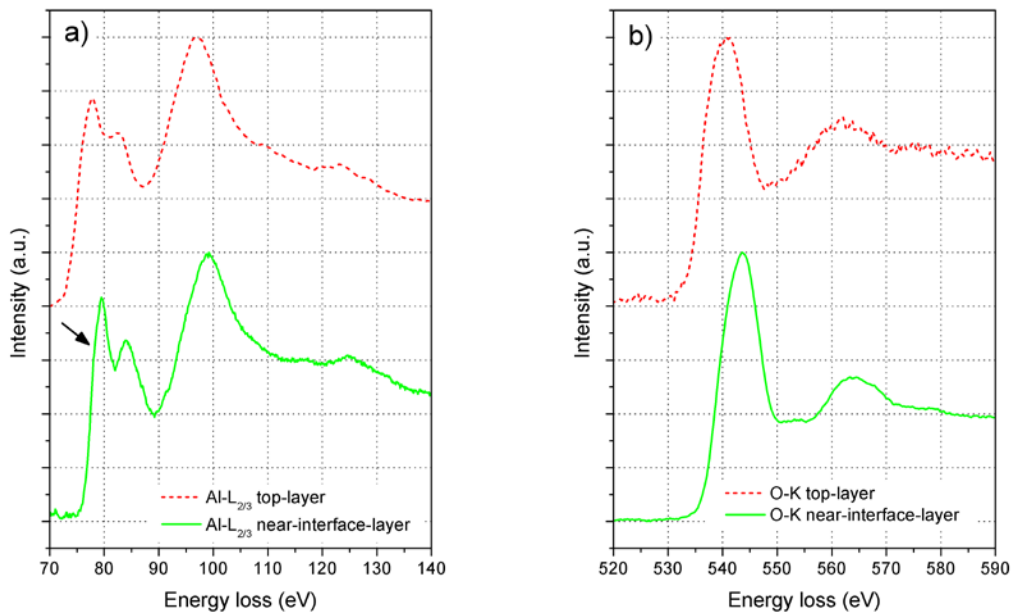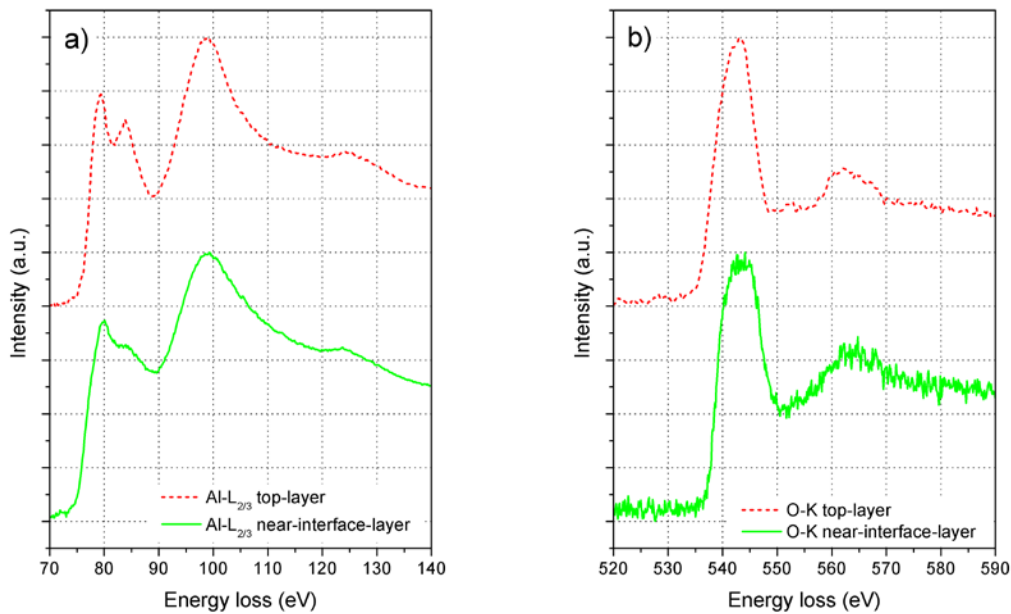
Figure 3.   EELS spectra of sample A in as-deposited state taken at the near-interface and top-layer. (a) Al-$L_{2,3}$ edge and (b) O-K edge. The arrow in the Al-$L_{2,3}$ spectrum marks the shoulder originating from tetrahedrally coordinated Al ions.

Fig. 4 shows the Al-$L_{2,3}$ and O-K ELNES spectra measured for sample B in the as-deposited state in the near-interface- and the top-layer taken under the same conditions as used for Fig. 3. The ELNES features of Al-$L_{2,3}$ and O-K of the top-layer reveal shapes characteristic for γ–Al_2O_3.[9,34] However, contributions of δ–Al_2O_3 can again not be fully excluded. In contrast to the top-layer, the ELNES of the Al-$L_{2,3}$ and O-K edge of the near-interface-layer show contributions of mainly amorphous Al_2O_3.[23,33] This can be clearly seen in the different shape of the Al-$L_{2,3}$ ELNES which is in agreement with published data on amorphous Al_2O_3.[23]

Figure 4. EELS spectra of sample B in as-deposited state taken at the near-interface and top-layer. (a) Al-L$_{2,3}$ edge and (b) O-K edge.

B. Annealed samples

To address the structural changes upon thermal exposure, both samples were also investigated after vacuum annealing at 1000 °C for 12 h. The obtained TEM images for sample A are presented in Figs. 5(a)-(d). Again, the compositional modulation due to substrate rotation can be clearly seen in the overview in Fig. 5(a). In Fig. 5(b), a detail of the near-interface-layer in higher magnification, showing the tensile crack network existing already in the as-deposited state, seen as vertical cracks (compare Fig. 1(a)), is given. In addition, horizontal cracks have emerged, which could be related to the annealing process, i.e. to changes in crystallinity and volume changes due to phase transformation. Both, the HRTEM images presented in Fig. 5(c) for the near-interface-layer and in Fig. 5(d) for the top-layer indicate a crystalline structure, only the grain size differs. The SAD pattern confirms these grains to be γ–Al$_2$O$_3$, but again δ–Al$_2$O$_3$ cannot be excluded. In case of the 1940 nm thick near-interface-layer, the

90

average grain size increases significantly from 22±8nm measured in the as-deposited state to 65±19 nm after annealing, indicating coarsening of γ–Al_2O_3 grains. Within the upper fraction of the near-interface-layer with a thickness of 690 nm, grain coarsening is less pronounced and the grain size reaches a value of 20±9 nm. For the top-layer with its higher content of amorphous phase in the as-deposited state, a slight decrease of the average grain size from 6±2 nm to 5±2 nm could be observed, whereas in the lower part of the top-layer an essentially unaffected grain size with 6±1 nm was found. These observed small grain sizes after annealing could be explained by a high nucleation rate and subsequent highly competitive growth of grains within the amorphous phase.[35] The 360 nm thick intermediate layer with a grain size of 8±3 nm in the as-deposited state could not be detected anymore after annealing.
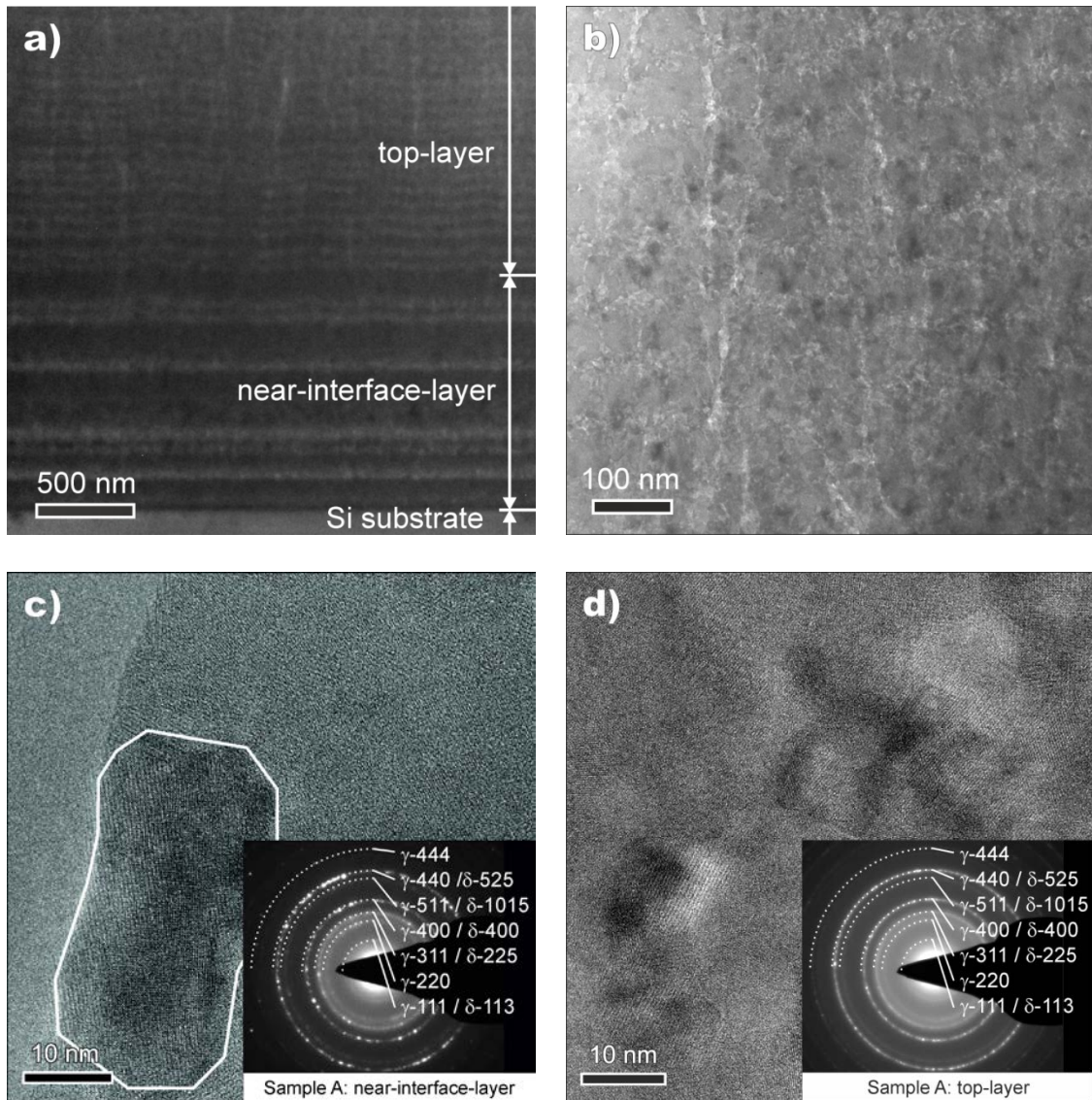
Figure 5.   Micrographs of sample A after vacuum annealing at 1000 °C for 12 h. (a) TEM cross-section overview image, (b) TEM detail of top-layer showing the formed crack network, (c) HRTEM image with SAD pattern of the near-interface-layer and (d) HRTEM image with SAD pattern of the top-layer.

The TEM results obtained for sample B after annealing are presented in Figs. 6(a)-(c). The near-interface-layer exhibits a fully crystalline structure with $\gamma-Al_2O_3$ grains (Fig. 6(b)). This is a marked change compared to the nearly fully amorphous state for the as-deposited film, where only a few $\gamma-Al_2O_3$ grains had been present. The

average size of these grains is 5±2 nm, remaining at a size similar to the initial state (4±2 nm). For sample B, the top-layer also shows a dramatic structural change upon annealing (Fig. 6(c)). According to SAD examination, the top-layer has transformed into the thermodynamically stable $\alpha-Al_2O_3$ phase. For example, Fig. 6(c) shows the SAD pattern of a single crystalline $\alpha-Al_2O_3$ grain. Starting from $\gamma-Al_2O_3$ crystals with an average grain size of 102±23 nm and 14±4 nm in the as-deposited state, the grain size has raised up to 288±89 nm and 130±30 nm for $\alpha-Al_2O_3$. After an annealing time of 12 hours, a layer of about 2 µm thickness from the coating surface has already transformed to $\alpha-Al_2O_3$, whereas an untransformed near-interface-layer with a thickness of about 1 µm is still visible in Fig. 6(a). It should be noted that the latter layer now includes the near-interface-layer denoted for the as-deposited sample (see Fig. 1(b)) and that fraction of the top-layer which has not yet been transformed to $\alpha-Al_2O_3$. This is corroborated by the above mentioned slight decrease in size of the remaining $\gamma-Al_2O_3$ grains. Although growth of $\gamma-Al_2O_3$ grains on the expense of the amorphous phase will occur in the not yet transformed top-layer, the average grain size is lower compared to values obtain for the virgin state, because the expected high nucleation rate in the nearly fully amorphous near-interface-layer hinders grain growth.[35]
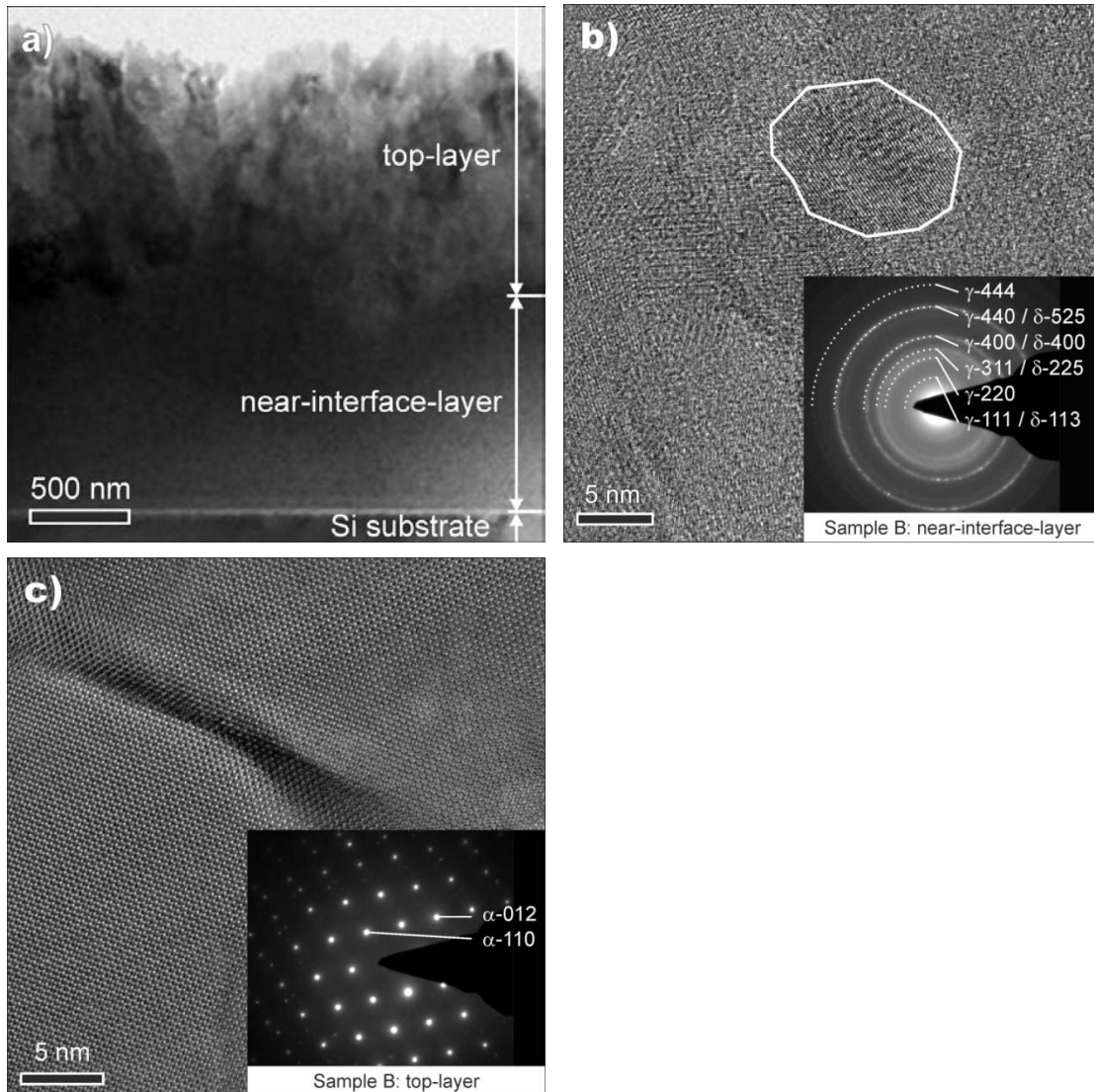
Figure 6. Micrographs of sample B after vacuum annealing at 1000 °C for 12 h.(a) TEM cross-section overview image, (b) HRTEM image with SAD pattern of the near-interface-layer, and (c) HRTEM image with SAD pattern of the top-layer.

The results of the EELS measurements of near-interface-layer and top-layer of sample A, again taken at 300 keV, after the annealing treatment are summarized in Fig. 7. The ELNES observed for both layers corresponds well to the reports for bulk $\gamma-Al_2O_3$.[9] For the annealed sample B, a similar shape of the spectra has been observed for the near-interface-layer, as shown in Fig. 8, which clearly changed compared to the

as-deposited state, again confirming crystallization of the amorphous areas and formation of γ–Al_2O_3. In contrast, the spectra obtained for the top-layer are significantly different from those taken for the near-interface-layer. There, the Al-$L_{2,3}$ and O-K ELNES show all features characteristic for α–Al_2O_3. The Al-$L_{2,3}$ ELNES reveals an additional peak emerging at ~86 eV and a strong asymmetry of the peak at ~100 eV, compared to the symmetric one characteristic for γ–Al_2O_3.[9] Changes in the O-K ELNES also occur, in particular instead of the one peak at higher energy loss (~565 eV), two peaks occur for α–Al_2O_3.
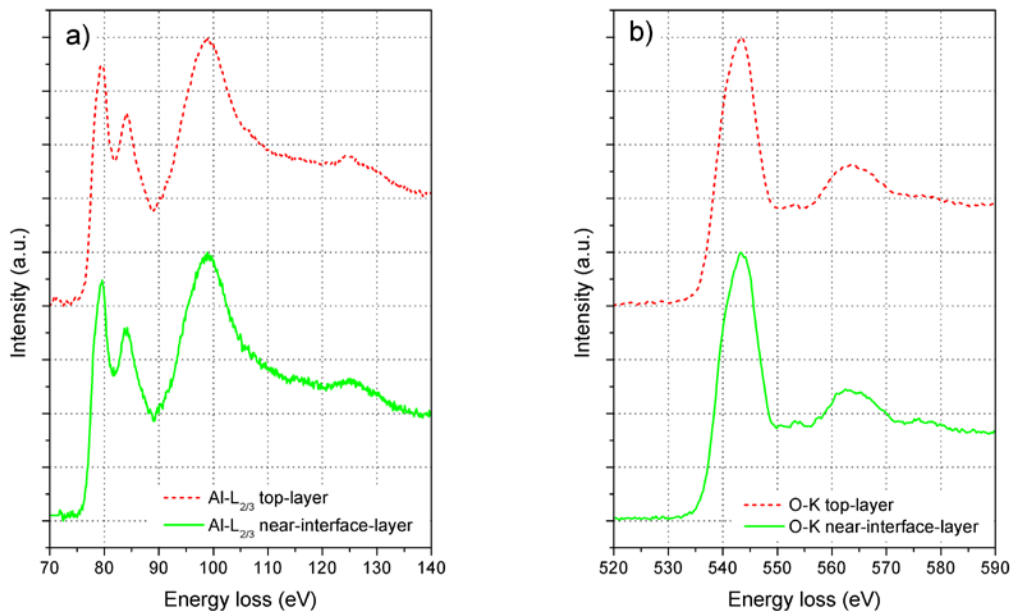
Figure 7.   EELS spectra of sample A after vacuum annealing at 1000 °C for 12 h taken at the near-interface-layer and top-layer. (a) Al-$L_{2,3}$ edge and (b) O-K edge.

95
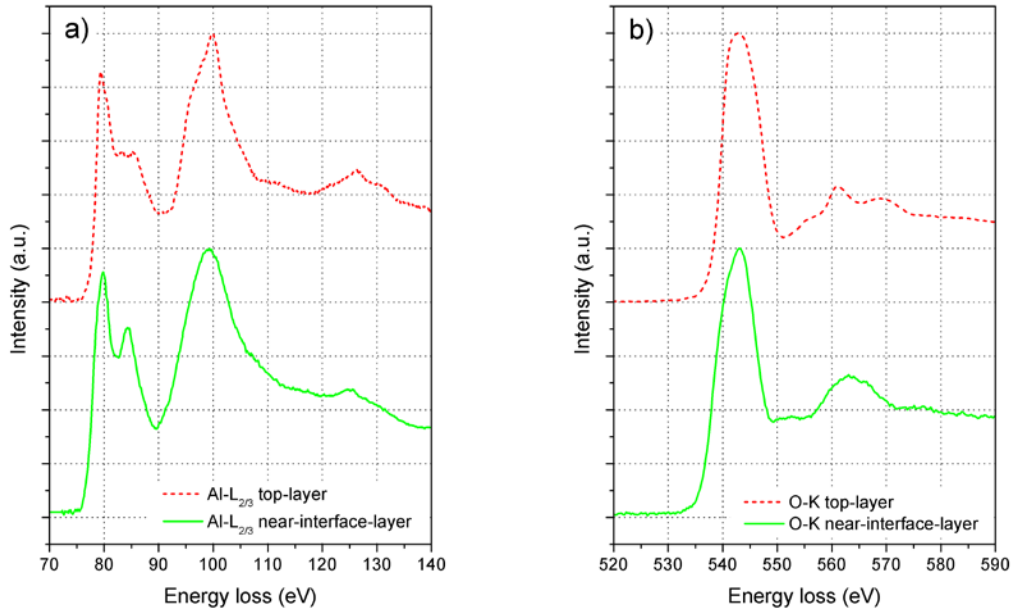
Figure 8.   EELS spectra of sample B after vacuum annealing at 1000 °C for 12 h taken at the near-interface-layer and top-layer. (a) Al-L$_{2,3}$ edge and (b) O-K edge.

C. Microstructural evolution

To summarize and visualize the changes observed, a schematic of the microstructural evolution during annealing is shown in Fig. 9. Sample A and B grown at low and intense ion bombardment conditions, respectively, are distinguished by different thicknesses of the near-interface- and top-layers. In both cases, the near-interface-layer consists of $\gamma-Al_2O_3$ crystallites embedded in an amorphous matrix; however, the intense and high-energy ion bombardment conditions used for sample B result in the formation of a significantly thinner near-interface-layer with a higher fraction of amorphous matrix compared to the low-energy ion bombardment sample (compare Figs. 9(a) and (c)). On the other hand, after formation of this near-interface-layer the high-energy ion bombardment seems to trigger growth of $\gamma-Al_2O_3$ crystallites in the top-layer, while for sample A grown at floating bias the fraction of $\gamma-Al_2O_3$

96

crystallites decreases for the top-layer. Taking into account that the thermal stability of the metastable phases formed is high, it may be assumed that structure formation is governed mainly by the ion bombardment conditions rather than the slightly higher substrate temperature observed for sample B (see section II.A). Thus, it might be assumed that the with increasing coating thickness decreasing size of $\gamma-Al_2O_3$ crystallites of sample A is an effect of the vanishing electrical conductivity of the growing alumina layer with increasing deposition time. This effect is only valid for sample A deposited at floating potential while charging effects do not affect growth of the alumina layer on sample B using pulsed bias. The growth mode observed for sample B may be compared to that of cubic boron nitride thin films, where also crystal nucleation and growth is triggered by high-energy ion bombardment after formation of an essentially amorphous interfacial layer.[36]

$\gamma-Al_2O_3$ crystallites nucleate and/or grow during vacuum annealing at 1000 °C for 12 hours at the expense of the amorphous matrix in both the near-interface- and the top-layer of the low-energy ion bombardment sample. Also, grain growth is observed in the layer close to the substrate interface of the sample synthesized using high-energy ion bombardment conditions. For sample A, growth occurs most pronounced close to the substrate interface, while in the top-layer a high nucleation rate prevents coarsening of the crystallites. Both near-interface-layer and top-layer can still be distinguished for sample A after annealing (compare Figs. 9(a) and (b)). In contrast, the major fraction of the top-layer in sample B has transformed to $\alpha-Al_2O_3$. Skogsmo *et al.* have reported that the transformation into $\alpha-Al_2O_3$ starts at free surfaces, provided by the coating surface and cracks.[37] Due to the volume decrease for the transformation from $\gamma-Al_2O_3$ to $\alpha-Al_2O_3$, a continuous transformation starting from these free surfaces and proceeding towards the coating/substrate interface is fostered.[38] Consequently, the interface seen in Fig. 9(d) is now formed between the already transformed $\alpha-Al_2O_3$ and the still existing $\gamma-Al_2O_3$ crystallites close to the substrate. Annealing time and temperature determine the remaining thickness of the untransformed layer.
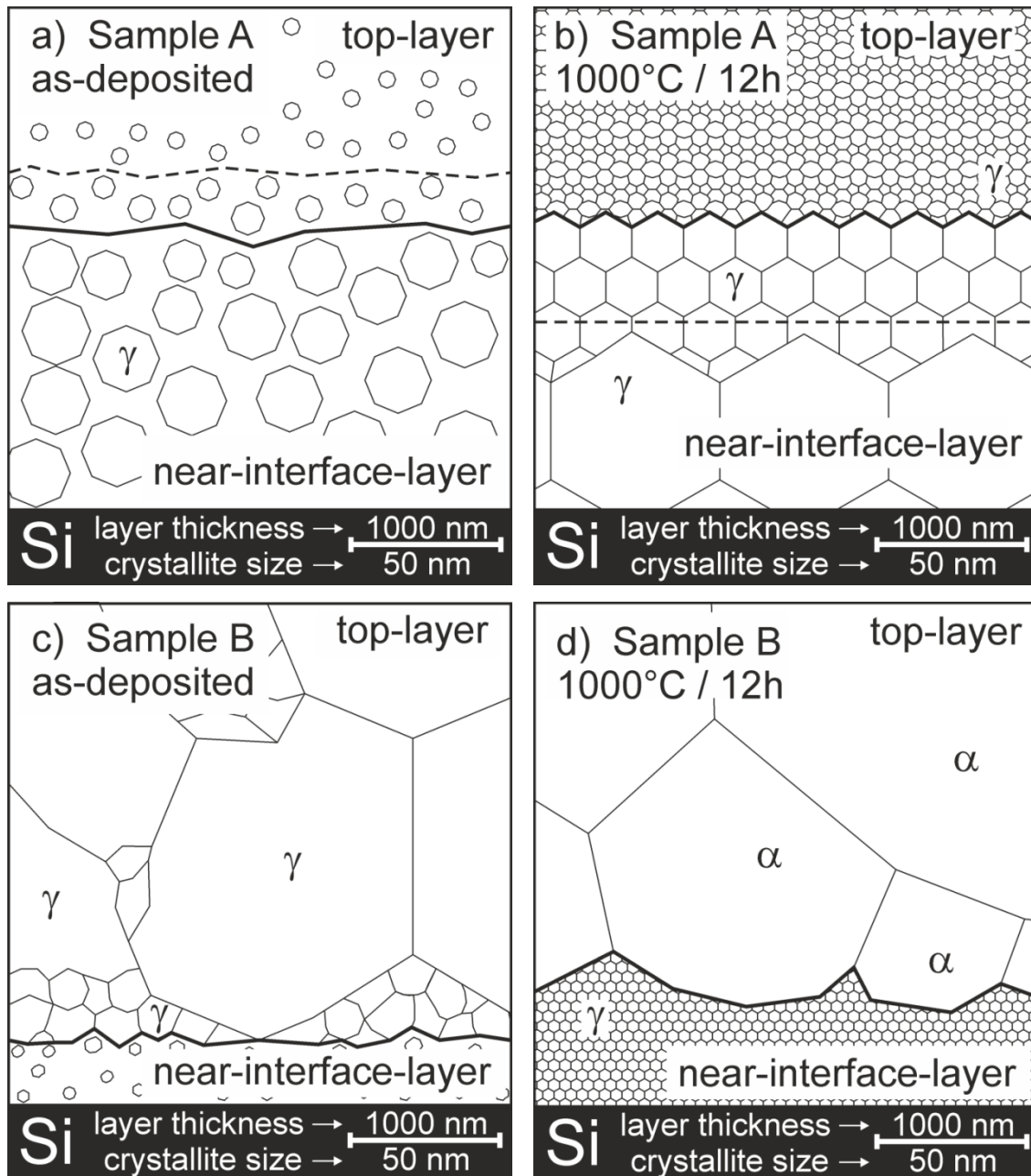
Figure 9. Schematic summarizing the cross-sectional microstructure of sputtered alumina coatings grown under low-energy ion bombardment (sample A) and under intense ion bombardment (sample B) in the as-deposited (a, c) and annealed (b, d) condition.

IV. Conclusions

The microstructure evolution during thermal exposure of two types of metastable alumina coatings synthesized by pulsed direct current magnetron sputtering has been investigated by transmission electron microscopy techniques. Both coatings can be divided in a near-interface and top-layer region, which differ strongly in structure. In the as-deposited state, the sample deposited at low ion bombardment consists of small $\gamma-Al_2O_3$ grains embedded in an amorphous phase, with a higher $\gamma-Al_2O_3$ phase content close to the Si substrate. During vacuum annealing at 1000 °C for 12 h, the coating becomes fully crystalline consisting of rather small $\gamma-Al_2O_3$ grains. In contrast, the as-deposited coating grown under intense ion bombardment conditions is characterized by an increased content of $\gamma-Al_2O_3$ grains in the top-layer and an amorphous matrix in the near-interface-layer, where only a few $\gamma-Al_2O_3$ grains are embedded. During annealing, nucleation of $\alpha-Al_2O_3$ starts at the coating surface, proceeding towards the interface with an area of not yet transformed $\gamma-Al_2O_3$ grains close to the substrate.

V. Acknowledgement

References

[1]   M. Kathrein, W. Schintlmeister, W. Wallgram, and U. Schleinkofer, Surf. Coat. Technol. **163** , 181 (2003).

[2]   J. Kopac , M. Sokovic, and S. Dolinsek, J. Mater. Process Technol. **118**, 377 (2001).

[3]   M.J. Buerger, *Phase Transformations in Solids* (John Wiley & Sons, New York 1951), pp. 202.

[4]   H.P. Rooksby, X-Ray *Identification and Crystal Structures of Clay*, (Mineralogical Society, London, England, 1951), pp. 264.

[5]   H.P. Rooksby and C.J.M. Rooymans, *The Formation and Structure of Delta Alumina*, Philips Research Laboratories, Eindhoven, Netherlands, 235 (1961).

[6]   W.E. Lee and K.P.D. Lagerlof, J. Electron Micr. Tech. **2**, 247 (1985).

[7]   B.C. Lippens and J.H. De Boer, Acta Crastallogr. **17**, 1312 (1964).

[8]   R.-S. Zhou and R.L. Snyder, Acta Crystallogr., Structural Science **B47**, 617 (1991).

[9]   I. Levin, A. Berner, C. Scheu, H. Müllejans, and D.G. Brandon, Mikrochim. Acta **15**, 93 (1998).

[10]   K.J.D. MacKenzie, J. Temuujin, M.E. Smith, P. Angerer, and Y. Kameshima, Thermochim. Acta **359**, 87 (2000).

[11]   V. Edlmayr, M. Moser, C. Walter, and C. Mitterer, Surf. Coat. Technol. **204**, 1576 (2010).

[12]   P. Eklund, M. Sridharan, G. Singh, and J. Bottiger, Plasma Process Polym. **6**, 907 (2009).

[13] J. Musil, J.Blazek, P. Zeman, S. Proksová, M. Sasek, and R. Cerstvý, Appl. Surf. Sci. **257**, 1058 (2010).

[14] K. Bobzin, N. Bagcivan, A. Reinholdt, and M. Ewering, Surf. Coat. Technol. **205**, 1444 (2010).

[15] P. Rez, *Transmission Electron Energy-Loss Spectrometry in Materials Science*, eds. M.M. Disko, C.C. Ahn, and B. Fultz, (The Minerals, Metals & Materials Society, Warrendale, Pennsylvania , 1992), pp. 107.

[16] R. Brydson, H. Sauer, and W. Engel, *Transmission Electron Energy-Loss Spectrometry in Materials Science*, eds. M.M. Disko, C. C. Ahn, and B. Fultz, (The Minerals, Metals & Materials Society, Warrendale, Pennsylvania 1992), pp.131.

[17] R.F. Egerton, Electron Energy-Loss Spectroscopy in the Electron Microscope, (Plenum Press, New York, 1996).

[18] K.-D. Bouzakis, G. Skordaris, N. Michailidis, I. Mirisidis, G. Erkens, and R. Cremer, Surf. Coat. Technol. **202**, 826 (2007).

[19] G.G. Stoney, Proc. R. Soc. Lond. A**82**, 172 (1909).

[20] W.D. Nix, Metall. Trans. **20A**, 1989 (1989).

[21] A. Strecker, U. Salzberger, and J. Mayer, Prakt. Metallogr.**30**, 482 (1993).

[22] C. Scheu, M. Gao, K. van Benthem, S. Tsukimoto, S. Schmidt, W. Sigle, G. Richter, and J. Thomas, J. Microscopy **210**, 16 (2003).

[23] J. Bruley, Microsc. Microanal. Microstruct. **4**, 23 (1993).

[24] C.C. Ahn and O.L. Krivanek, *EELS Atlas*, ASU HREM, Center for Solid State Science, Arizona State University, Tempe, Arizona and Gatan, Gatan, Warrendale, PA.

[25] J. Neidhardt, H. Högberg, and L. Hultman, Thin Solid Films **478**, 34 (2005).

[26] J. Neidhardt, S. Mráz, J.M. Schneider, E. Strub, W. Bohne, B. Liedke, W. Möller, and C. Mitterer, J. Appl. Phys. **104**,063304 (2008).

[27] H.O. Pierson, *Handbook of Chemical Vapor Deposition (CVD)*, 2nd ed. (Noyes Publications / William Andrew Publishing, LLC, New York, USA, 1999), pp. 297.

[28] P. Becker, K. Dorenwendt, G. Ebeling, R. Lauer, W. Lucas, R. Probst, H.J. Rademacher, G. Reim, P. Seyfried, and H. Siegert, Phys. Rev. Lett. **46**, C6-128 (1981).

[29] I. Petrov, P.B. Barna, L. Hultman, and J.E. Greene, J. Vac. Sci, Technol. **A21**, 117 (2003).

[30] J. Ramm, M. Ante, T. Bachmann, B. Widrig, H. Brändle, M. Döbeli, Surf. Coat. Technol. **202**, 876 (2007).

[31] D. Hochauer, C. Mitterer, M. Penoy, C. Michotte, H.P. Martinz, M. Kathrein, Surf. Coat. Technol. **203**, 350 (2008).

[32] J. Bruley, M.-W. Tseng, and D.B. Williams, Microsc. Microanal. Microstruct. **6**, 1 (1995).

[33] R. Brydson, J. Phys. D: Appl. Phys. **29**, 1699 (1996).

[34] D. Bouchet, C. Colliex, Ultramicroscopy **96**, 139 (2003).

[35] K. Lu, Mat. Sci. Engin. Reports **16**, 161 (1996).

[36] S. Reinke, R. Freudenstein, W. Kulisch, Surf. Coat. Technol. **97**, 263 (1997).

[37] J. Skogsmo, M. Halvarsson, and S. Vuorinnen, Surf. Coat. Technol. **54**, 186 (1992).

[38] S. Vuorinen and L. Karlsson, Thin Solid Films **214**, 132 (1992).

11. Publication III

Publication III

Microstructure and thermal stability of corundum-type $(Al_{0.5}Cr_{0.5})_2O_3$ solid solution coatings grown by cathodic arc evaporation

V. Edlmayr[a], M. Pohler[a], I. Letofsky-Papst[b], C. Mitterer[a]

[a]Department of Physical Metallurgy and Materials Testing, Montanuniversität Leoben, 8700 Leoben, Austria

[b]Institute for Electron Microscopy, University of Technology Graz, Steyrergasse 17, 8010 Graz, Austria

Microstructure and thermal stability of corundum-type $(Al_{0.5}Cr_{0.5})_2O_3$ solid solution coatings grown by cathodic arc evaporation

V. Edlmayr[a], M. Pohler[a], I. Letofsky-Papst[b], C. Mitterer[a]

[a] Department of Physical Metallurgy and Materials Testing, Montanuniversität Leoben, 8700 Leoben, Austria

[b] Institute for Electron Microscopy, University of Technology Graz, Steyrergasse 17, 8010 Graz, Austria

Abstract

Corundum-type $(Al_xCr_{1-x})_2O_3$ coatings were grown by reactive cathodic arc evaporation in an oxygen atmosphere using AlCr targets with an Al/Cr atomic ratio of 1. Since the $(Al_xCr_{1-x})_2O_3$ solid solution shows a miscibility gap below 1300 °C, where spinodal decomposition is predicted, the microstructural changes upon annealing were investigated by a combination of transmission electron microscopy, X-ray diffraction, Raman spectroscopy, and differential scanning calorimetry. The as-deposited coating consists primarily of the corundum-type $(Al_xCr_{1-x})_2O_3$ solid solution, with smaller fractions of cubic $(Al_xCr_{1-x})_2O_3$. An additional Al-rich amorphous phase and a Cr-rich crystalline phase stem from the droplets incorporated. The corundum-type $(Al_xCr_{1-x})_2O_3$ solid solution is still present after vacuum annealing at 1050 °C for 2 hours, whereas the cubic $(Al_xCr_{1-x})_2O_3$ phase has transformed to corundum-type $(Al_xCr_{1-x})_2O_3$. Cr and Cr_2O_3 have been detected in the annealed coating, the latter most probably originating from the partial oxidation of Cr-rich droplets. Upon crystallization of the amorphous phase fractions present, $\gamma-Al_2O_3$ is formed, which then transforms

into α–Al_2O_3. No evidence for decomposition of the corundum-type $(Al_xCr_{1-x})_2O_3$ solid solution could be found within the temperature range up to 1400 °C.

Keywords: *(Al,Cr)$_2$O$_3$; Al-Cr-O, Arc evaporation; Coatings; Annealing; Thermal stability.*

1. Introduction

Recently, wear-resistant coatings grown by cathodic arc evaporation for cutting applications within the Al_2O_3–Cr_2O_3 system have been introduced [1, 2]. The performance of coatings for cutting tools is determined by a combination of properties like hardness, wear and thermal fatigue resistance and resistance against oxidation. Therefore, α–Al_2O_3, which is the thermodynamically stable Al_2O_3 phase with corundum-type crystal structure, is highly attractive. Its essential drawback is the high deposition temperature necessary to synthesize coatings with the desired α–Al_2O_3 structure. Depending on the deposition technique, temperatures starting from 700 °C for sputtering up to 1000 °C for chemical vapor deposition (CVD) are required [3-5]. To lower the deposition temperature to ~600 °C and thus to enable coating of thermally sensitive tool steels, the α–Al_2O_3 phase may be stabilized by Cr_2O_3 (eskolaite), forming a corundum-based $(Al_xCr_{1-x})_2O_3$ solid solution. α–Al_2O_3 and Cr_2O_3 are isostructural, the space group being $R\bar{3}c$ [6]. In this crystal structure, the metal cations occupy two-thirds of the octahedral interstitial sites. The ionic radii of Al and Cr are nearly similar (0.057 nm for Al^{3+} and 0.064 nm for Cr^{3+}), which favors the formation of a solid solution between these oxides [7]. The $(Al_xCr_{1-x})_2O_3$ solid solution is formed over the whole composition range for temperatures above 1200 °C under thermodynamic equilibrium conditions [8]. The lattice parameter of such an $(Al_xCr_{1-x})_2O_3$ solid solution changes nearly linearly with composition according to Vegard´s behavior and is discussed in Refs. [9-11]. In contrast, for lower temperatures phase separation of this solid solution to α–Al_2O_3 and Cr_2O_3 by spinodal decomposition occurs [8]. However, this miscibility gap was not observed for coatings grown by physical vapor deposition

techniques so far [12]. This background motivates the present work, where we investigated microstructural changes of $(Al_xCr_{1-x})_2O_3$ solid solution coatings grown by cathodic arc evaporation with temperature by differential scanning calorimetry, X-ray and electron diffraction analyses, Raman spectroscopy and a combination of various transmission electron microscopy techniques. The aim was to contribute to the understanding of the thermal stability of the $(Al_xCr_{1-x})_2O_3$ solid solution formed by plasma-assisted vapor deposition.

2. Experimental details

Coatings were grown on single crystalline silicon (100) and iron foil substrates by cathodic arc evaporation in an Oerlikon Balzers INNOVA system with a base pressure $< 10^{-3}$ Pa. Prior to deposition, all substrates were ultrasonically pre-cleaned in alcohol and etched at ~550 °C in pure Ar plasma with ions extracted from an additional arc discharge. During deposition, an oxygen atmosphere was established by applying a gas flow of 400 sccm. A symmetrical bipolar pulsed bias with an amplitude of 40 V and a pulse frequency of 40 kHz and a negative-to-positive-pulse-time ratio of 19 was applied. The substrate temperature was kept constant at 550 °C. The two arc sources used were equipped with powder metallurgically produced targets having an Al/Cr atomic ratio of 1 (PLANSEE Composite Materials). An arc current of 180 A was used. The used deposition time of 80 min yielded a 3 µm thick coating on all substrates mounted on a two-fold rotating carousel.

After deposition, the coatings grown on silicon were annealed in an HTM Reetz vacuum furnace (base pressure $< 5 \times 10^{-4}$ Pa), applying a heating and cooling rate of 20 K/min. Annealing temperatures of 700, 900, 950, 1000 and 1050 °C were held constant for 2 h. During the heating ramp, an isothermal 30 min step at 250 °C was introduced to remove volatile contaminations.

The chemical composition of the coating was determined by an energy-dispersive X–ray spectroscopy system (EDX, Oxford Instruments INCA) attached to a scanning electron microscope (Zeiss EVO 50). Results have been cross-checked by elastic recoil detection analysis (ERDA) using a 35 MeV Cl^{7+} ion beam with an analyzed area of 1.5×1.5 mm^2 and a depth of information of about ~600 nm.

Coated silicon samples in the as-deposited and the annealed state were prepared for transmission electron microscopy (TEM) investigation using an FEI Nova 200 DB FIB/SEM (focused ion beam/scanning electron microscopy) instrument with an OMNIPROBE in-situ lift-out technique by standard FIB preparation technique [13]. The main part of the TEM studies was conducted in a Philips CM 20 scanning TEM operated at 200 kV (LaB$_6$ cathode), equipped with a Gatan imaging filter (GIF) and a Noran EDX system with an HPGe-detector. This system was applied for bright-field (BF) imaging and for the investigation of the chemical composition. Three different methods were used: (*i*) EDX analysis, (*ii*) electron energy-loss spectroscopy (EELS) using the GIF in spectrum mode, and (*iii*) energy-filtered TEM (EFTEM) using the GIF in imaging mode. The elemental maps were obtained by recording an image at the energy of an element-specific ionization edge. For two-dimensional elemental distribution maps, "jump ratio" images were calculated. This yielded one energy-filtered background image in front of the edge (pre-edge image) and one image at the ionization edge of the element of interest (post-edge image). To get the jump ratio image, the post-edge image was divided by the pre-edge image. In addition, selected area electron diffraction (SAED) investigations were carried out using a Tecnai T12 TEM working at 120 kV (LaB$_6$ cathode).

For investigation of microstructural changes during thermal exposure, differential scanning calorimetry (DSC) measurements were done using a Setaram LabsysEvo. This device was calibrated with the melting points of pure elements (Zn, Al, Au, and Pd). The crucibles for the samples were made of α–Al$_2$O$_3$ and an empty crucible was utilized as reference. In order to avoid substrate interference during the DSC measurement, a powder specimen was used. Coatings were chemically removed

from the iron foil substrate by dissolving it in 25 % nitric acid at 75 °C for approximately 20 min. The remaining film material was rinsed with acetone and ethanol, and manually ground to powder. The powder specimen was heated up to 1400 °C with a constant heating rate of 20 K/min. The sample environment was a dynamic argon atmosphere with flow rate of 20 ml/min. In order to remove volatile contaminations, an isothermal 30 min step at a temperature of 150 °C was applied.

All other analyses were done on coatings grown on silicon substrate. Structural analysis of the as-deposited and annealed coatings was conducted in a Bruker-AXS D8 Advance diffractometer at 2θ angles from 20 to 70° and an angle of incidence of 2° of the primary beam (CuKα radiation). Raman spectra were obtained by means of a Dilor LABRAM confocal Raman spectrometer operated at a laser wavelength of 633 nm. The laser power of the He–Ne laser was 100 mW and the spot size was 5 μm. The spectra were taken between 160 and 1600 cm^{-1} with a resolution of 2 cm^{-1}.

3. Results

The coating reveals with ~22 at.-% Al, ~20 at.-% Cr and ~58 at.-% O a chemical composition close to stoichiometry of $(Al_xCr_{1-x})_2O_3$. Fig. 1(a) shows a BF TEM cross-section overview image of the as-deposited coating on silicon substrate. A dense 3 μm thick coating with columnar grain structure was observed. The column width is in the range of 50 to 100 nm, as measured at higher magnification images, and increasing with film thickness. Diffraction indices of SAED pattern, in order to obtain more information about the microstructure, are given in Fig. 1(b). Diffraction points arranged on diffuse rings were observed. This is in agreement with the columnar grain structure and indicates a nanocrystalline microstructure with a slightly preferred orientation. These rings can be assigned to the rhombohedral ($R\bar{3}c$) lattice (i.e. corundum-based) of the $(Al_xCr_{1-x})_2O_3$ solid solution [14]; the diffuse region in the center of the SAED pattern may be interpreted by the existence of a minor amount of an amorphous phase. It should be noted here that the intense pattern of the corundum-type $(Al_xCr_{1-x})_2O_3$ solid solution might overlap other phases like the face-

centered cubic $(Al_xCr_{1-x})_2O_3$ phase reported by Kathibi *et al.* [15]. An EDX linescan over the whole film thickness yielded a slightly lower Al/Cr atomic ratio compared to the target composition.
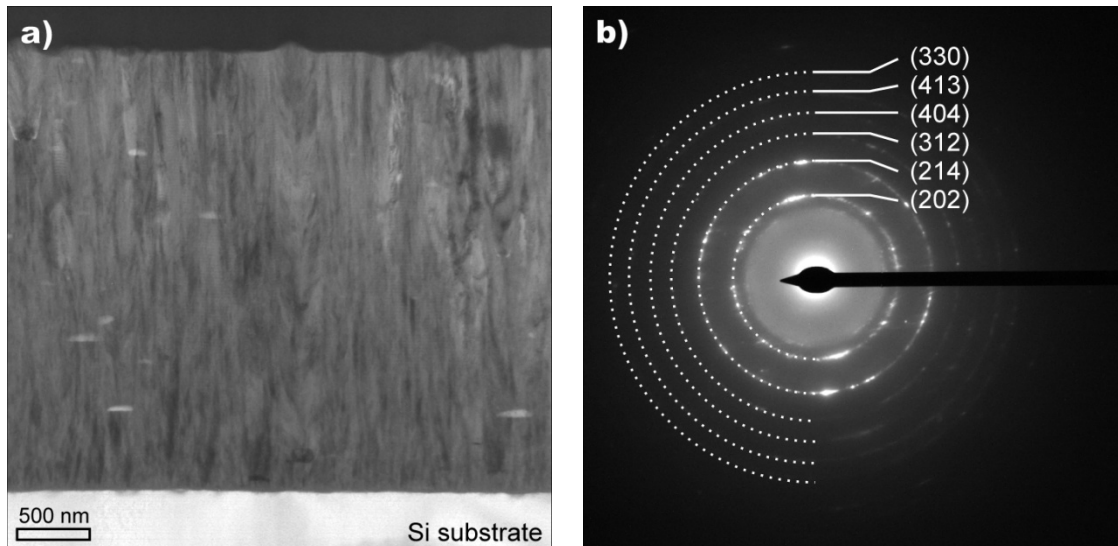

Figure 1. $(Al_xCr_{1-x})_2O_3$ coating deposited on silicon substrate in the as-deposited state, (a) bright-field TEM cross-section overview image and (b) SAED pattern.

The generation of macroparticles, so-called droplets, is a well-known drawback of coatings grown by non-filtered cathodic arc evaporation [16]. These droplets are emitted from the cathode and are mainly composed of the target constitutive metals as well as compounds formed in the reactive deposition atmosphere. According to an earlier study by Pohler *et al.* [17], two types of droplets were observed. Fig. 2(a) shows a sphere-shaped droplet which is characterized by a metallic core consisting of intermetallic Al-Cr phases. The diameter of these metallic droplets is in the range of 300 to 500 nm. A hemispherical-shaped droplet with a representative diameter and height of ~600 and ~200 nm, respectively, is shown in Fig. 2(b). In contrast to the ball-shaped droplets, it can be assumed that the droplet is still in the molten state when it arrives at the film surface, resulting in the flattened shape. According to EDX analyses, the hemispherical droplets consist of aluminum and oxygen, but no chromium could be detected.
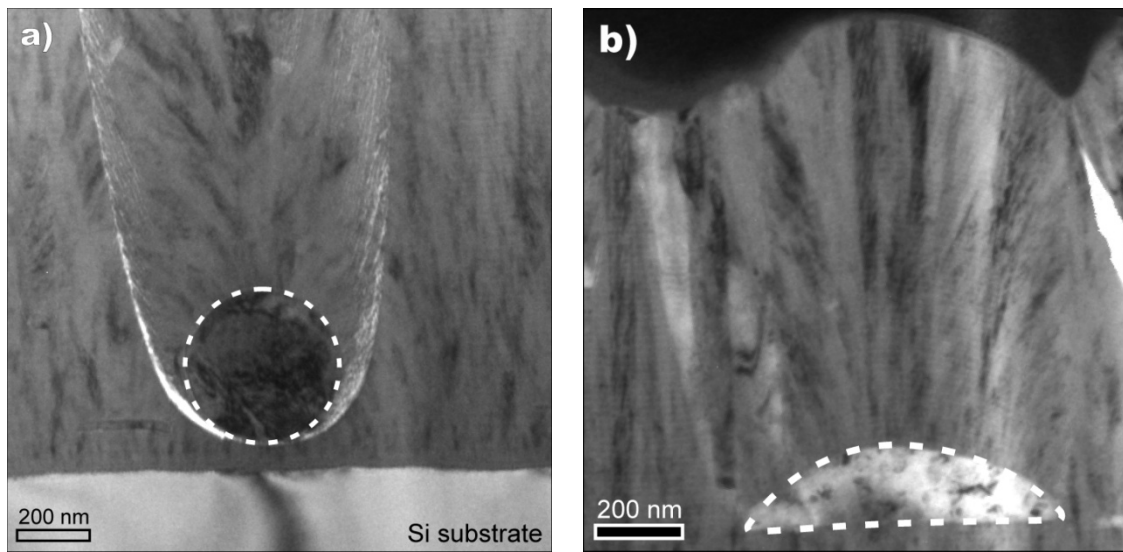
Figure 2. Bright-field TEM images of (a) ball-shaped droplet and (b) hemispherical-shaped droplet in an $(Al_xCr_{1-x})_2O_3$ coating deposited on Si substrate in the as-deposited state.

Fig. 3 shows the DSC signal, i.e. the heat flow, obtained during thermal ramping from room temperature up to 1400 °C. A slightly elevated level of the exothermic heat flow was observed between 650 and 900 °C, which may cover several smaller peaks, e.g. originating from recovery of defects and probably also nucleation and growth of Cr_2O_3 [18] and/or intermediate phases like $\gamma-Al_2O_3$. In particular, the peak with maximum at 848 °C could then be attributed to the crystallization of the metastable $\gamma-Al_2O_3$ [19]. The main exothermal peak appearing at ~1036 °C is indicative for the transformation from $\gamma-Al_2O_3$ into $\alpha-Al_2O_3$. Despite the different deposition techniques and coating composition, this interpretation agrees well to earlier investigations on sputtered Al_2O_3 coatings [20, 21].
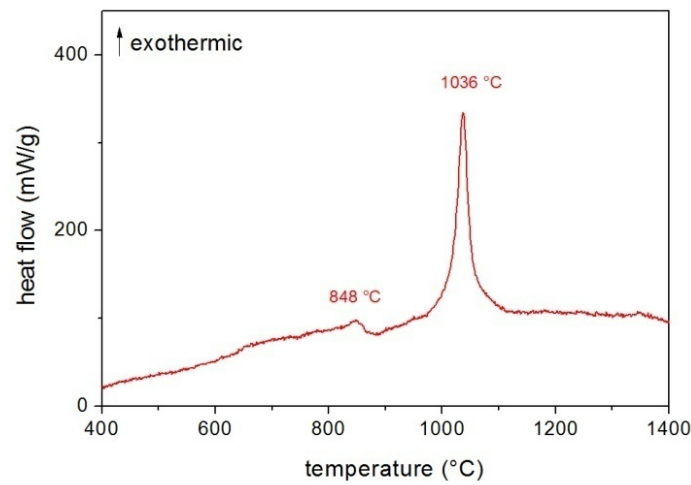
Figure 3. DSC signal (heat flow) of an $(Al_xCr_{1-x})_2O_3$ powder specimen, dissolved from the Fe foil substrate.

Coatings deposited on silicon substrates and coating powder specimens have been characterized by XRD prior to and after annealing at different temperatures. The patterns for the coatings on silicon are presented in Fig. 4. For a better legibility, only peak positions of $\alpha-Al_2O_3$, eskolaite Cr_2O_3, the corundum-based $(Al_xCr_{1-x})_2O_3$ solid solution and metallic chromium are plotted. The peak positions of the solid solution were calculated from the isostructural $\alpha-Al_2O_3$ and eskolaite Cr_2O_3 standard for a replacement of 50% Cr^{3+} by Al^{3+} cations [14]. According to Vegard´s behavior, the replacement of Cr^{3+} with Al^{3+} results in a gradual shift of the diffraction peaks towards higher angles. This means that with increasing Al content the lattice parameters shrink linearly due to the smaller ionic radius of Al compared to Cr [2, 7, 22, 23]. Due to the atomic fraction of Al:Cr ~ 1:1, the peak position corresponding to the $(Al_xCr_{1-x})_2O_3$ solid solution is located in the center between the positions of Cr_2O_3 and $\alpha-Al_2O_3$. This is in good agreement with literature [24, 25]. The as-deposited coating exhibits clear indications for the crystalline $(Al_xCr_{1-x})_2O_3$ solid solution, where the enhanced background indicates an additional amorphous phase, which is also confirmed by SAED (see Fig. 1b). Besides the corundum-based $(Al_xCr_{1-x})_2O_3$ solid solution, an additional fraction of face-centered cubic $(Al_xCr_{1-x})_2O_3$ solid solution, which has been suggested by

Khatibi *et al.* [15] and Najafi *et al.* [26], might contribute to the broad peaks at $2\theta \approx 44.8°$ and 65.8°. With increasing annealing temperature, the contribution of these cubic peaks vanishes and the one of the corundum-based $(Al_xCr_{1-x})_2O_3$ solid solution becomes more pronounced. With increasing temperature, the latter are first shifted towards lower 2θ angles and then shifted back to the original peak position (see the peak at 2θ = 36.8° in Fig. 4). Starting at annealing temperatures of 950 °C, evidence of $\alpha-Al_2O_3$ is visible, which is most pronounced for the (104) peak at 2θ = 35.2°. The strongest orientation of a Cr_2O_3 powder sample is also (104) [14], but there is no unambiguous evidence by XRD for Cr_2O_3 formation in the coating. At temperatures higher than 900 °C, diffusion of Si takes place and the small peaks at $2\theta \approx 27°$ and in the range of 47 to 49° can be attributed to $CrSi_2$. The peaks at $2\theta \approx 32°$, between 41 and 43°, and between 54 and 55° stem from SiO_2 formation. This is corroborated by measurements performed on the powder specimen, where these peaks are absent. Two peaks at $2\theta \approx 44.3°$ and 64.6°, emerging after annealing above 700 °C in both coating and powder specimen, can be attributed to metallic Cr and have also been observed by Ramm *et al.* [2]. Since the peak intensity of the Cr phase is increasing with annealing temperature and the position is within the range of both broad peaks of the cubic $(Al_xCr_{1-x})_2O_3$ phase, its existence in the as-deposited state can not be excluded.
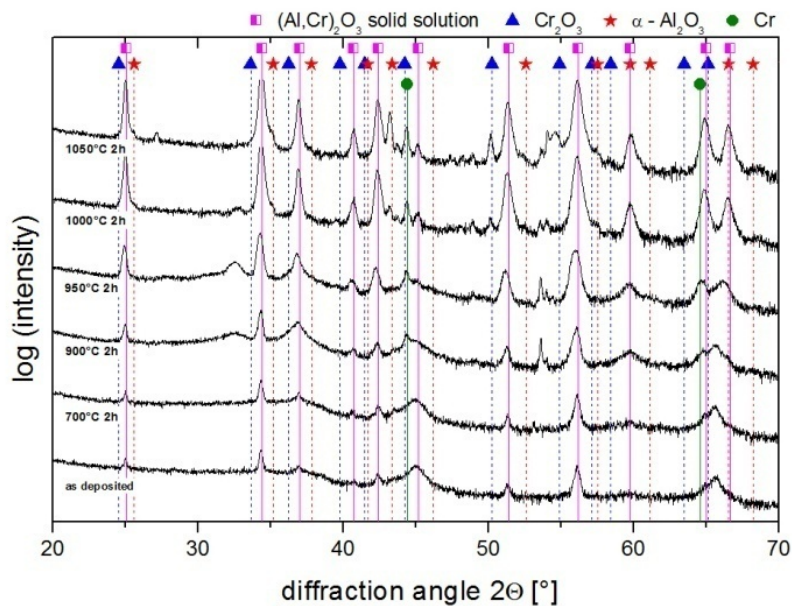
Figure 4.   XRD patterns of an $(Al_xCr_{1-x})_2O_3$ coating deposited on silicon substrate in the as-deposited state and after different annealing treatments.

Fig. 5 shows the Raman spectra of the coating deposited on silicon prior to and after annealing at 1050 °C for 2 h. Reference data for the silicon substrate material and $\alpha-Al_2O_3$ and Cr_2O_3 are added [27]. Since among these oxide phases only $\alpha-Al_2O_3$ is Raman active, the as-deposited coating exhibits only the dominant silicon substrate peak with slight indications of the eskolaite Cr_2O_3 phase. After annealing, the peak at 300 cm^{-1} can be clearly attributed to Cr_2O_3. An additional huge peak with maximum at 593 cm^{-1} is located between the positions of $\alpha-Al_2O_3$ and Cr_2O_3. In the region from 350 to 450 cm^{-1}, where many $\alpha-Al_2O_3$ peaks are located, small peaks can be detected. Also the broad peak between 700 and 800 cm^{-1} confirms the existence of $\alpha-Al_2O_3$ in the annealed coating.

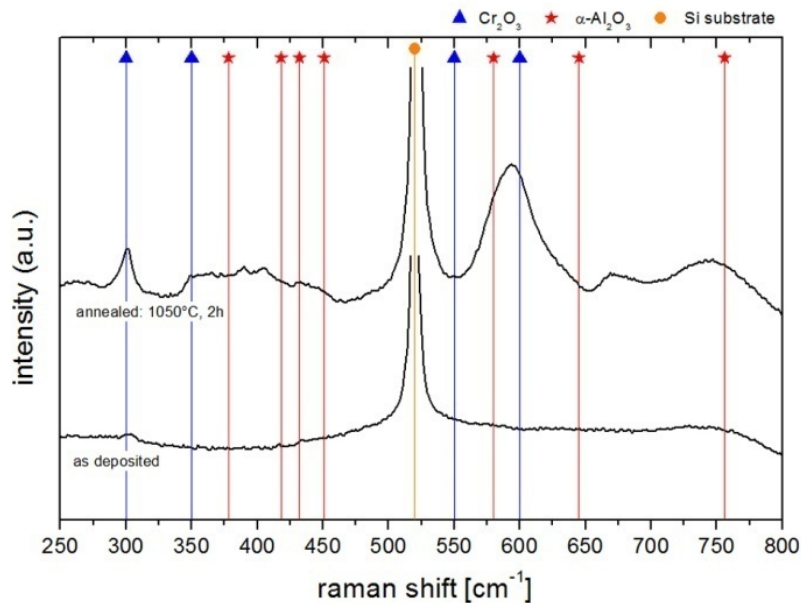Figure 5.   Raman spectra of the $(Al_xCr_{1-x})_2O_3$ coating prior to and after annealing. Also shown are the standard values for the substrate material silicon, $\alpha-Al_2O_3$ and Cr_2O_3.

To address the structural changes upon thermal exposure, the coating deposited on silicon was investigated after annealing at 1050 °C for 2 h by TEM (see Figs. 6-8). In comparison to the sample in the as-deposited state (see Fig. 1(a)), many spherically shaped grains with a diameter between 100 and 300 nm and a few cracks are observed in the BF TEM cross-section of the annealed coating (see Fig. 6(a)). A TEM image with higher magnification illustrates the presence of holes of different shape and size (Fig. 6(b)). Some of those holes seem to be localized on former grain boundaries. The SAED pattern of the grains (Fig. 6(c)) indicates a rhombohedral ($R\bar{3}c$) lattice in the $[1\bar{1}0]$ zone axis, according to the coating in as-deposited state.
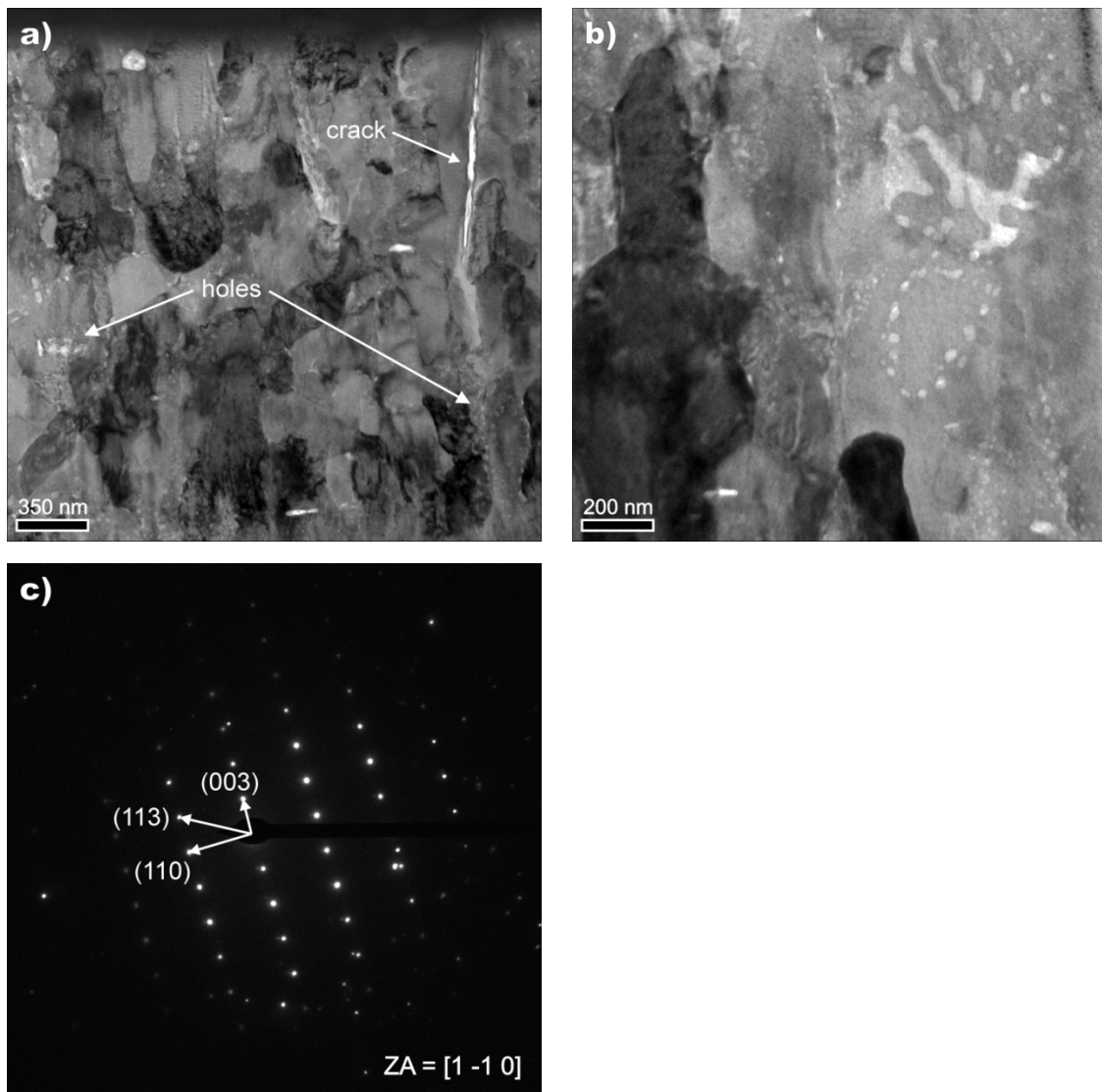
Figure 6. Sample deposited on silicon substrate after annealing, (a) BF TEM cross-section overview image, (b) BF TEM detail of hole formation and (c) SAED pattern. The zone axis is $[1\bar{1}0]$.

In Figs. 7 and 8, two EFTEM-series acquired at different magnifications are shown, representing the elemental distribution of Al, Cr and O. The four micrographs show the same viewing area of the annealed sample grown on silicon. Fig. 7(a) presents a BF cross-section image of the coating, where besides the interface to the substrate the above mentioned grains and the holes could be seen. Fig. 7(b) shows the

aluminum distribution map, indicating – with the exception of the holes – a homogeneous distribution. In the chromium map (Fig. 7(c)), a depletion of chromium on grain boundaries is clearly visible. Additionally, at the interface to the silicon substrate an ~80 nm thick layer poor in chromium was found, which is followed by a region of small chromium-rich grains. No serious variation of the aluminum content was found in this area (see Fig. 7(b)). This is in contrast to the oxygen content (Fig. 7(d)), which shows low oxygen concentrations at those areas where the above mentioned Cr-rich grains are localized. It should be noted that at those areas where holes are found, oxygen seems to be dominant due to lower sample thickness.
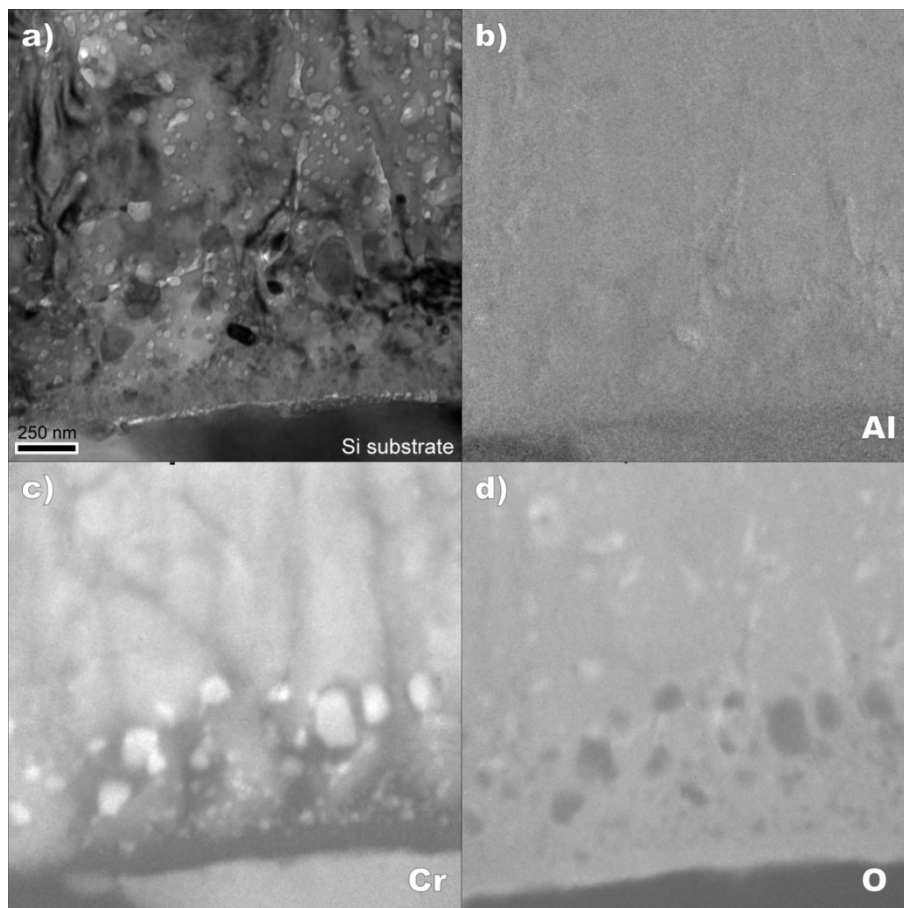

Figure 7.   Energy-filtered TEM analysis of the coating after annealing, (a) bright field image, (b) aluminum, (c) chromium and (d) oxygen jump ratio image.

A BF cross-section TEM image of a sphere-shaped droplet is illustrated in Fig. 8(a). The metallic core of such a droplet in the as-deposited state shown in Fig. 2(a) stays essentially unmodified after annealing at 1050 °C for 2 h. The outer rim of the droplets is expected to be oxidized during annealing due to its exposure to the oxygen-containing environment of the surrounding underdense area; those areas are still visible as holes after annealing. However, they seem to undergo a major rearrangement due to the growth of the neighboring grains and minimization of the pore surface, resulting in a broader shape, see the bright areas in Fig. 8(a). The aluminum map indicates depletion in the area of the holes and an enrichment in aluminum is visible on grain boundaries and the metallic core of the droplet (see Fig. 8(b)). Less chromium on these grain boundaries and a chromium-depleted grain, most probably originating from a hemispherical-shaped droplet [17], was detected (see Fig. 8(c)). The oxygen distribution map in Fig. 8(d) confirms the oxygen-rich area above the metallic core of the sphere-shaped droplet, where the lower oxygen content of the droplet is also visible.
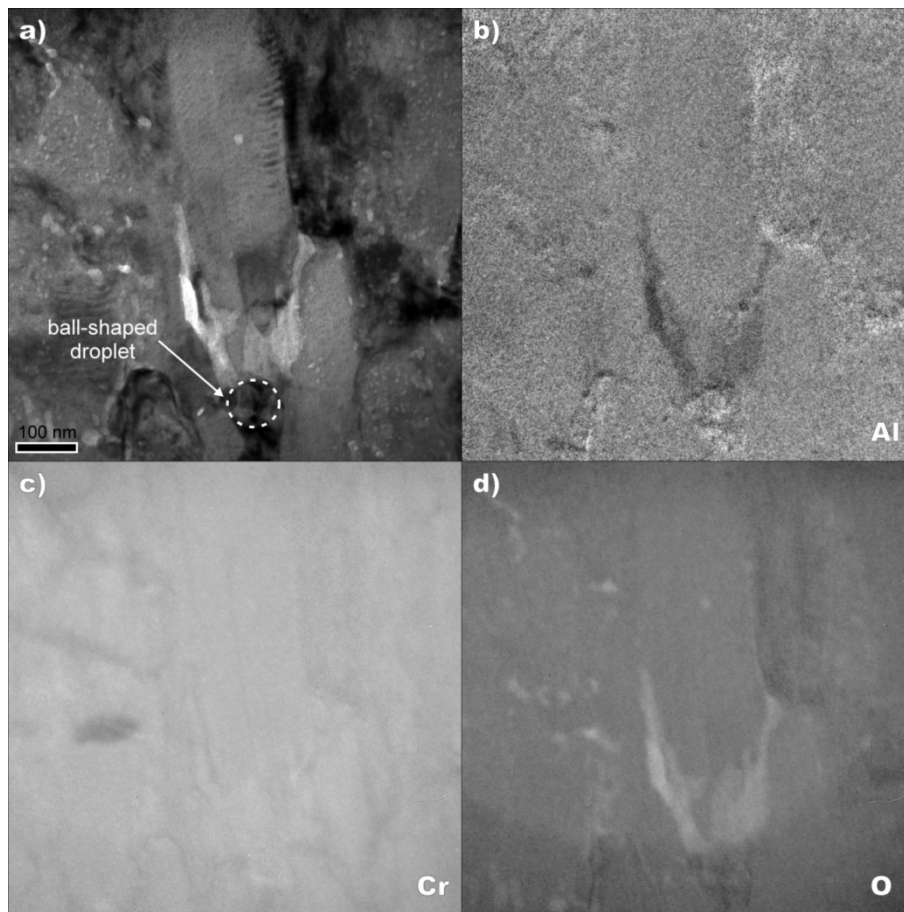
Figure 8.   Energy-filtered TEM analysis of the area surrounding a ball-shaped droplet after annealing, (a) bright field image, (b) aluminum, (c) chromium and (d) oxygen jump ratio image.

4. Discussion

($Al_xCr_{1-x})_2O_3$ coatings with an Al/Cr atomic ratio of ~1 were grown by cathodic arc evaporation with a dense, columnar morphology. In the as-deposited state, the coating microstructure is dominated by the rhombohedral ($Al_xCr_{1-x})_2O_3$ solid solution. Additionally, a smaller fraction of the cubic ($Al_xCr_{1-x})_2O_3$ phase, as inferred by the two broad diffraction peaks located at peak positions of $2\theta \approx 44.8°$ and 65.8°, was found. Also metallic chromium and an aluminum-rich amorphous phase could be detected,

originating from crystalline ball-shaped and amorphous hemispherical-shaped droplets, respectively [17].

No unambiguous evidence for spinodal decomposition of the rhombohedral and the cubic $(Al_xCr_{1-x})_2O_3$ solid solutions was found during vacuum annealing at 1050 °C for 2 h. According to Kathibi *et al.* [28], the cubic $(Al_xCr_{1-x})_2O_3$ phase transforms to the rhombohedral $(Al_xCr_{1-x})_2O_3$ solid solution above 900 °C, which corresponds well to its vanishing XRD peaks (see Fig. 4). The $\alpha-Al_2O_3$ phase observed by XRD stems from crystallization of the formerly amorphous and aluminum-rich hemispherical-shaped droplets. This is corroborated by DSC measurements, indicating the crystallization of the amorphous phase fraction present in the as-deposited state to $\gamma-Al_2O_3$ at 848 °C and at its transformation to the thermodynamically stable $\alpha-Al_2O_3$ at 1036 °C. Also temporary melting of the aluminum-rich droplets during annealing can not be excluded, before they undergo oxidation. Cr_2O_3 could be formed by oxidation of the chromium-rich ball-shaped droplets in their under-dense and thus oxygen-containing environment during annealing. This process could be based on substitutional diffusion fostered by the vacancies existing in the neighborhood of the droplets, where chromium can diffuse into the area of lower density and form Cr_2O_3 by up-taking the oxygen available there [29]. The microstructural changes occurring during annealing result in formation of thermal cracks and holes, which can be attributed to volume changes due to phase transformation and/or temporary melting processes.

5. Conclusions

The effects of thermal annealing on the microstructure of $(Al_xCr_{1-x})_2O_3$ solid solution coatings with an Al/Cr atomic ratio of ~1 deposited by cathodic arc evaporated were investigated. In the as-deposited state, the coating shows a dense columnar structure, consisting mainly of the corundum-type $(Al_xCr_{1-x})_2O_3$ and a minor fraction of a cubic $(Al_xCr_{1-x})_2O_3$ solid solution. Additionally, crystalline chromium and amorphous aluminum-rich phases could be detected, originating from ball- and hemispherical-shaped droplets, respectively. While the cubic $(Al_xCr_{1-x})_2O_3$ phase

transforms to the corundum-type $(Al_xCr_{1-x})_2O_3$ solid solution at elevated temperature, no significant changes of the latter were found after annealing at 1050 °C for 2 h. The observed $\alpha-Al_2O_3$ phase stems from the now crystallized and oxidized, formerly amorphous hemispheric-shaped droplets. Oxidation of Cr−rich ball-shaped droplets, having oxygen stored within the surrounding underdense areas, leads to formation of Cr_2O_3.

Summing up, the temperature driven microstructural changes occurring within arc evaporated $(Al_xCr_{1-x})_2O_3$ coatings have been investigated. The corundum-type $(Al_xCr_{1-x})_2O_3$ solid solution is characterized by a remarkable thermal stability, making these coatings interesting candidates for high-temperature applications.

Acknowledgement

References

[1]   B.K. Tay, Z.W. Zhao, D.H.C. Chua, Mater. Sci. Eng. R. 52 (2006) 1.

[2]   J. Ramm, M. Ante, T. Bachmann, B. Widrig, H. Brändle, M. Döbeli, Surf. Coat. Technol. 202 (2007) 876.

[3]   F. Fietzke, G. Goedicke, W. Hempel, Surf. Coat. Technol. 86 (1996) 657.

[4]   O. Zywitzki, G. Hoetzsch, Surf. Coat. Technol. 94 (1997) 303.

[5]   T. Kohara, H. Tamagaki, Y. Ikari, H. Fujii, Surf. Coat. Technol. 185 (2004) 166.

[6]   R.M. Spriggs, S.I. Bender, J. Am. Ceram. Soc. 45 (1962) 506.

[7]   M. Ristic, S. Popovic, S. Msic, Mater. Lett. 16 (1993) 309.

[8]   W. Sitte, Mater. Sci. Monogr. 28A (1985) 451.

[9]   J. Ramm, M. Ante, H. Brändle, A. Neels, A. Dommann, M. Döbeli, Adv. Eng. Mater. 9 (2007) 604.

[10]   D.M. Roy, R.E. Barks, Nature Phys. Sci. 235 (1972) 118.

[11]   L.R. Rossi, W.G. Lawrence, J. Am. Ceram. Soc. 53 (1970) 604.

[12]   M. Witthaut, R. Cremer, K. Reichert, D. Neuschütz, Microchim. Acta 133 (2000) 191.

[13]   L.A. Gianuzzi, F.A. Stevie, Micron 30 (1999) 197.

[14]   Powder Diffraction File (Card 00-046-1212 for $\alpha-Al_2O_3$, Card 00-038-1479 for Cr_2O_3), International Centre for Diffraction Data, ICDD-JCPDS, 2007.

[15]   A. Khatibi, J. Palisaitis, C. Höglund, A. Eriksson, P.O.A. Persson, J. Jensen, J. Birch, P. Eklund, L. Hultman, Thin Solid Films 519 (2011) 2426.

[16] R.L. Boxman, S. Goldsmith, Surf. Coat. Technol. 52 (1992) 39.

[17] M. Pohler, R. Franz, J. Ramm, P. Polcik, C. Mitterer, Surf. Coat. Technol. 206 (2011) 1454.

[18] X. Pang, K. Gao, F. Luo, H. Yang, L. Oiao, Y. Wang, A.A. Volinsky, Thin Solid Films 516 (2008) 4685.

[19] V. Edlmayr, M. Moser, C. Walter, C. Mitterer, Surf. Coat. Technol. 204 (2010) 1576.

[20] M. Dressler, M. Nofz, F. Malz, J. Pauli, C. Jäger, S. Reinsch, G. Scholz J. Solid State Chem. 180 (2007) 2409.

[21] D.H. Trinh, K. Back, G. Pozina, H. Blomqvist, T. Selinder, M. Collin, I. Reineck, L. Hultman, H. Högberg, Surf. Coat. Technol. 203 (2009) 1682.

[22] N.D. Chatterjee, H. Leistner, I. Terhart, K. Abraham, R. Klaska, Am. Mineral. 67 (1982) 725.

[23] F. Bondioli, A.M. Ferrari, C. Leonelli, T. Manfredini, L. Linati, P. Mustarelli, J. Am. Ceram. Soc. 83 (2000) 2036.

[24] R. Brill, F. Koch, J. Mazurelle, D. Levchuck, M. Balden, Y. Yamada-Takamura, H. Maier, H. Bolt, Surf. Coat. Technol. 174 (2003) 606.

[25] K. Pedersen, J. Boettiger, M. Sridharan, M. Sillassen, P. Eklund, Thin Solid Films 518 (2010) 4294.

[26] H. Najafi, A. Karimi, P. Dessarzin, M. Morstein, Thin Solid Films 520 (2011) 1597.

[27] J.S. Zabinski, N.T. McDevitt, Raman Spectra of Inorganic Compounds Related to Solid State Tribochemical Studies, Final Report WL-TR-96-4034, Materials Directorate Wright Laboratory, Wright-Patterson Airforce Base, Ohio, 1996 (available at http://www.dtic.mil/cgi-bin/GetTRDoc?AD=ADA310647).

[28]   A. Khatibi, J. Lu, J. Jensen, P. Eklund, L. Hultman, Surf. Coat. Technol. 206 (2012) 3216.

[29]   R.H. Doremus, J. Appl. Phys. Rev. B 82 (2010) 174302.